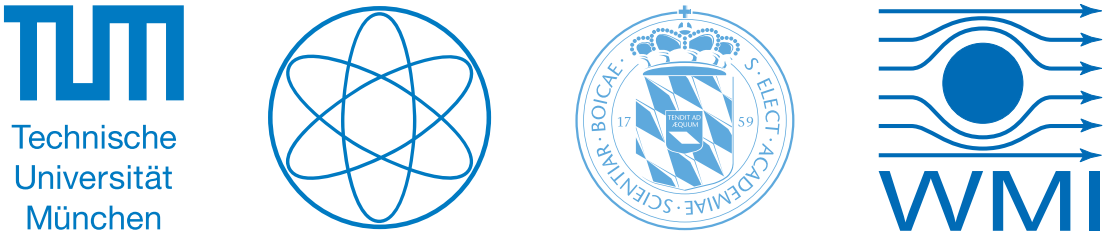

Carrier and Lattice Dynamics in Systems with Charge and Spin Order

Dissertation

Hans-Martin Emil Eiter

August 2014

Advisor: Prof. Dr. Rudolf Gross

Fakultät für Physik
Technische Universität München

TECHNISCHE UNIVERSITÄT MÜNCHEN

Fakultät für Physik
Lehrstuhl E23 für Technische Physik

Walther-Meißner-Institut für Tieftemperaturforschung
der Bayerischen Akademie der Wissenschaften

Carrier and Lattice Dynamics in Systems with Charge and Spin Order

Hans-Martin Emil Eiter

Vollständiger Abdruck der von der Fakultät für Physik der Technischen Universität München zur Erlangung des akademischen Grades eines

Doktors der Naturwissenschaften

genehmigten Dissertation.

Vorsitzender:		Univ.-Prof. Dr. Martin Zacharias
Prüfer der Dissertation	1.	Univ.-Prof. Dr. Rudolf Gross
	2.	Univ.-Prof. Dr. Christian Pfleiderer

Die Dissertation wurde am 07.08.2014 bei der Technischen Universität München eingereicht und durch die Fakultät für Physik am 25.08.2014 angenommen.

Abstract

This thesis discusses the impact of charge and spin ordering on electron and lattice excitations in the rare-earth tritellurides and in MnSi. Using Raman spectroscopy, anisotropies in the electron dynamics are studied as a function of temperature, magnetic field and applied pressure. In the tritellurides band hybridization was identified as an important factor for charge density wave formation. In MnSi phonons and conduction electrons respond to both the helimagnetic phase transition and the fluctuations above.

Kurzzusammenfassung

In dieser Arbeit werden die Auswirkungen von Ladungs- und Spinordnung auf Elektronen- und Gitteranregungen in den Seltenerd-Tritelluriden und in MnSi diskutiert. Mit Raman Spektroskopie wurden Anisotropien in der Elektronendynamik bei tiefen Temperaturen, im Magnetfeld und unter hohem Druck untersucht. In den Tritelluriden trägt die Bandhybridisierung entscheidend zur Entstehung der Ladungsdichtewellen bei. In MnSi reagieren Phononen und Leitungselektronen auf den helimagnetischen Phasenübergang und die Fluktuationen bei höheren Temperaturen.

Contents

Chapter 1

Introduction

A system of atoms, electrons, and spins always tries to find a favourable arrangement that minimizes its free energy in a competition of various interactions such as Coulomb or exchange interaction and entropy. Upon tuning external parameters such as temperature, pressure or magnetic field, the balance shifts, and abrupt changes of structure or dynamics occur upon crossing critical values. A phase transition takes places. The most familiar example are certainly the phase transitions of water from ice to liquid and vapour defining the Celsius temperature scale.

An active field of contemporary research is the investigation of ordered phases in the electronic system such as superconductivity, charge- and spin-density waves, itinerant magnetism or complex spin textures [1–6]. Their intriguing magnetic and electronic properties are not only interesting from an academic point of view, but are used in numerous technological applications such as magnetic data storage. In this thesis, charge and spin order in metallic materials and the related interactions with the crystal lattice are studied.

Charge density waves (CDW) are periodic modulations of the electron density in real space. In low dimensional materials, the transition into the CDW phase can be driven by the electronic system showing a divergent response to an external perturbation. The divergence is related to the topology of the Fermi surface, particularly to the presence of parallel surface sheets that can be mapped onto each other by a single vector in momentum space, referred to as nesting [5]. As a consequence, a finite electron-phonon coupling leads to periodic distortion of the lattice. Quite surprisingly, it has been shown theoretically that, in the quasi one-dimensional case, an unconventional CDW can also be triggered purely by phonons [7], i.e. the lattice. Unconventional, in this context, means that the CDW energy gap is anisotropic due

to anisotropic electron-phonon coupling. Of course, in real materials combinations of electronic instabilities and anisotropic electron-lattice interactions drive the CDW phase transition, and several recent studies raise the question as to whether nesting alone is sufficient to explain the observed CDW ordering vector, particularly in dimensions higher than one [8–12].

Johannes and Mazin [12] argue that only a tiny fraction of the observed charge ordering phase transitions, if any at all, is due to nesting alone, since electronic instabilities are easily destroyed even by small deviations from perfect nesting conditions. Rather, a concerted action of the electronic and ionic subsystem drives the phase transition [12]. Therefore, several mechanisms beyond purely electronic ones are discussed including orthorhombicity, the tendency towards phase separation and nematicity via the Coulomb interaction [10,13–15]. Strongly momentum dependent electron-phonon interaction was identified to play an important role as well as competing instabilities, such as magnetism or superconductivity [2, 11, 12, 16].

Can the conditions for the various types of CDW formation and orientation be accessed experimentally? Already early analyses of the Ginzburg-Landau functional showed that the electron-phonon coupling strength determines the energy of the amplitude fluctuations of the CDW order parameter, where the order parameter can be associated with the CDW condensate density [5]. The amplitude fluctuations can be directly observed in a Raman experiment and are usually referred to as amplitude modes (AM). Then the electron-phonon coupling constant can be derived as soon as the energy of the CDW phonon is known from either theory or other sources [5, 17]. In addition, the excitation gap in the electronic spectrum can be studied by light scattering providing information on the energy gain in the CDW state. In many cases, the transition temperatures were found to be much lower than expected from the energy gaps as a result of fluctuations [18]. Therefore, one may wonder whether the related fluctuations can be observed directly. It will in fact be one of the results to be presented below, that the fluctuations can be observed directly in the Raman experiment if the samples are sufficiently clean [19]. As another side effect of clean samples, the amplitude mode can be scrutinized in the entire CDW phase including a range of approximately one degree below the transition temperature thus substantially augmenting earlier work [20, 21]. In this context, the rare-earth tritellurides turned out to be ideally suited samples and the Raman technique has the capability to provide a host of useful new information on CDW formation.

Similar advantages apply in the case of spin order. Here, the focus is on itinerant magnetism contributing crucially to, e.g., the magnetism in iron, cobalt and nickel. Major achievements in understanding the mechanism were obtained in the 1970s and 1980s in the framework of spin fluctuation theory [22, 23]. In this context, MnSi is one of the most interesting compounds due to its well defined hierarchy of energy scales [24]. The ferromagnetic exchange is the strongest scale and leads to a parallel alignment of the spins. The Dzyaloshinskii-Moriya interaction is weaker than the exchange energy. It is proportional to the cross product of spins and hence favours a perpendicular alignment of neighbouring magnetic moments [25–27]. Finally on the weakest scale, crystal electric field effects pin the spin arrangement in the crystal [28]. The complex interplay of these competing interactions results in a rich phase diagram as a function of temperature, magnetic field [29], doping [30] and pressure [31].

The interest in MnSi revived in recent years, when an unusual non-Fermi liquid (NFL) behaviour was observed in high pressure experiments [32]. The low-temperature resistivity of MnSi switches from the Fermi liquid like T^2 behaviour below a critical pressure p_c to a $T^{3/2}$ temperature dependence above p_c [33]. It was found that the phase transition at p_c is of first order rather than being continuous, and that the NFL behaviour is accompanied by partial magnetic order on short time scales in a small pressure and temperature range [31, 34, 35]. In the regime of the NFL resistivity, Ritz *et al.* observed an additional contribution to the Hall signal suggesting that spin correlations with non-trivial topology may be responsible for the breakdown of Fermi liquid theory [36]. A candidate for these spin correlations are topologically protected spin whirls, referred to as skyrmions, showing a similar topological Hall signal [37,38]. Skyrmions were first observed in MnSi at ambient pressure and with applied magnetic field via small angle neutron scattering (SANS) [39]. The discovery of the skyrmion lattice [39], representing a new type of magnetic order, further boosted the scientific interest in itinerant helical magnets. Topological protection in combination with a low power consumption for modifying the spin arrangement makes these materials interesting for future applications in ultra-dense data storage, spintronics, or for magnetic structures on the nanoscale [38, 40–43].

In the phase diagram of MnSi, the skyrmion pocket is enclosed by the helimagnetic, the conical and the fluctuation disordered state. Similar to the CDW transition discussed above, fluctuations play also an important role in spin systems. Initially, the phase transition from paramagnetism to helimagnetism was considered to be

second order as expected from mean field theory and compatible with most of the experiments [32, 44, 45]. However, these findings were questioned in early electron spin resonance (ESR) experiments [46] and it was found recently that the transition is indeed first order [47,48]. In a scenario, first considered by Brazovskii [49], isotropic chiral fluctuations inhibit the phase transition until it becomes first order at a reduced transition temperature T_C [48]. The intensity of the critical fluctuations is distributed almost uniformly on a sphere in momentum space, meaning that the length of the ordering vector, corresponding to the pitch of the helix, is already fixed above T_C while the ordering direction is not. In a magnetic field, the fluctuations are quenched and the phase transition reverts to conventional second order at a field-induced tricritical point [50].

The onset of helimagnetic order has of course a broad impact on the physical properties. For instance, the optical conductivity and the effective mass of the charge carriers were studied as a function of frequency and temperature via infrared spectroscopy [51]. Mena *et al.* find that the optical conductivity cannot be described by the standard Drude formalism in the helical phase below T_C. Rather, the measurements are compatible with a phenomenological approach developed for materials having a strongly anisotropic scattering rate or showing non-Fermi liquid (NFL) behaviour [52]. Conventional transport, however, rules out NFL behaviour without applied pressure [32]. Indeed, anisotropic electron scattering can be expected in MnSi where multiple bands form a complex multi-sheeted Fermi surface [53,54]. In contrast, a momentum independent carrier lifetime is assumed in the theoretical description of the topological Hall effect present in the skyrmion phase [37, 55, 56].

An experimental probe that provides some momentum resolution could overcome the limitations of conventional and optical transport measurements and thus can be extremely useful to address the type of questions raised above. Raman spectroscopy can meet these requirements. Via the Raman selection rules, excitations of different symmetries can be detected independently, and separate regions of the Brillouin zone can be probed [57]. The impact of phase transitions on optical phonons can be studied as well as the anisotropy of charge- [19,58] or spin-fluctuations [59]. Moreover, electronic properties [57] such as the **k**-dependence of the carrier relaxation rates or the CDW energy gap can be investigated.

However, the low scattering cross section in MnSi hampered inelastic light scattering below room temperature up until now. In a major effort during this dissertation,

the optical setup for Raman scattering measurements was augmented facilitating experiments at low temperature, in magnetic fields and at high pressure.

The thesis is organized as follows: Chapter 2 compiles the relevant concepts of electronic Raman scattering, before detailing the Raman and high pressure facilities largely built up during this work. In Chapter 3, an introduction to CDWs and the material class of rare-earth tritellurides is given. Specifically, the Raman results on collective excitations of the CDW amplitude, charge fluctuations above the phase transition and the anisotropy of the CDW energy gap are discussed. Chapter 4 briefly introduces the magnetic phases and the crystal structure of MnSi. A short review of optical conductivity results precedes the discussion of the Raman results which include the temperature dependence of the phonons, signatures of fluctuations above T_{C} and the temperature and symmetry dependence of electronic excitations. Chapter 5 summarizes the results.

Chapter 2

Experiment

2.1 Theoretical concepts

This section is intended to be a brief compilation of concepts used later in this thesis but not a pedagogical introduction to Raman scattering. It covers only Raman scattering from electrons including symmetry arguments and selection rules. As an exception, the effective mass approximation for Raman scattering is described in some detail. The theoretical description is adopted mainly from the review article by Devereaux and Hackl [57] where a more detailed description can be found.

2.1.1 Electronic Raman scattering

Electronic Raman scattering measures the cross section for scattering of photons off electrons in a solid. Typically one is interested in the scattering from conduction electrons close to the Fermi surface. The number of scattered photons per second $\dot{N}(\omega, T)$ is proportional to the differential cross section [57, 60, 61]

$$\dot{N}(\omega, T) \propto \frac{\partial^2 \sigma}{\partial \Omega \, \partial \omega_s} = \hbar r_0^2 \, \frac{\omega_s}{\omega_i} \, \mathcal{R} \tag{2.1}$$

which is determined by the probability that an incident photon of frequency ω_i is scattered into a solid angle interval between Ω and $\Omega + d\Omega$ and a frequency window between ω_s and $\omega_s + d\omega_s$. Here, $r_0 = e^2/4\pi\varepsilon_0 mc^2$ is the Thompson radius of an electron, and $\mathcal{R}$ the transition rate determined via the Fermi golden rule,

$$\mathcal{R} = \frac{1}{\mathcal{Z}} \sum_{I,F} \exp^{-\beta E_I} \, |M_{F,I}|^2 \, \delta(E_F - E_I - \hbar\omega). \tag{2.2}$$

Here, $\mathcal{Z}$ is the partition function and $\beta = 1/k_{\mathrm{B}}T$. $M_{F,I} = \langle F|M|I\rangle$ is the matrix element for the transition from the initial to the final state due to the effective light scattering operator M that contains the photon-electron interaction; the transferred energy $\hbar\omega = \hbar\omega_i - \hbar\omega_s$ is referred to as Raman shift. For a general discussion of the matrix element $M_{F,I}$ the reader is referred to Ref. [57]. At this point, symmetry arguments and simplifying assumptions have to be applied to arrive at treatable solutions.

2.1.2 Symmetry and light polarizations

The charge-density fluctuations induced by the light scattering process, basically, have the symmetry imposed by the polarization direction of incident and scattered photons. Thus, the light polarizations $\hat{\mathbf{e}}_{\mathrm{i},s}$ are the key to access the symmetry properties of excitations in the sample. Methods of group theory are applied to classify the polarization dependence of the Raman response. It has been shown that the matrix element $M_{F,I}$ can be decomposed into basis functions of the irreducible point group of the crystal [60], meaning that the contributions to $M_{F,I}$ can be decomposed into different symmetries which can be accessed with appropriate light polarizations [57]. In case of cubic symmetry (point group O) the decomposition[1] can be written as

$$\begin{aligned} M_{F,I} \;&= \mathcal{O}_{A1}(e_i^x e_s^x + e_i^y e_s^y + e_i^z e_s^z) \\ &+\mathcal{O}_E^{(1)}(2e_i^z e_s^z - e_i^x e_s^x - e_i^y e_s^y) \;+\; \mathcal{O}_E^{(2)}(e_i^x e_s^x - e_i^y e_s^y) \\ &+\mathcal{O}_{T1}^{(1)}(e_i^x e_s^y - e_i^y e_s^x) \;+\; \mathcal{O}_{T1}^{(2)}(e_i^y e_s^z - e_i^z e_s^y) \;+\; \mathcal{O}_{T1}^{(3)}(e_i^z e_s^x - e_i^x e_s^z) \\ &+\mathcal{O}_{T2}^{(1)}(e_i^x e_s^y + e_i^y e_s^x) \;+\; \mathcal{O}_{T2}^{(2)}(e_i^y e_s^z + e_i^z e_s^y) \;+\; \mathcal{O}_{T2}^{(3)}(e_i^z e_s^x + e_i^x e_s^z). \end{aligned} \tag{2.3}$$

Thereby, the light polarizations $e_{i,s}^{x,y,z}$ are connected with the symmetry contributions to the matrix element. The projected operator $\mathcal{O}_\mu$ for the symmetry μ describes the light-matter interaction and also includes normalization factors.

The pure symmetries cannot be accessed individually by a single set of polariza-

[1] Point group O was used for the symmetry decomposition in MnSi, although its space group $P2_13$ corresponds to the point group $\mathcal{T}$ (23) [62]. However, $\mathcal{T}$ (23) contains only the three irreducible representations A, E, and T implying that, e.g., $x'y' + xy - rl \equiv 0$. In Experiment, this holds true only for the phonons (cf. Ref. [63]) but not for the continua having a strong antisymmetric component $xy + x'y' - rl = 2T_1$ [see Fig. 4.10]. A distinction between the symmetric T_2 and antisymmetric T_1 contributions is only possible in the next higher point group O with the replacements $A \to A_1$, $E \to E$, and $T \to T_2$ [64].

tions, but only in sums of at least two irreducible representations (i.e. symmetries). For the six polarization combinations used in the following, this reads [65]:

$$\begin{aligned} xx &= A_1 + \tfrac{4}{3}\,E & xy &= T_1 + T_2 \\ x'x' &= A_1 + \tfrac{1}{3}\,E + T_2 & x'y' &= E + T_1 \\ rr &= A_1 + \tfrac{1}{3}\,E + T_1 & rl &= E + T_2 \end{aligned} \tag{2.4}$$

To simplify the notation, the measurement configuration is given in Porto notation, e.g. $e_i^x e_s^x$ is abbreviated as xx. Here, x and y label polarizations aligned with the crystal axes of the cubic unit cell, x' and y' are rotated by 45° with respect to these axes, and r, l denote right and left circularly polarized light, respectively. If two spectra of each line in Eq. (2.4) are added up, the entire response is obtained. Consequently, the three sums should return the same result and therefore can be used to check the consistency of the measurements (Figs. 3.15, 3.16 and 4.10).

Via linear combinations of measured spectra the response of an individual symmetry can be obtained

$$\begin{aligned} A_1 &= \tfrac{1}{3}[(xx + x'x' + rr) - (x'y' + rl)] \\ E &= \tfrac{1}{3}[(xx + x'y' + rl) - \tfrac{1}{2}(xy + x'x' + rr)] \\ T_1 &= \tfrac{1}{3}[(xy + x'y' + rr) - \tfrac{1}{2}(xx + x'x' + rl)] \\ T_2 &= \tfrac{1}{3}[(xy + x'x' + rl) - \tfrac{1}{2}(xx + x'y' + rr)]. \end{aligned} \tag{2.5}$$

The system of equations is over-determined, and already a subset of four measured spectra is sufficient to calculate the pure symmetries, e.g. $E = (x'y' + rl - xy)/2$. In practice, however, it was useful to compare the symmetry decompositions obtained from different combinations of orientations to ensure the consistency of the results. The pure symmetries provide information on, e.g., phonon symmetry, collective modes or spin excitations. In the case of electron-hole excitations, different parts of the Brillouin zone can be accessed separately, thus facilitating a finite **k**-resolution [57,66].

2.1.3 The effective mass approximation

For quantitative predictions it is necessary to simplify the expression for the Raman scattering cross section [Eqs. (2.1) and (2.2)]. To this end, only single-particle excitations in weakly interacting systems are considered. Accounting only for Bloch electrons, indexed by momentum quantum numbers, the Raman transition rate $\mathcal{R}$ [cf. Eq. (2.2)] simplifies to the Raman density-density correlation function $\tilde{S}$ connected to the effective Raman susceptibility $\tilde{\chi}$ via the fluctuation dissipation theorem [67,68],

$$\tilde{S}(\mathbf{q},\omega) \;=\; -\frac{1}{\pi}\,\left[1+n(\omega,T)\right]\,\tilde{\chi}''(\mathbf{q},\omega) \tag{2.6}$$

with $n(\omega,T)$ being the Bose-Einstein distribution, and

$$\tilde{\chi}(\mathbf{q},\omega) \;=\; \langle\langle\,[\tilde{\rho}(\mathbf{q}),\tilde{\rho}(-\mathbf{q})]\,\rangle\rangle_{\omega}. \tag{2.7}$$

Here, $\langle\langle\,\rangle\rangle$ denotes a thermodynamic average [57]. The Raman density $\tilde{\rho}$ reads

$$\tilde{\rho}(\mathbf{q}) \;=\; \sum_{\mathbf{k},\sigma}\gamma(\mathbf{k},\mathbf{q})\;c^{\dagger}_{\mathbf{k}+\mathbf{q},\sigma}\,c_{\mathbf{k},\sigma}. \tag{2.8}$$

The scattering amplitude γ is determined from the Raman matrix elements $\gamma_{\alpha,\beta}$ (Raman vertex) and the polarizations of incident and scattered photons,

$$\gamma(\mathbf{k},\mathbf{q}) \;=\; \sum_{\alpha,\beta}\gamma_{\alpha,\beta}(\mathbf{k},\mathbf{q})\;e_i^{\alpha}\,e_s^{\beta}, \tag{2.9}$$

with

$$\begin{aligned}\gamma_{\alpha,\beta}(\mathbf{k},\mathbf{q}) \;=\; \delta_{\alpha,\beta} \;+\; \frac{1}{m}\sum_{\mathbf{k}_\nu}\Big(&\frac{\langle\mathbf{k}+\mathbf{q}|\,p_s^{\beta}\,|\mathbf{k}_\nu\rangle\langle\mathbf{k}_\nu|\,p_i^{\alpha}\,|\mathbf{k}\rangle}{E_{\mathbf{k}}-E_{\mathbf{k}_\nu}+\hbar\omega_i}\\ &+\;\frac{\langle\mathbf{k}+\mathbf{q}|\,p_i^{\alpha}\,|\mathbf{k}_\nu\rangle\langle\mathbf{k}_\nu|\,p_s^{\beta}\,|\mathbf{k}\rangle}{E_{\mathbf{k}+\mathbf{q}}-E_{\mathbf{k}_\nu}-\hbar\omega_s}\Big),\end{aligned} \tag{2.10}$$

$p^{\alpha}_{i,s}=p^{\alpha}\,\exp(\pm i\mathbf{q}_{i,s}\cdot\mathbf{r})$ the momentum density, and $\alpha,\beta=x,y,z$. The $\delta_{\alpha,\beta}$ term arises from two-photon scattering in first order perturbation theory. It vanishes if the polarizations of incoming and scattered light are orthogonal and thus does not probe electron dynamics in which the charge density relaxes in a direction orthogonal to the incident polarisation direction [57]. The other terms arise from single photon scattering via intermediate states $\mathbf{k}_\nu$ in second order perturbation theory. These terms

involve different time orderings of photon absorption and emission which plays a role for anti-symmetric contributions to the Raman response as discussed in Sec. 2.1.4.

In the limit of small momentum transfer $q \to 0$ and assuming that the photon energies $\omega_{i,s}$ are small in comparison to the separation of the intermediate states $\mathbf{k}_\nu$ from the conduction band (initial state), $\omega_{i,s} \ll |E_{\mathbf{k}_\nu} - E_{\mathbf{k}}|$, the Raman vertex further simplifies to the well known effective mass approximation:

$$\gamma_{\alpha\beta}(\mathbf{k}, \mathbf{q} \to 0) = \frac{1}{\hbar^2} \frac{\partial^2 E_{\mathbf{k}}}{\partial k_\alpha \, \partial k_\beta} \tag{2.11}$$

In this approach, the Raman vertex depends on the second derivatives of the conduction band $E_{\mathbf{k}}$ projected by the polarization vectors of incoming and scattered light. Here, k_α and k_β are the momenta along the crystal axes a and b. Thus the curvature of the bands and the orientations of the light polarizations determine which carriers are involved in the scattering off electrons in different bands in the Brillouin zone. The effective mass approximation provides a powerful tool to study properties of the band structure, yet it is limited to small $\hbar\omega_{i,s}$ and $\omega \ll \omega_{i,s}$. At higher energy transfers the approximations becomes increasingly unjustified and resonance effects may appear as discussed in Sec. 2.1.4. In all Raman experiments described below, $R\chi''$ is plotted as a function of the energy shift ω, where R is a constant that absorbs experimental factors and takes care of the units.

2.1.4 Antisymmetric contributions to the Raman response

In general, the Raman response i.e. the Raman tensor has both symmetric and antisymmetric contributions which can, in principle, be separated. The antisymmetric contributions are negligible in many cases such as phonons or nearly free conduction electrons, but necessary for the analysis of anisotropic electron dynamics in strongly correlated systems [57, 69]. In magnetic crystals without inversion symmetry, the Dzyaloshinskii-Moriya interaction, i.e. the antisymmetric part of the spin-spin interaction [27], is different from zero. As a result, canted spin arrangements like helical magnetic order occur in many cases [28, 70]. Excitations of such chiral objects are expected to appear in the antisymmetric part of the electronic Raman response [57]. Thereby, new insights into itinerant electron magnets like MnSi can be obtained.

However, chiral excitations are not the only origin of light detected in the antisymmetric channel. Contributions in the antisymmetric channel may also arise, if there

is either (i) a parasitic background from light sources other than the sample, or (ii) if $\hbar\omega_{i,s}$ is close to resonances, or (iii) if the angular momenta of the initial and the excited state are different. In the following these cases will be discussed.
(i) There are various possibilities for external light sources other than Raman scattering from the sample, such as fluorescence in the optical elements or residual light in the laboratory or a background signal of the CCD. However, a background problem can be excluded experimentally as described in Sec. 2.2.2.
(ii) Away from resonances when the photon frequencies $\omega_{i,s}$ can be neglected with respect to the gaps between the electron bands around the Fermi energy, the effective mass approximation [cf. Eq. (2.11)] applies. In the effective mass approximation no antisymmetric response [T_1 terms[2] in Eq. (2.3)] can be obtained [71] as the order of the partial derivatives of the conduction band is irrelevant, i.e. $\gamma_{ab} = \gamma_{ba}$. In a more general form of the Raman vertex including resonance effects [Eq. (2.10)], it does make a difference if incoming and scattered photons, ω_i and ω_s, are exchanged, particularly close to a resonance. As a result, the matrix elements are different, if the time order of photon absorption and emission is reversed and a finite intensity in the T_1 channel is expected. The T_1 contribution is only different from zero, if $\gamma_{\alpha\beta} \neq \gamma_{\beta\alpha}$, where $\alpha, \beta = x, y, z$. Large intensity may occur close to a narrow resonance.
(iii) If the angular momenta of the initial and the final states are different, an antisymmetric response can occur, for example in the case of crystal field excitations [65] as shown in Sec. 3.4.1. In 1990 Shastry and Shraiman [69] derived the magnetic Raman response for a Mott-Hubbard system and found that the spin chirality operator $\mathbf{S}_i \cdot (\mathbf{S}_j \times \mathbf{S}_k)$ couples to the light in linear order and has antisymmetric matrix elements[3]. Later Michaud, Vernay and Mila showed that this is not the case due to cancellation effects [72]. Nevertheless, scattering from chiral spin excitations is likely to be observed experimentally at least in Heisenberg magnets [73] and may come from higher order excitations or strong resonance enhancement. On the basis of the existing data these questions cannot be settled satisfactorily for any of the systems studied so far.

In summary, while contributions from residual light in the laboratory and from fluorescence can safely be excluded experimentally (cf. Sec. 2.2.2), it is not trivial to clearly distinguish if an antisymmetric Raman response originates from resonance

[2] In tetragonal systems A_{2g} is the antisymmetric channel.
[3] The spin chirality operator resembles the mathematical form of the Dzyaloshinskii-Moriya interaction.

effects or chiral excitations as will be discussed in Sec. 4.5.2.

2.2 Experimental setup and data analysis

The challenge of Raman scattering in metallic or even superconducting samples is the low scattering cross section due to the small light-matter interaction volume (penetration depth) in combination with the limited optical access to the sample located in the center of a superconducting magnet and, optionally, inside a diamond anvil pressure cell (cf. Sec. 2.3). A considerable part of this thesis was to set up an experiment capable of measuring weak Raman signals under these extreme conditions. In this section, the Raman experiment is described, the key components of the new setup are particularly emphasized, and details on the data analysis procedure are provided.

2.2.1 Light path

A schematic drawing of the experiment is shown in Fig. 2.1. As a light source either a Krypton ion laser (Coherent Innova 400, 14 discrete wavelengths between 406.7 and 799.3 nm are available) or a Nd-YAG diode-pumped solid state laser (Klastech Scherzo, $\lambda = 532\,\mathrm{nm}$) can be selected[4] via a removable mirror (RM). A pinhole system (PH1), consisting of a microscope objective lens, a circular aperture (20 µm) and an achromat, spatially filters the laser beam and expands the beam diameter. A prism monochromator (PM), designed and built during this dissertation, disperses the laser light. In combination with a slit, only monochromatic light of a selected wavelength can pass. In the range of green light, the device suppresses [74] all plasma lines that differ by more than about 0.9 nm ($30\,\mathrm{cm}^{-1}$) from the main laser line. In this way, radiative transitions in the Kr-plasma other than the lasing transition can be suppressed and do not appear as peaks in the spectrum superimposed to the Raman signal. A $\lambda/2$-plate together with a polarizer (P1) is used to reduce the power of the pre-polarized laser light. The final polarization state of the incoming photons is selected by polarizer P2 and a Soleil-Babinet compensator[5] which facilitates an independent access to polarization and phase of the incoming photons. As the incoming

[4] For economic reasons, mainly the solid state laser was used in the range of green light.

[5] The compensator consists of wedge-shaped birefringent crystals that can be rotated and shifted against each other in order to adjust the optical properties.

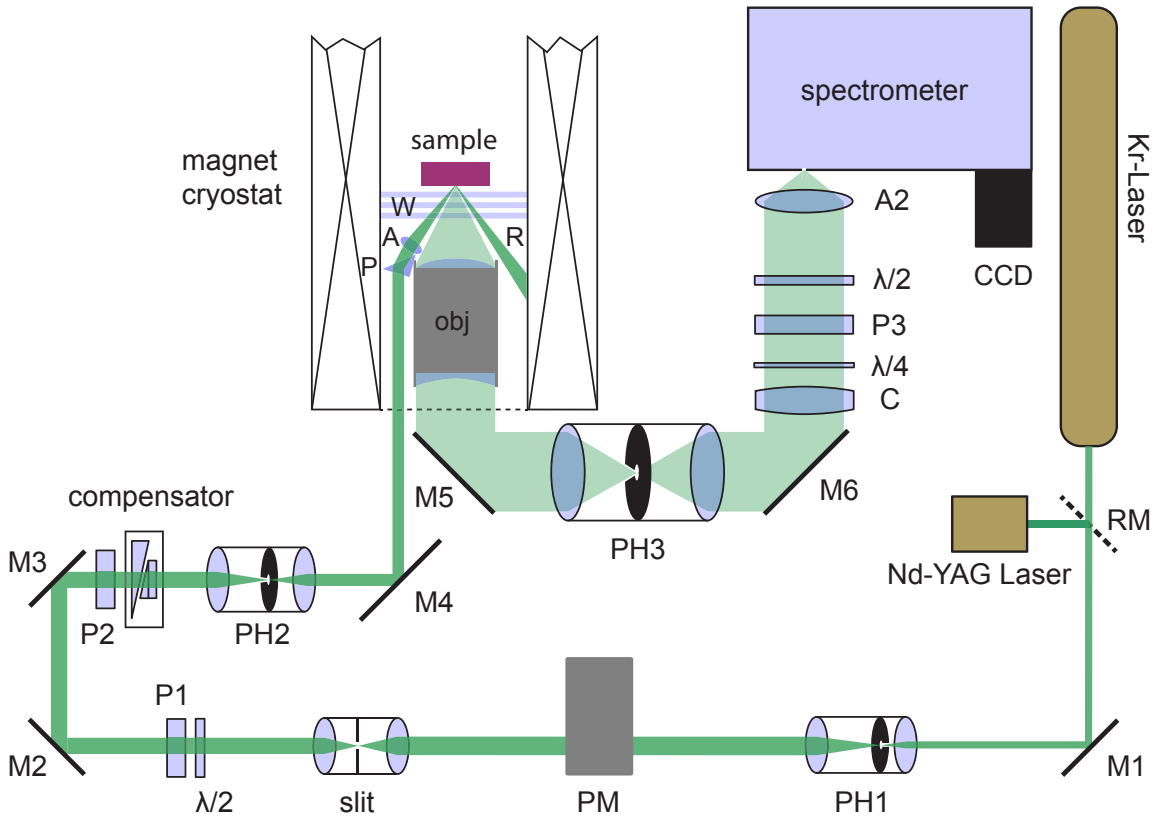

Figure 2.1: Schematic drawing of the Raman experiment. For details and description see text.

light is focussed on the sample surface at an angle of 30°, the absorption coefficients for light polarized parallel and perpendicular to the plane of incidence are different. As a result, circularly polarized light, e.g., assumes an elliptical polarization inside the sample. The compensator takes care of this problem as the light can be polarized elliptically outside the sample such that the absorbed light is circularly polarized inside. In this procedure, it is essential to know the complex index of refraction $\hat{n}$ which has to be determined experimentally for every sample and excitation wavelength. For a detailed description of the method, the reader is referred to Prestel *et al.* [75]. The next optical element in the light path is again a pinhole system (PH2) that spatially filters the beam and adjusts its diameter to the following optical components. Via a mirror (M4) the incoming beam is directed into the 41 mm warm bore of a solenoid superconducting magnet[6] providing fields up to 8 T. The light propagates in the ring-

[6]The specifications of magnet and cryostat are described in Ref. [76].

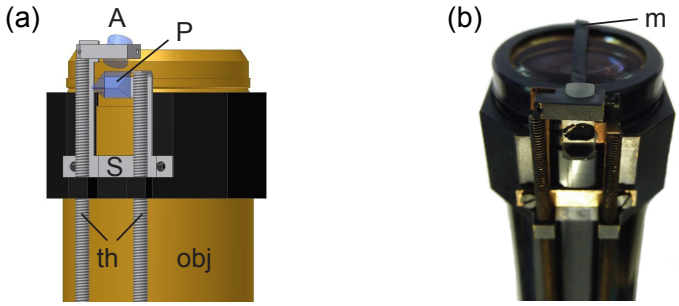

Figure 2.2: Drawing (a) and photograph (b) of the optics focussing the laser on the sample and the objective (obj) collecting the scattered light. The position of the achromat (A) and the prism (P) can be adjusted via threaded rods (th) pushing against springs (S). A metal strip (m) is positioned on top of the objective lens to block the laser light that is elastically reflected from the cryostat windows. All of it is located in the 41 mm bore of the magnet cryostat. Adapted from Ref. [77].

shaped gap between the bore and the objective lens and reaches a prism (P) and an achromat (A) directing and, respectively, focusing the photons on the sample. The optical components located in the bore of the magnet are depicted in Fig. 2.2. The photons reflected (R) from the sample surface cannot enter the collection optics, as their angle incidence is larger than the aperture angle of the objective lens (obj). To block the reflections from the cryostat windows (W), a thin black metal strip (m in Fig. 2.2) was placed on top of the objective lens (obj). Thereby, the amount of elastically scattered light reaching the detector is further reduced. The Raman light is collected by a custom-made objective lens[7] (obj) having a numerical aperture of $NA = 0.34$ (19.5°) which corresponds to a covered solid angle of 0.36 sr. For maximum throughput and best imaging properties, the lens corrects optical aberrations introduced by the cryostat windows (W) and the diamonds of the pressure cell described in Sec. 2.3. The spatial filter (PH3) in the path of the scattered light is one of the key components to suppress light that is not coming from the illuminated spot on the sample (cf. Sec. 2.2.2). A cylindrical lens (C) reduces the astigmatic aberration which is introduced by the gratings inside the spectrometer. Before the scattered photons are focussed on the entrance slit of the spectrometer the desired polarization states are selected with a quarter wave plate ($\lambda/4$) and an analyzer (P3). A $\lambda/2$-plate rotates the light polarization into the vertical direction where the spectrometer is most sensitive.

A triple-stage spectrometer (Jobin-Yvon T64000) in combination with a liquid ni-

[7]Designed and built by *Bernhard Halle Nachfl.* Optische Werkstätten GmbH, Berlin.

trogen cooled charge coupled device (CCD) is used to spectrally analyze the scattered light. The 2400 gr/mm gratings in the spectrometer have a dispersion of 0.5 nm/mm for light of 500 nm wavelength corresponding to roughly $0.5\,\mathrm{cm}^{-1}$ per pixel (25 µm) of the CCD detector. The spectrograph was calibrated using the lines of a neon calibration lamp. To this end, the entrance slit is set to 50 µm, and each single pixel column is read out separately referred to as binning one. As the entrance slit is imaged 1 : 1 on the CCD chip, there are two measured points (pixel columns) within the optical resolution being $1\,\mathrm{cm}^{-1}$ in this case. Rechecking the calibration several times per day, we find changes of less than $0.04\,\mathrm{cm}^{-1}$ which underscores that the instrument is practically stable. For the MnSi measurements, the focus of the scattered light has a size of roughly 150 µm on the entrance slit defining the minimum size of the slit in order to prevent a loss of signal. Consequently, the optical resolution is roughly $3\,\mathrm{cm}^{-1}$. The binning is set to 4, which corresponds to one measured point every $2\,\mathrm{cm}^{-1}$ in the spectrum. The main error source in the frequency determination is the position of the light focus on the entrance slit. A deviation of 40 µm from a perfectly centered position results in a frequency shift about $0.2\,\mathrm{cm}^{-1}$, defining the error bars of the measurements.

Observation optics

In addition to the efficiency of the collection optics, also the observation optics [76] was improved and adapted to the requirements of the new optical setup. Particularly in high pressure experiments (cf. Sec. 2.3) where the sample has a diameter of typically 100 µm, a high-resolution optical image is essential to select an appropriate spot for the laser focus on the sample surface. With a removable beam splitter, the experiment can be switched from measurement (Fig. 2.1) to observation mode (Fig. 2.3). Like in high quality optical microscopes, a Köhler illumination technique [78] is used to guarantee an evenly bright and high contrast image of the sample. To this end, two plano-convex lenses (L1) collect the light and image the filament (F′) of a lamp to the plane of aperture AP1. A second lens (L2) projects a magnified image (F″) of the filament on the back-focal plane of the objective lens (obj). The image can be considered as an extended light source and from each point of it a bundle of rays emerges. For example, this is sketched for one point in Fig. 2.3. Through the objective lens (obj) the image of the filament is perfectly defocussed. As the image of the filament fills the whole back-focal plane of the objective lens, the sample is

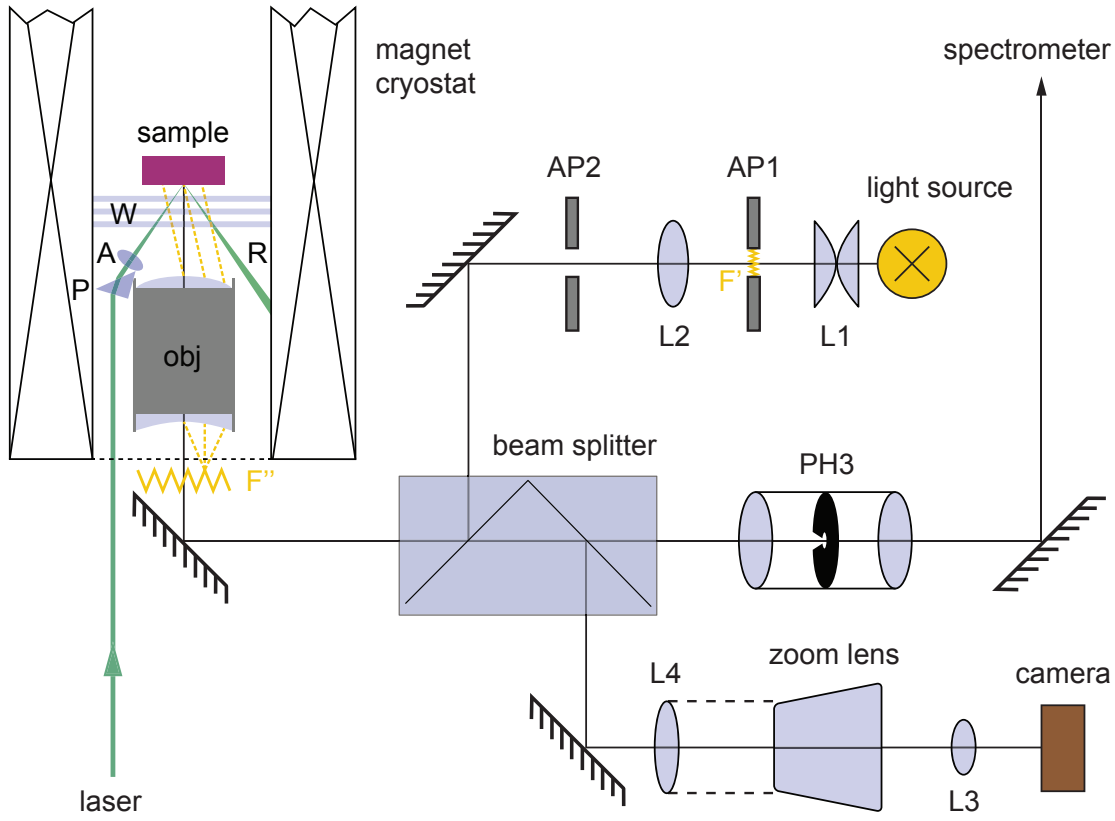

Figure 2.3: Optical setup to illuminate and observe small samples. For details see text.

illuminated with parallel light from many different angles. The apertures AP1 and AP2 control the maximum light angle, limited by the numerical aperture of the objective lens, and the illuminated area on the sample surface, respectively.

2.2.2 Background contributions versus Raman continuum

The optical setup described above is optimized for low scattering intensities and for suppressing light sources other than the sample like elastic reflections or fluorescence of optical components. The key components [79] are the bespoke objective lens (obj) in combination with the separate light paths for incoming and scattered photons and the spatial filter (PH3). In the following, the impact of the single components is briefly quantified. More details can be found in the in the diploma thesis of Peter Jaschke [77] associated to this work.

Fig. 2.4 (a) shows spectra of the Si phonon at $520\,\mathrm{cm}^{-1}$ measured with a commercial achromat (black) and with the new objective lens (red). The objective produced

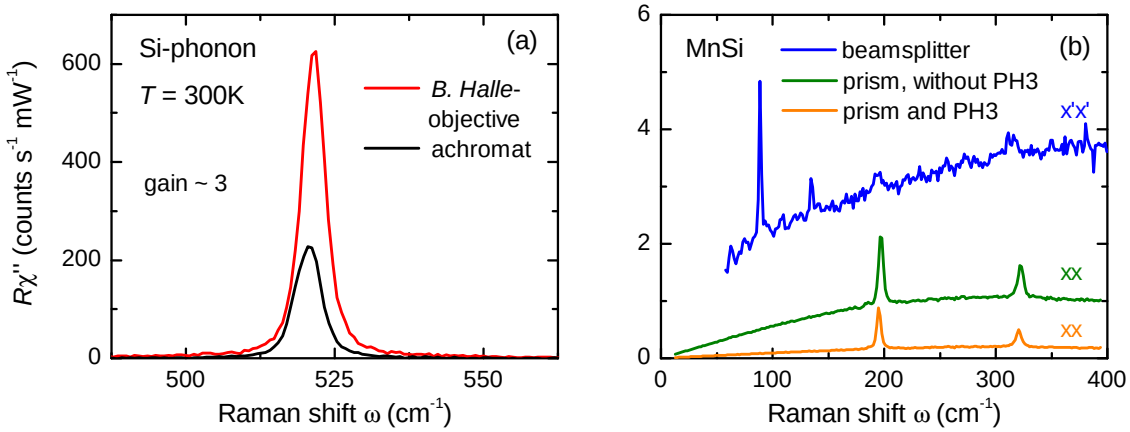

Figure 2.4: Comparison of different optical configurations. (a) With the *B. Halle* objective lens a factor of three in Intensity can be gained in comparison to a standard achromat. (b) Spectra obtained via different light paths are plotted together. The combination of prism and pinhole system yields the biggest suppression of undesirable background contributions.

by *B. Halle* collects about a factor of three more scattered photons than the standard achromat ($f = 60\,\mathrm{mm}$, $\emptyset\,30\,\mathrm{mm}$) used before. Panel (b) illustrates the suppression of stray-light and fluorescence, on the example of MnSi spectra. The response from the sample for $x'x'$ polarized light consists of A_1, $1/3\,E$ and T_2 contributions (cf. Sec. 2.1.2) with E phonons at $\sim 194\,\mathrm{cm}^{-1}$ and $\sim 319\,\mathrm{cm}^{-1}$ and T_2 phonons at $\sim 196\,\mathrm{cm}^{-1}$ and $\sim 314\,\mathrm{cm}^{-1}$ (cf. Sec. 4.4.1). If the sample is not illuminated via prism and achromat (cf. Fig. 2.1), but through a 10 : 90 beam splitter instead of mirror M5, the background contributions outshine the Raman light from the sample (blue spectrum). This is because the *B. Halle* objective lens is not only used to collect the scattered light, but also to focus the incoming laser on the sample. In this configuration, the incoming laser beam creates stray light in the objective lens. In addition, the elastic reflex from the sample passes through the optical components in the scattered light path and gives rise to fluorescence before it enters the spectrometer. The main background contributions, however, originate from the beam splitter and the calcite polarizer (P3 in Fig. 2.1) that is responsible for the strong peaks at 90 and $135\,\mathrm{cm}^{-1}$. If the sample is excited via the light path through prism (P) and achromat (A) but without pin hole PH3 (cf. Fig. 2.1), the green spectrum in Fig. 2.4 (b) is recorded. As xx polarization projects A_1 and $4/3\,E$ symmetry, the E phonons are more prominent in comparison to the $x'x'$ spectrum. The background is reduced by at least a factor of two, but still remains stronger than the signal from the sample. A spatial filter

(PH3 in Fig. 2.1) in the path of the scattered light further reduces the background. The continuous part of the spectrum drops by 80% from 1.1 ± 0.2 to 0.2 ± 0.05, while the phonon intensity is reduced by a factor of two (orange spectrum).

Another frequency dependent contribution to the background originates from the CCD detector. It was determined by measurements with closed shutter and the same exposure time as the experiment. If the Raman signal from the sample is below one count per second, such as in MnSi, the CCD background is not negligible, particularly at low frequencies. As the CCD background was stable, a smoothed mean value was subtracted from each measured MnSi spectrum. From the difference, the Raman response $R\chi''$ is obtained by dividing through the thermal Bose factor as shown in Fig. 2.5 [57].

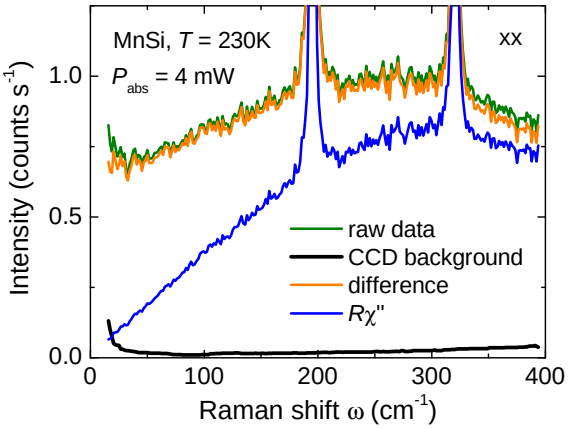

Figure 2.5: CCD background. The contributions are indicated and described in the text. Note that the spectra are not normalized to the absorbed laser power.

As a crosscheck for the new setup, we compared the spectra measured in the magnet cryostat close to back scattering conditions with those obtained in pseudo-Brewster geometry (described in Ref. [80] and references therein), where no laser light reaches the collection optics, and found good agreement. Altogether, the background issues can be considered under control and it is possible to distinguish an electronic Raman signal of about 0.1 inelastically scattered photons per second and milliwatt from parasitic background. For a typical integration time of 6 times 300 s and an absorbed laser power of 4 mW, this corresponds to about 700 photons reaching the detector in a frequency interval of $2\,\mathrm{cm}^{-1}$.

2.2.3 Fit procedure

In a next step, the electronic continuum is separated from phononic contributions. To this end, the phonons were fitted by standard Lorentzians for rare-earth tritellurides and by Voigt fits for MnSi. If the phonon width is comparable to the spectral resolution of the instrument, such as as in MnSi, the Lorentz response of the phonon is

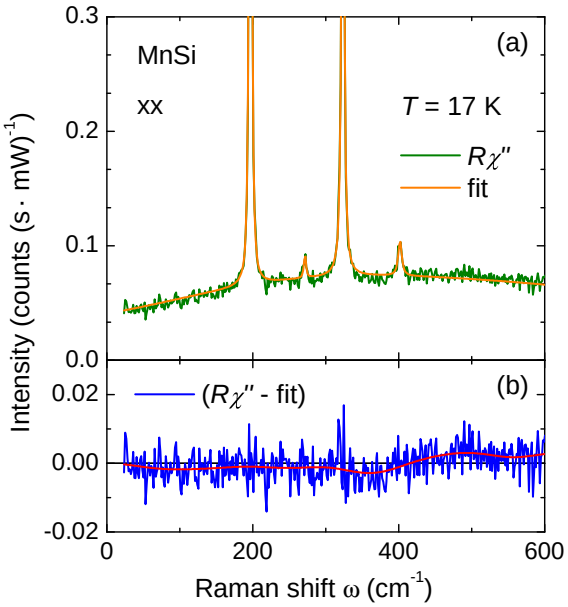

Figure 2.6: Demonstration of the data fitting for a MnSi xx spectrum at 17 K. Panel (a) shows the measured data (green) together with the fit function (orange) consisting of a 5th order polynomial and four Voigt shaped peaks. (b) shows the difference (blue) between measurement and fit. A smoothed curve (red) points out how much and at which frequencies the measurement and the fit differ beyond the noise level. To separate the phononic part from the electronic continuum, only the fits to the phonons are subtracted from the spectra.

convoluted with a gaussian profile due to the optical imaging inside the spectrometer. In the Voigt fit, the Gaussian width was fixed at the resolution being $2\,\mathrm{cm}^{-1}$. The width, position, and spectral weight of the Lorentzians are the fitting parameters and contain the physical information from the sample.

Fig. 2.6 shows a typical example. The Raman response $R\chi''$ of a MnSi xx spectrum (green) was fitted using Voigt profiles for the four phonons and a polynomial baseline (orange). The 5th order polynomial is anchored at 30 points which are distributed over the full energy range except for the vicinity of the phonon lines. Subtracting this polynomial puts the phonon peaks on a horizontal basis for the Voigt fit. In this example, the fit yields a position (Lorentzian width) of $196.8\,\mathrm{cm}^{-1}$ ($2.4\,\mathrm{cm}^{-1}$) and 323.3 ($3.7\,\mathrm{cm}^{-1}$) for the two strongest phonons, respectively. Panel (b) shows that the difference (blue) between the data and the fit is less than 0.005 counts $(\mathrm{s}\cdot\mathrm{mW})^{-1}$ for most points. The smoothed red line is a guide to the eye. On the one hand, the fit is used to determine the phonon frequencies (Lorentzian widths) with a precision of $\pm 0.2\,\mathrm{cm}^{-1}$ ($\pm 0.3\,\mathrm{cm}^{-1}$) for the large peaks and about $\pm 0.5\,\mathrm{cm}^{-1}$ ($\pm 0.6\,\mathrm{cm}^{-1}$) for

the low intensity phonons[8]. On the other hand, subtracting the phonons from the spectrum yields the electronic continuum of the Raman response which is used to obtain carrier properties [81] (cf. Sec. 4.5.2).

2.2.4 Temperature determination

The physical properties depend crucially on the temperature in the illuminated spot T_s. The absorbed light heats the sample locally and results in a difference ΔT between the holder temperature T_h and T_s, particularly at low temperatures. A precise temperature determination is essential, if the spectra of the studied sample strongly change in small temperature intervals which particularly may be the case close to a phase transition.

One common method to determine the amount of heating is to compare Stokes and anti-Stokes intensity, i.e. energy gain and energy loss spectra. They differ by an exponential factor due to thermal occupation which can, in principle, be used to calculate the temperature. However, this method is not always reliable, in particular at temperatures below 100 K and in materials with low scattering intensities, such as MnSi. As an alternative, strongly temperature dependent features in the spectra can be analyzed using combinations of various laser powers P_abs and holder temperatures T_h. Ideally, P_abs and T_h are selected in a way that the spectral features assume the same shape for at least two combinations. Then, if ΔT is moderate, one can expect that the spot temperatures are equal.

A third method uses the complex index of refraction $\hat{n}$ and thermal conductivity data to estimate the laser heating. It was developed for V_3Si [82, 83] where the strong temperature dependence of the gap mode in the superconducting state was used to determine the amount of laser heating. Knowing the amount of the absorbed light power and the thermal conductivity $\lambda(T)$ the complete temperature range of a material becomes accessible. It was shown that the method can be extrapolated to other materials, such as Nb_3Sn [83], having an isotropic heat conductivity. As MnSi is an isotropic metal, but has a low scattering intensity and no sufficiently temperature dependent features, the latter method is applied as described in the following [64].

Starting point is the equation for thermal conductivity in a semi-spherical geometry. The laser power P_abs is deposited within the illuminated spot with radius r_0. It is assumed that the complete energy is transferred to the sample holder via heat

[8]The size of the error bars and the stability of the experimental setup is addressed in Sec. 2.2.1.

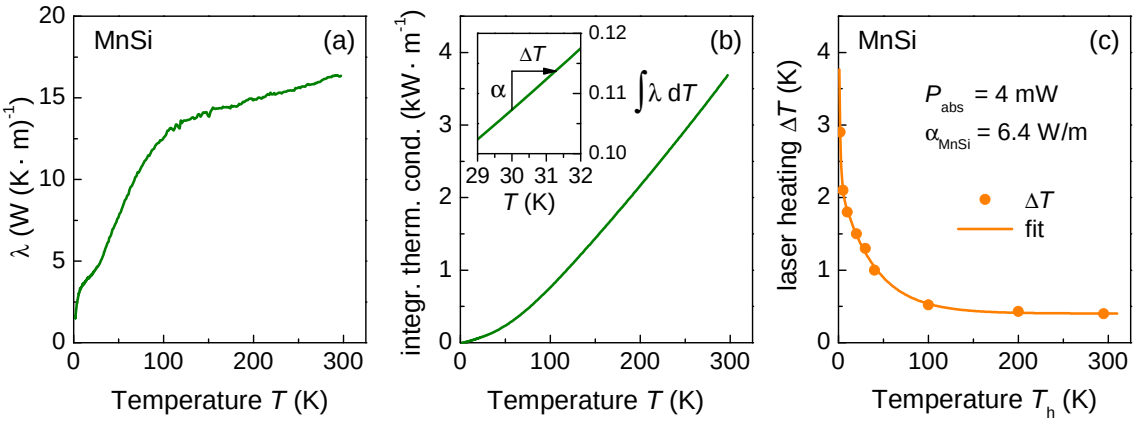

Figure 2.7: Thermal conductivity and laser heating in MnSi. (a) thermal conductivity measurement [64]; (b) integrated thermal conductivity. According to Eq. (2.13), the integral $\int \lambda dT =: \alpha$ from T_h to $T_\mathrm{h} + \Delta T$ is constant as long as the laser power and the focus size are not changed. For the experimental setup used here, α is 6.4 W/m for an absorbed laser power of 4 mW. The inset of (b) illustrates how ΔT can be obtained from α and the integrated conductivity. (c) the laser heating ΔT in the entire temperature range. Points are obtained from the integrated thermal conductivity as described in (b). An exponential fit was used to obtain ΔT in the full temperature range.

conduction in the sample. This is an excellent approximation for metals in both vacuum and gas atmosphere. In the case of transport in the metal, the heat flow through a shell with area $2\pi r^2$ and thickness dr is given by

$$P_\mathrm{abs} = -\lambda(T) \cdot 2\pi r^2 \frac{dT}{dr}, \tag{2.12}$$

where dT is the temperature drop across the radial increment dr. If the sample is large compared to r_0, integration yields [83, 84]

$$\alpha(P_\mathrm{abs}, r_0) := \frac{P_\mathrm{abs}}{2\pi\, r_0} = \int_{T_\mathrm{h}}^{T_\mathrm{h}+\Delta T} \lambda(T) dT. \tag{2.13}$$

$\Delta T = T_\mathrm{s} - T_\mathrm{h}$ is the average laser-induced heating. α depends only on r_0 and P_abs but not on any strongly temperature dependent property of the sample. Hence the knowledge in one sample, such as V_3Si, is sufficient for deriving ΔT in other isotropic compounds. The main non-trivial sample dependence comes from $\lambda(T)$ which has to be known in detail. Then ΔT can be determined for any T_h if the integral over $\lambda(T)$ is known (cf. Fig. 2.7).

In V_3Si, $\alpha_{V3Si} = 0.96\,\mathrm{W/m}$ was derived experimentally for an absorbed laser power

of 1 mW. For MnSi we used $P_{\mathrm{abs}} = 4.0\,\mathrm{mW}$ for all light polarizations. Differences in the optical setup of both experiments change the focus size by a factor of 0.6. Scaling α_{V3Si} with these changed experimental parameters results in $\alpha_{\mathrm{MnSi}} = 6.4\,\mathrm{W/m}$. As an example the graphical solution of Eq. (2.13) for the MnSi sample is shown in Fig. 2.7 (b). The experimental quantity $\alpha_{\mathrm{MnSi}} = 6.4\,\mathrm{W/m}$ for $P_{\mathrm{abs}} = 4\,\mathrm{mW}$ is added to the integrated thermal conductivity at the holder temperature T_{h}. Then, a horizontal line intersects the integral $\int \lambda dT$ at the spot temperature T_{s}. The length of this line is ΔT. In the example shown in the inset of Fig. 2.7 (b), $T_{\mathrm{h}} = 30\,\mathrm{K}$, $T_{\mathrm{s}} = 31.3\,\mathrm{K}$ and $\Delta T = 1.3\,\mathrm{K}$.

In the same way, the laser heating was determined for several holder temperatures between 2 and 300 K. These temperatures are indicated as points in Fig. 2.7 (c). At selected holder temperatures $T_{\mathrm{h}} = 2$, 30, and 300 K, ΔT is 2.9, 1.3, and 0.4 K, respectively ($P_{\mathrm{abs}} = 4\,\mathrm{mW}$). An exponential fit yields ΔT for all temperatures in between and was used to correct for the laser heating in all MnSi spectra presented in this thesis. In the following, T_{s} is referred to as T for simplicity.

2.3 High pressure technique

Pressure is an important parameter for tuning material properties making high pressure techniques powerful tools. By applying pressure, the unit cell volume of a crystal can be reversibly tuned affecting the physical properties. With the distance between atoms also the overlap of atomic orbitals is changed. Phase transitions can be induced or prevented by pressure, such as superconductivity in the cuprates [85, 86] or charge density wave order in the rare-earth tritellurides (cf. Sec. 3.4.2).

In the course of this thesis the diamond anvil cell designed and built by Leonardo Tassini [87], was carried over from the test phase to standard operation in the laboratory. A second pressure cell and gas handling system with improved operability was built. The new cell also allows susceptibility measurements at high pressure as described in Ref. [88]. Also, improved techniques for preparing the gasket and loading the cell were developed. In this section the new equipment and the principle of operation is briefly described. Finally, pressure determination and hydrostaticity in the cell are discussed.

2.3.1 The diamond anvil cell

Diamond anvil cells (DAC) are perfectly compatible with Raman scattering, as small sample sizes are sufficient and the diamonds are transparent in the spectral range of visible light. The operating principle of a DAC is sketched in Fig. 2.8. A pair of diamond anvils squeeze a metal gasket. The sample and a piece of ruby, as a pressure gauge, are placed in a hole in the gasket filled up with a (hydrostatic) pressure medium. By applying force on the diamonds pressure is generated.

The DAC actually used is illustrated in Fig. 2.9. Here, the force is generated via a stainless steel membrane that bends when it is filled with pressurized He gas through a capillary. The flexible part of the membrane has a diameter of 2.5 cm and thus applies a force of roughly 50 N per 1 bar He pressure to the piston, assuming that it touches the piston on its whole area. The culet, i.e. the flattened tip of the diamond anvil, has a diameter of 600 µm. Due to the ratio of the two areas, the pressure is enhanced by a factor of about 1700. The maximum He gas pressure in the membrane is 130 bar and hence corresponds to an applied force of 6500 N which is translated into a pressure of roughly 23 GPa at the culet. Since only a part of the membrane touches the piston, the maximum pressure reached in experiment was 18 GPa with a He pressure of 125 bar in the membrane. For the huge force, the diamonds have to be supported by tungsten carbide anvils, since otherwise the supporting CuBe of the pressure cell may be indented. The bottom anvil is a flat disc that can be shifted laterally, the top one is hemispherical and can be tilted. Together they are used to align the diamond culets laterally up to a precision of about 10 µm and parallel up to a few angle-minutes. The angle between the two touching culets was determined by the interference pattern of light reflected from these two diamond surfaces. When the diamonds are pressed against each other, the movement is guided by four hardened copper beryllium aligning pins. The accuracy of the alignment is limited by the tolerance of the alligning pins[9] which is of order 10 µm. To avoid

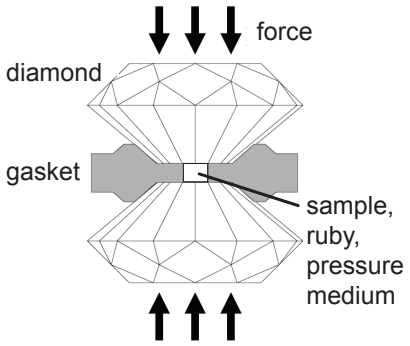

Figure 2.8: Working principle of diamond anvil cells. Drawing adapted from [89].

[9] To reduce the friction on the aligning pins, they were lubricated with molycote microsize powder (MoS_2).

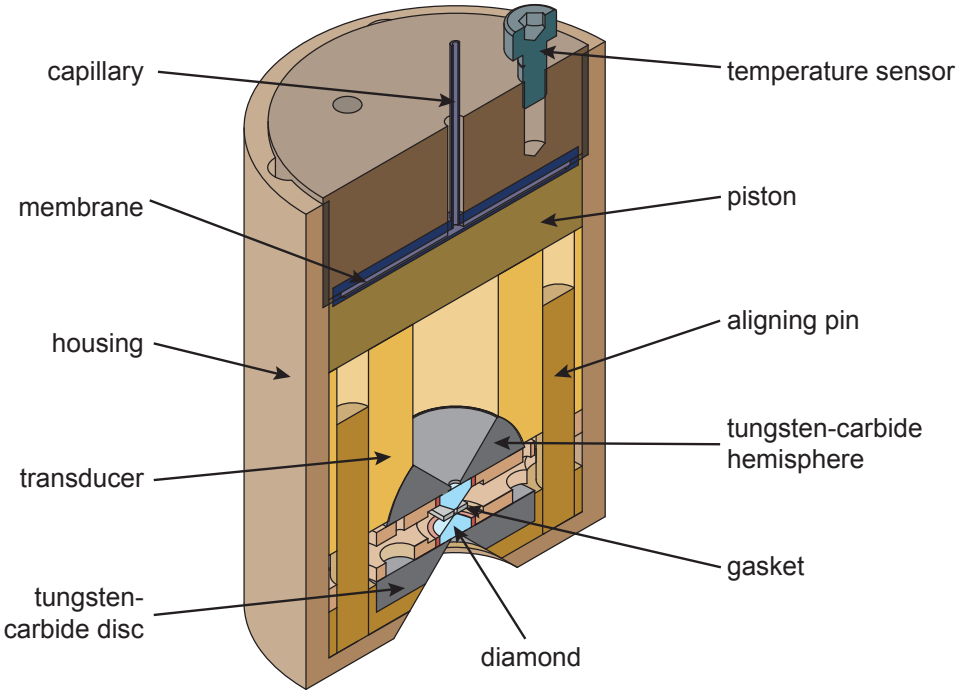

Figure 2.9: Schematic drawing of the diamond anvil cell. Courtesy of Leonardo Tassini.

a blocking of the DAC at low temperatures due to thermal expansion effects, it is important to use the same material for the pins as for the rest of the cell. The temperature is measured by a Cernox CX-1050-MT-1.4L metal oxide resistor, calibrated in the range from 1.4 to 325 K with an accuracy between ±5 and ±40 mK. It can also be used in magnetic fields, as the magneto-resistive effect $\Delta T(B)/T$ is smaller than 0.4% for $4.2 < T < 300$ K in a magnetic field of 8 T. The Cernox resistor is located roughly 3.5 cm above the sample which leads to a temperature gradient[10] of less than 1 K between sensor and sample, if temperature is changed at a rate of $\sim$1 K/min [88].

In DAC experiments, the gasket plays an important role. It is a "soft" buffer layer that prevents the diamonds from touching, but the material has to be strong enough to maintain a sufficiently thick final layer between the diamonds at the highest pressures [90]. The gasket guides the diamonds, provides a ring anchor around the diamond culets and reduces the strain in the culets [91]. Most importantly, it confines the pressure transmission medium (here, helium was used exclusively) and thus facilitates measurements in hydrostatic conditions. All experiments in the following

[10]The temperature gradient in the pressure cell was determined from the shift of the superconducting transition in $YBa_2Cu_3O_{7-x}$ as a function of increasing and decreasing temperature [88].

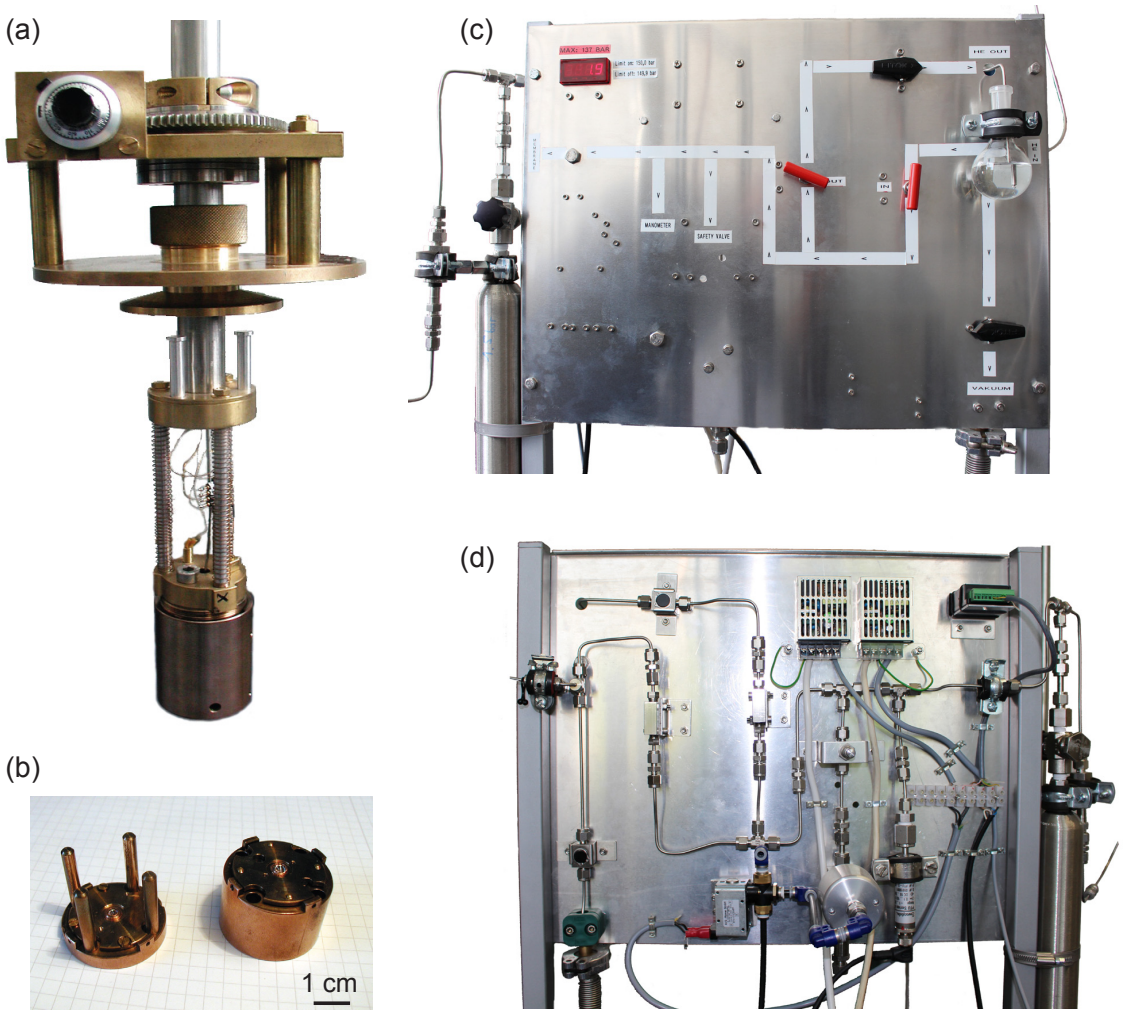

Figure 2.10: Photographs of the high pressure equipment built up during this dissertation. (a) dip stick with pressure cell, (b) open pressure cell, and (c, d) the gas handling system (front- and back-view) to adjust the applied pressure.

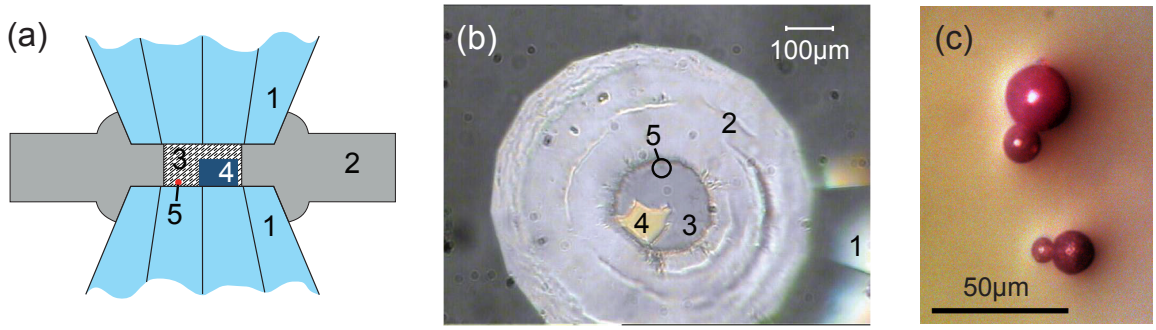

Figure 2.11: Volume under pressure. (a) section through the DAC (side view). (b) view through the bottom diamond into the cell using the observation optics. 1 diamond; 2 gasket; 3 pressure transmission medium (helium); 4 sample ($LaTe_3$); 5 ruby [not resolved in (b)]. (c) ruby spheres.

were performed with stainless steel gaskets as it has suitable mechanical properties and a high electrical resistivity that reduces eddy currents upon changing the external magnetic field. This property becomes particularly important, if ac susceptibility measurements are intended to be performed [88]. In addition, it is important that the material remains non-magnetic and non-superconducting down to low temperature.

The gaskets were cut from a 250 µm thick foil, mounted in the DAC and pre-indented to a thickness of roughly 50 µm. In the center of the 600 µm wide indent, a 300 µm hole was machined using spark erosion technique. The indented region has to be free of micro-cracks to confine the helium in the volume under pressure, and the hole should be perfectly circular and exactly centered to within a precision of 10 µm in order to distribute the pressure load uniformly. To this end, an improved setup for electrical discharge machining was built up during this dissertation. For details, the reader is referred to the bachelor thesis of Georg Haunschild [92].

The pressure cell can be operated in the magnet cryostat of the Raman setup described above. In fact, the optics was adapted to the requirements of high pressure experiments. The accessible parameter range is 0 – 20 GPa in pressure, 0 – 8 T in magnetic field, and 2 – 310 K in temperature. The cryostat is also used to load the cell with helium serving as the pressure transmission medium. To this end, gasket, sample, and ruby are placed on the diamonds, and the cell is closed almost completely except for a gap of roughly 50 µm between the top diamond and the gasket. In the cryostat the DAC is submerged in superfluid helium that enters the sample space through the gap. Via the gas handling system and the stainless steel membrane, a force is applied to the top diamond, and the cell is closed trapping ruby, sample

and the superfluid helium inside. With the cell, also the membrane is submerged in superfluid helium and the He gas inside liquifies as well. More gas has to be fed through the capillary to keep the pressure up. The big volume change associated with gas-liquid phase transition in the membrane was buffered by a much larger helium gas volume at room temperature. Besides improving the operability, the buffer volume also helps to avoid pressure shocks that may result in breaking the diamonds. Additional safety measures in the gas handling system are a burst disc that limits the pressure to 197 ± 10 bar and an electronically controlled safety valve that is triggered by a pressure sensor at 150 bar, but would close again below 145 bar to avoid bigger shocks to the diamonds. Typically, the cell was closed with a force of 3500 N (70 bar in the membrane) in supercooled, superfluid helium between 3.5 and 4.0 K. At 70 bar and below ~ 2.8 K [93], the helium in the membrane becomes solid blocking the capillary and preventing further pressure changes. Apart from this limitation, the pressure in the cell can be changed in situ via the gas handling system even at low temperatures[11].

2.3.2 Pressure determination

The most direct way to determine pressure is via its definition, force per area. However, in the GPa range practical difficulties arise due to friction, strain, non-elastic deformation and thermal expansion; in addition, the gasket absorbs an unknown fraction of the load [94]. Thus, more sophisticated methods to determine high pressures were developed in the past decades [90]. Given that an optical access is available, ruby fluorescence is the most straightforward method [95].

First, the origin of the fluorescence spectrum will be discussed. Ruby, i.e. Al_2O_3 doped with 0.05% Cr^{3+} ions, has two strong absorption bands which can be optically pumped. The excited meta-stable states rapidly decay non-radiatively and populate the $^2T_1$ and ^2E states[12] [90,96]. The ruby R lines (red), that are used for the pressure determination, arise from the radiative transition to the ground state; $^2E \rightarrow {}^4A_2$. The two-fold degeneracy of the ^2E-level is lifted by spin-orbit coupling, resulting in a pair of levels $E_{3/2}$ and $E_{1/2}$ corresponding to the R_1 and R_2 lines at 694.2 nm and, respectively, 692.7 nm at room temperature and atmospheric pressure. An increase

[11] For safety reasons, the pressure was typically not changed below a temperature of 30 K in experiment.

[12] Note that in this subsection $^2T_1$, ^2E, $^4A_2$, $E_{3/2}$, and $E_{1/2}$ do not refer to crystal symmetries, but label spectroscopical term schemata of the Cr^{3+} ion.

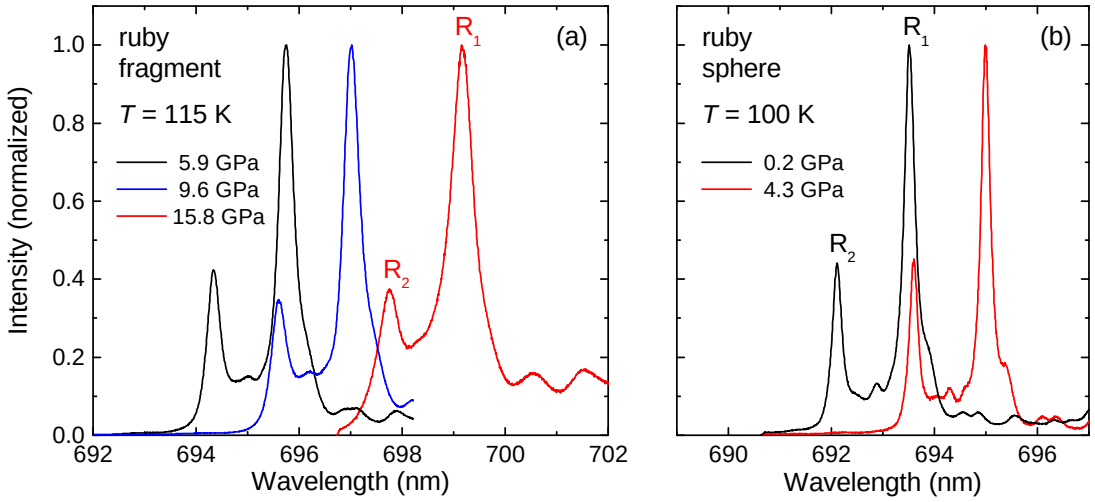

Figure 2.12: Ruby fluorescence at various pressures. (a) ruby spheres, (b) ruby fragments. The pressure can be calculated from the frequency of the R_1 line and the temperature. Hydrostaticity can be judged from the peak widths and the separation of the two strong ruby lines $\Delta R = R_1 - R_2$.

in pressure changes the local crystal field environment of the Cr^{3+}-ion which leads to a lowering of the transition energies and shifts both the R_1 and the R_2 line to larger wavelengths [90]. However, the separation of the two lines of $\Delta R = R_1 - R_2 = 1.5\,\mathrm{nm}$ ($\approx 30\,\mathrm{cm}^{-1}$) remains almost constant, if the pressure conditions are hydrostatic [97]. Spectra of (a) fragments of a synthetic ruby and (b) commercial ruby spheres provided by easylab Technologies Ltd. are plotted in Fig. 2.12.

The ruby as a pressure gauge was calibrated via x-ray measurements of the lattice constant of NaCl [98], Co, Mo, Pd und Ag [99] where the pressures are determined from an equation of state. This yields an empirical fit for pressures up to 80 GPa [100],

$$p(\lambda_{\mathrm{R1}}) = \frac{1904}{7.665}\left[\left(\frac{\lambda(p,\,T) - \Delta\lambda(T)}{\lambda_0}\right)^{7.665} - 1\right]\,\mathrm{GPa}. \tag{2.14}$$

Here, λ_0 is the position of the R_1-line at ambient pressure and room temperature. The shift $\lambda(p,\,T)$ is the observed ruby wavelength which depends both on pressure and temperature. To include the temperature dependence, the $\Delta\lambda(T)$ term was introduced. It is constant below 50 K and can be approximated by a polynomial at higher temperatures [101]:

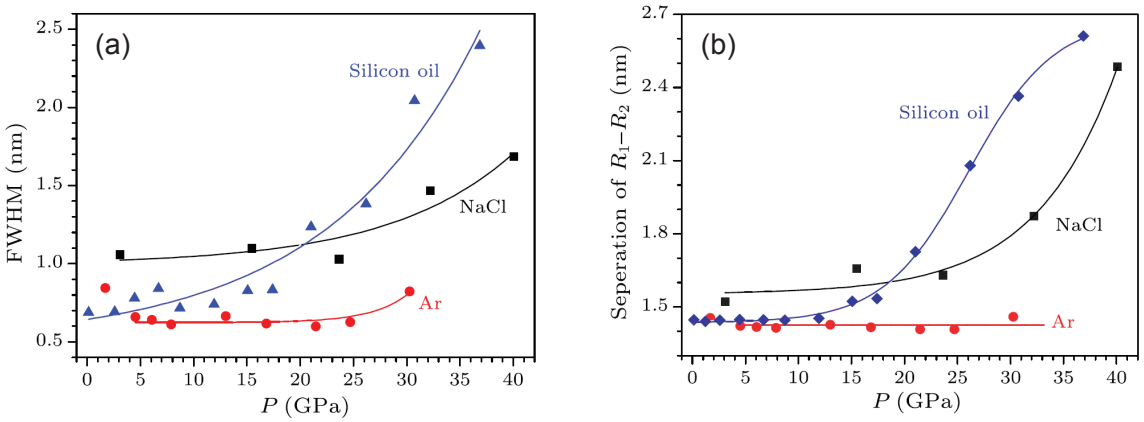

Figure 2.13: Comparison of different pressure transmission media from literature [102]. Both the width of the R_1-line (a) and the wavelength difference $\Delta R = R_1 - R_2$ strongly increase, if the transmission medium becomes anisotropic with increasing pressure. Solid lines are guides to the eye.

$$\Delta\lambda(T < 50\,\mathrm{K}) = -0.877\,\mathrm{nm} \tag{2.15}$$

$$\Delta\lambda(50\,\mathrm{K} < T < 296\,\mathrm{K}) = 6.64 \cdot 10^{-3}\,\mathrm{nm/K} \cdot \Delta T + 6.76 \cdot 10^{-6}\,\mathrm{nm/K^2} \cdot \Delta T^2 - 2.33 \cdot 10^{-8}\,\mathrm{nm/K^3} \cdot \Delta T^3 \tag{2.16}$$

Here, $\Delta T = T - 296\,\mathrm{K}$. This temperature dependence leads to an overestimation of the pressure, if the ruby would be considerably heated by the excitation via the laser beam. However, the ruby in the cell is thermally well connected to the diamonds via the pressure transmission medium. Hence, for laser powers in the range of few mW, the heating does not induce measurable line shifts.

The ruby spectrum reacts sensitively to uniaxial components in the pressure. The deviations from hydrostatic conditions can be estimated from the spectral width of the R lines and and changes in $\Delta R = R_1 - R_2$ [97, 103, 104]. Previous to the discussion on the ruby measurements in our diamond anvil cell, an example of truly non-hydrostatic pressure conditions can provide a feeling for the size of the related effects. Fig. 2.13 shows a recent study on the width of the R_1 line and the line separation ΔR with increasing pressure in different transition media [102]. Both quantities stay rather constant in the hydrostatic regime but increase dramatically at high pressure values when the conditions become non-hydrostatic; using argon the pressure remains hydrostatic at least up to 30 GPa.

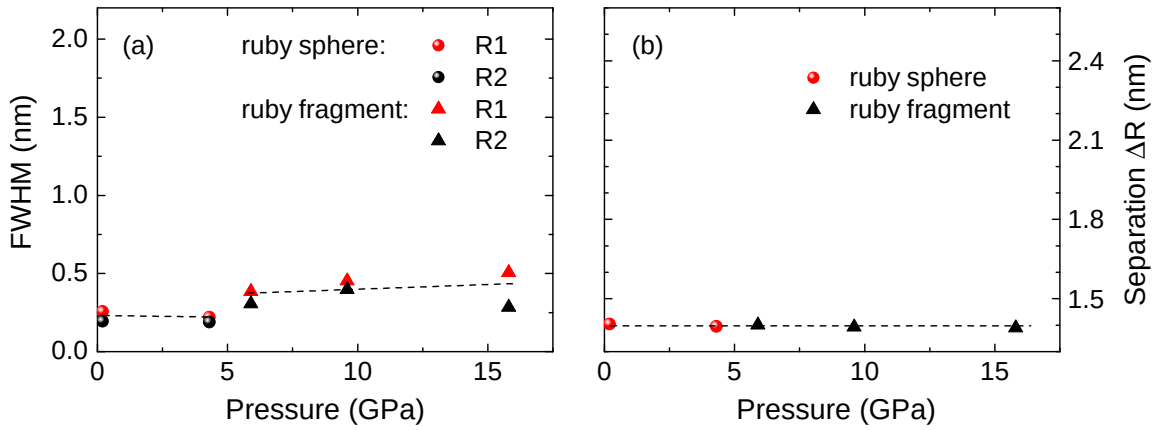

Figure 2.14: Check of the hydrostatic conditions in the helium loaded DAC. Width and separation of the R_1 and R_2 ruby lines shown in Fig. 2.12 are plotted as a function of pressure. The scale is comparable to that in Fig. 2.13. Dashed lines are guides to the eye. (a) The FWHM of both lines stays almost constant and well below the widths plotted in Fig. 2.13. The ruby spheres yield sharper fluorescence lines than the ruby fragments. (b) The separation $\Delta R = R_1 - R_2$ stays constant for pressures up to 15.8 GPa. Together, this indicates hydrostatic pressure conditions.

In our DAC, helium was used as the pressure transmission medium which is superior to argon concerning hydrostaticity, particularly at low temperatures [90, 105]. Fig. 2.14 shows the R_1-, R_2-linewidths and the line separation ΔR as obtained from the ruby spectra plotted in Fig. 2.12. All three quantities stay almost constant in the pressure range from 0 to 15.8 GPa indicating hydrostatic conditions inside the cell. The commercial ruby spheres have sharper fluorescence lines due to their superior crystal quality after annealing. The line separation ΔR, which may be the more reliable indication for a hydrostatic environment [97], is unaffected by the width of the two lines and stays pinned at a constant value of 1.4 nm. We do not find increases in linewidth or ΔR comparable to what is observed in non-hydrostatic conditions. Thus, it is safe to conclude that the conditions in the DAC used here are hydrostatic at least up to 15.8 GPa.

Chapter 3

Charge density waves in the rare-earth tritellurides

Rare-earth tritellurides ($R\mathrm{Te}_3$) turn out to be textbook examples and a laboratory for studying charge density wave systems. The are outstandingly clean, can be cleaved very easily and are tunable by chemical and applied pressure. The light scattering results add a variety of novel insights to collective excitations, charge order fluctuations and mechanisms beyond Fermi surface nesting contributing to the charge density wave (CDW) formation.

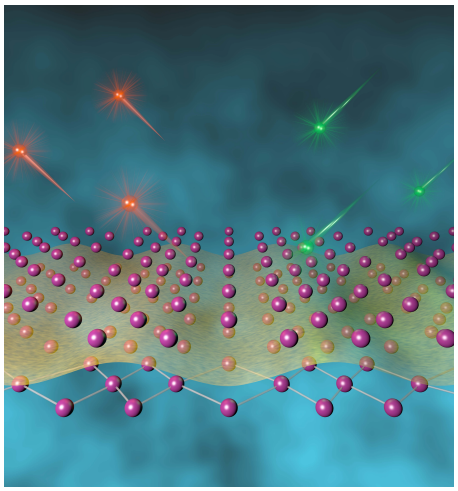

Figure 3.1: Bilayer of tellurium atoms distorted by a periodic modulation of the charge density (yellow). The complex interplay of the electrons with the lattice can be studied by inelastic light scattering (green, red) revealing an alternative mechanism for CDW formation.

3.1 Charge density waves - A brief introduction

This section provides a short introduction to CDW formation, since these general concepts will be used in the discussion. For a more detailed review, the reader is

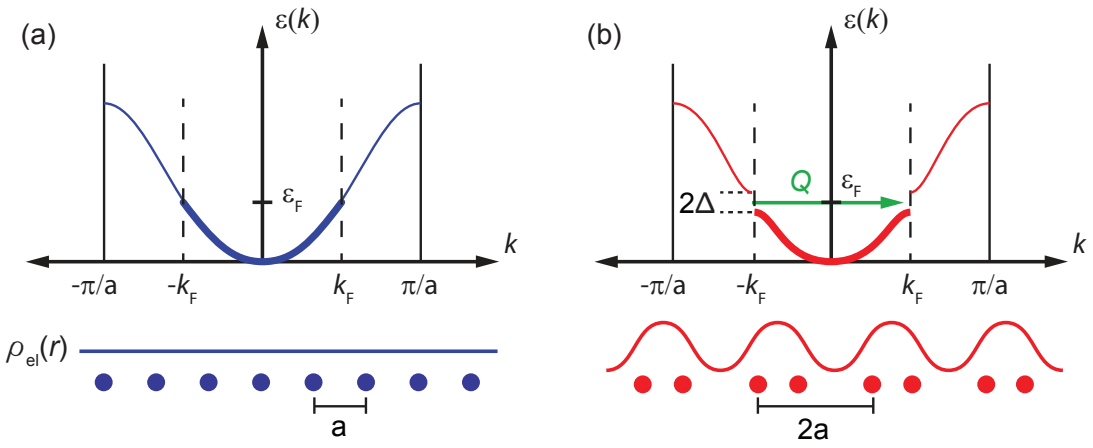

Figure 3.2: The Peierls transition. A one dimensional metal with a half filled electron band and a spatially uniform charge density distribution $\rho(r)$ (a) switches over to the CDW state (b); an energy gap 2Δ opens; the charge density is distributed in a wave like pattern which results in a periodic distortion of the linear chain of atoms. Adapted from [5].

referred to the textbook "Density Waves in Solids" by George Grüner [5].

Already in 1955, Rudolf Peierls pointed out that a one-dimensional metal at low temperatures is unstable against a periodic static lattice distortion together with a periodically varying charge distribution. Due to this new superstructure an energy gap opens at the Fermi surface turning the material into an insulator [5, 106]. Basically, the new broken symmetry ground state originates from a competition between elastic and electronic energy as a consequence of electron-phonon coupling. The periodicity of the CDW modulation is determined by the Fermi wave vector $\mathbf{k}_\mathrm{F}$ and thus depends on the band filling.

Fig. 3.2 illustrates the Peierls transition in a linear one-dimensional metal with a half filled energy band. In the normal state (a), the charge density $\rho(r)$ is constant and the atoms of the chain are evenly spaced with a lattice constant of a. When electron-phonon coupling is switched on, the CDW phase becomes the energetically favourable ground state. Opening up a gap 2Δ lowers the energy of the electrons close to the Fermi surface at the cost of a higher Coulomb repulsion in the ionic subsystem. In case of half filling, the ordering vector is $Q = 2k_\mathrm{F} = \pi/a$ and the periodicity[1] of the distorted lattice is $2a$. As Q depends on the band filling, the CDW modulation

[1]Due to the CDW superstructure, the Brillouin zone is reduced. This results in a backfolding of energy bands that can be detected by Raman scattering, e.g. additional phonon modes appear at $q \approx 0$ and finite energy.

is usually incommensurate, i.e. does not match the lattice periodicity.

Further, we consider how the low dimensional electron gas responds to a perturbation induced by a time independent potential

$$\phi(\mathbf{r}) = \int_q \phi(\mathbf{q})\, e^{i\mathbf{q}\cdot\mathbf{r}}\, d\mathbf{q}. \tag{3.1}$$

Within the framework of linear response theory, the induced rearrangement of the charge density

$$\rho_{\mathrm{ind}}(\mathbf{r}) = \int_q \rho(\mathbf{q})\, e^{i\mathbf{q}\cdot\mathbf{r}}\, d\mathbf{q} \tag{3.2}$$

reads

$$\rho_{\mathrm{ind}}(\mathbf{q}) = \chi_{\mathrm{L}}(\mathbf{q})\, \phi(\mathbf{q}). \tag{3.3}$$

Here, $\chi_L(\mathbf{q})$ is the (real part of) the Lindhard function in $d = 1, 2, 3$ dimensions

$$\chi_L(\mathbf{q}) = \int \frac{d\mathbf{k}}{(2\pi)^d} \frac{f(\epsilon_{\mathbf{k}}) - f(\epsilon_{\mathbf{k}+\mathbf{q}})}{\epsilon_{\mathbf{k}} - \epsilon_{\mathbf{k}+\mathbf{q}}}, \tag{3.4}$$

with $f(\epsilon_{\mathbf{k}})$ the Fermi function. Fig. 3.3 shows the Lindhard response as a function of $\mathbf{q}$ in case of a one-, two-, and three-dimensional free electron gas. In the 1D case, the response is dramatically different. Assuming a linear dispersion around E_{F}, $\chi_{\mathrm{L}}(q)$ has a logarithmic divergence at $q = 2k_{\mathrm{F}}$,

$$\chi_{\mathrm{L}}^{\mathrm{1D}}(q) = -e^2\, n(E_{\mathrm{F}})\, \ln \left| \frac{q + 2k_{\mathrm{F}}}{q - 2k_{\mathrm{F}}} \right|, \tag{3.5}$$

where $n(E_{\mathrm{F}})$ is the density of states at the Fermi level. It is remarkable, that in the 1D case, an external perturbation $\phi(q)$ leads to a divergent charge redistribution according to Eqs. 3.3 and 3.5. This implies that the electron gas itself is unstable, even without a finite electron-phonon coupling. However, this divergence is very fragile and there are reasonable doubts, if this is the only relevant mechanism for CDW formation in real materials [12]. This issue will be a central part in the discussion below.

Already in the 2D case, only a step-like feature remains at $\mathbf{Q} = 2\mathbf{k}_{\mathrm{F}}$, but the divergence is absent. The main contributions to the integral in Eq. 3.4 come from pairs of states (one full, one empty) having the same energy, but differ by $2\mathbf{k}_{\mathrm{F}}$ in momentum. It is obvious from Fig. 3.4, that in dimensions higher than one, the

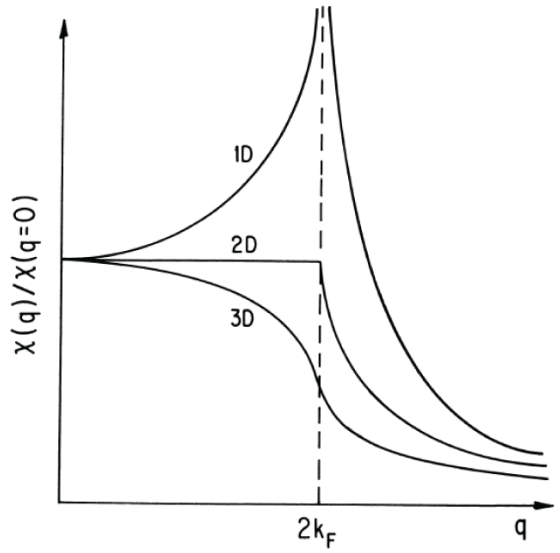

Figure 3.3: The Lindhard response function as a function of momentum transfer $\mathbf{q}$ plotted for a one, two and three dimensional free electron gas at $T = 0$. The divergence due to nesting is most prominent at low dimensionality. From [5].

number of such states is significantly reduced. Thus, the divergence in $\chi_{\mathrm{L}}(\mathbf{q})$ is connected to the topology of the Fermi surface, particularly to the presence of parallel surface sheets that can be mapped onto each other by a single vector $\mathbf{Q}$, referred to as nesting. In a one dimensional electron gas, the Fermi surface only consists of two points for a single chain, or two parallel sheets for an extremely anisotropic metallic array as shown in Fig. 3.4 (a) [5]. A single nesting vector $\mathbf{Q}$ perfectly connects the two sheets. For a 2D Fermi cylinder, Fig. 3.4 (b), this is not possible, but $\mathbf{Q}$ at best connects two lines. Panel (c) shows a quasi one-dimensional Fermi surface, obtained by including a dispersion perpendicular to the 1D chain. In this topology a nesting vector $\mathbf{Q}$ can be found that connects large parts of the Fermi surface. A similar situation will be discussed for the rare-earth tritellurides in Sec. 3.2.2.

To describe the CDW phase transition, electron-phonon coupling and the temperature dependence of the Lindhard susceptibility have to be taken into account. Already above the transition temperature, the CDW formation is preceded by the softening of the particular phonon mode, corresponding to the CDW lattice distortion[2]. With decreasing temperature, the distortion becomes static at $T = T_{\mathrm{CDW}}$, defining the transition temperature. The phonon renormalization $\tilde{\omega}_{\mathbf{q}}$, driven by the electronic

[2]As the CDW phonon is at $\mathbf{Q} = 2\mathbf{k}_{\mathrm{F}}$, it is not observable via Raman scattering.

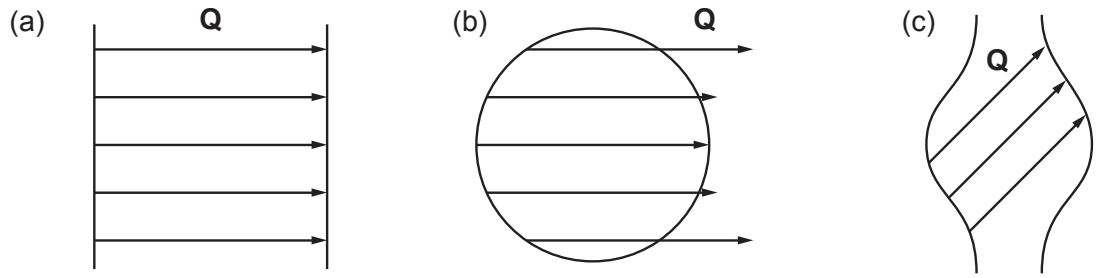

Figure 3.4: Nesting in different Fermi surface topologies. The arrows indicate pairs of states, one full and one empty, connected by a nesting vector **Q**. In (a), the one dimensional case, perfect nesting is realized. This is not possible for (b), a two dimensional Fermi sphere. In (c), the quasi one dimensional case, there are nesting vectors **Q** which connect parts of the Fermi surface. Adapted from [5].

susceptibility $\chi_{\mathrm{L}}(\mathbf{q}, T)$ and the electron-phonon coupling strength g, is known as the Kohn anomaly [107]. In mean field approximation, it reads [5]

$$\tilde{\omega}_{\mathbf{q}}^2 = \omega_{\mathbf{q}}^2 + \frac{2g^2\omega_{\mathbf{q}}}{\hbar}\chi_{\mathrm{L}}(\mathbf{q}, T), \tag{3.6}$$

with $\omega_{\mathbf{q}}$ being the unrenormalized phonon frequency. At T_{CDW}, the lattice distortion "freezes-in" as $\tilde{\omega}_{\mathbf{q}} \to 0$. As the divergence in the electronic response disappears in dimensions higher than one, the renormalization of the phonon frequencies gets less significant. If $\tilde{\omega}_{\mathbf{q}}$ remains finite even at $T = 0$, no phase transition occurs.

Properties of the CDW state can be probed by studying excitations of the charge density condensate. Via light scattering, not only phonons and the excitation of electron hole pairs across the energy gap can be studied, but also collective excitations of the electrons. In general, it is possible to excite the phase or the amplitude of the electron density wave. In the example of the linear chain of atoms, phason and amplitudon are depicted for the limit $q = 0$ in Fig. 3.5. Phase excitations lead to a displacement of the electron density $\rho(r)$ with respect to the lattice resulting in a

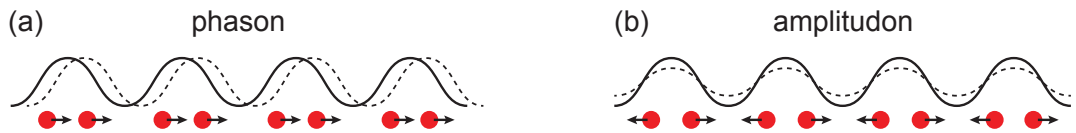

Figure 3.5: Phase (a) and amplitude (b) mode excitation of the CDW (solid line) in a 1D metal in the limit $\mathbf{q} = 0$. In the chain of lattice atoms (red spheres), the displacements in response to the electronic excitation (dashes) are indicated by arrows.

change of the dipole moment. Consequently the phase mode is optically active, i.e. can be probed via infrared spectroscopy. In contrast, the fluctuation of the amplitude of the charge density wave changes the polarizability and thus is Raman active. Via the amplitude mode (AM), the temperature dependence of the CDW condensate density can be studied as will be discussed in Sec. 3.4.3.

3.2 Properties of the rare-earth tritellurides

3.2.1 Composition and structure

Rare-earth tritellurides ($R\mathrm{Te}_3$) are quasi two-dimensional layered systems, consisting of stacked rare-earth-tellurium and tellurium layers that mainly determine the physical properties [109]. The crystal is pseudo-tetragonal and belongs to space group $Cmcm$ (No. 63); all atoms are in Wyckoff 4(c) positions and the unit cell contains four formula units [109]. The orthorhombic distortion of the crystal is small and shrinks from 0.3% in LaTe_3 having $a = 4.405\,\text{Å}$ and $c = 4.42\,\text{Å}$ to 0.05% in DyTe_3 having $a = 4.302\,\text{Å}$ and $c = 4.304\,\text{Å}$ [110]; the respective long axes are $b = 26.267\,\text{Å}$

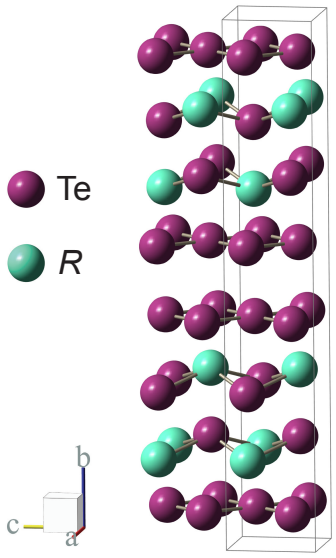

Figure 3.6: Crystal structure of the rare-earth tritellurides ($R\mathrm{Te}_3$). The 3D crystallographic unit cell is indicated in gray. The structure consists of nearly square planar Te double layers separated by two corrugated R-Te layers. The space group symmetry is orthorhombic. Note that b is the long axis here (crystal structure created with *Balls & Sticks* [108]).

and $b = 25.405\,\text{Å}$, respectively [111]. The space group has a glide plane between the tellurium bilayer in the middle of the unit cell. If the upper half of the unit cell is translated by $c/2$, a reflection on the glide plane maps it onto the lower half of the unit cell. This symmetry occurs only in the c but not in the a direction and thus makes the two directions inequivalent and the structure orthorhombic (see Fig. 3.6). The single crystalline samples were grown in the group of Ian Fisher at Stanford University via a self-flux technique and slow cooling of the binary melt as described in Refs. [111–113].

3.2.2 Electronic properties

In the Te layers, the atoms are arranged in a planar, almost quadratic unit cell, indicated by the black square in Fig. 3.7 (a) with x, z being the lattice parameters of the Te cell. These layers mainly determine the electronic properties of the rare-earth tritellurides [109], as only the Te $5p_x$ and $5p_z$ orbitals contribute to the bands that cross the Fermi energy [114]. The Fermi surface as determined by angle-resolved photo-emission (ARPES) measurements is shown in Fig. 3.7 (b) and (c) [115–117]. For describing the electronic properties, it is convenient to use the Te square cell in addition to the crystallographic one. It is rotated by 45° with respect to the crystallographic cell and encloses only half the area. The $5p_x$ and $5p_z$ orbitals of neighbouring Te atoms overlap, forming linear chains perpendicular to each other as depicted in Fig. 3.7 (a). In reciprocal space, the electronic unit cell is spanned by k_x and k_z and encloses twice the area of the Brillouin zone (BZ) of the crystallographic unit cell (red dashed rectangle) that is confined by $a^* = 2\pi/a$ and $c^* = 2\pi/c$. At 100 K, deep in the CDW state, larger parts of the Fermi surface (FS) are gapped out than at 300 K, as the CDW energy gap further opens at surface sheets connected by the nesting vector $\mathbf{Q}_{\text{CDW}} \parallel c^*$ ($T_{\text{CDW}}(\text{TbTe}_3) = 336\,\text{K}$). The gap is anisotropic in momentum space and breaks the 4-fold rotational symmetry (C_4).

The electronic structure can be modeled by a tight-binding scheme [10,114,116,118]. The predicted Fermi surface [black dashed lines in Fig. 3.7 (b) and (c)] consists of p_x and p_z bands (inner dashed lines) which show a high intensity in the ARPES measurement at 300 K and bands that show low intensity (outer dashed lines) and result from back-folding due to the crystallographic BZ boundaries (dashed red lines) [119]. The weak intensity of the folded bands reflects the small 3D couplings and, consequently, the nearly 2D character of these compounds [114]. Band folding due to the

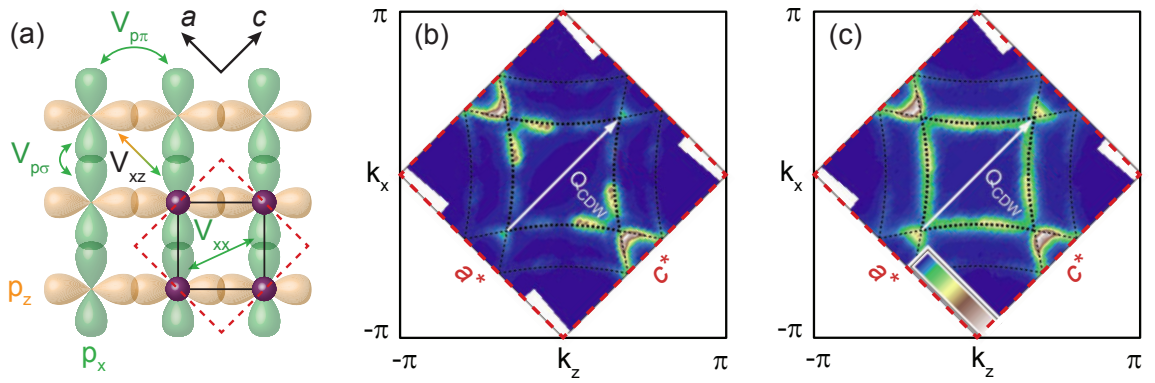

Figure 3.7: Orbital structure of the Te plane and $TbTe_3$ Fermi surface. (a) In a Te plane, the atoms (violet spheres) are connected via Te $5p_x$ (green) and $5p_z$ (orange) orbitals. Various hopping matrix elements are indicated. The bonds define an electronic unit cell (full black square) which is rotated by 45° with respect to the crystallographic unit cell (dashed red). (b, c) Fermi surface of $TbTe_3$ as determined by ARPES measurements [117]. (b) Deep in the CDW phase large parts of the Fermi surface are gapped at the corners connected by the nesting vector $\mathbf{Q}_{\mathrm{CDW}}$. (c) Fermi surface at 300 K where the CDW gap is almost closed [$T_{\mathrm{CDW}}(TbTe_3) = 335\,\mathrm{K}$]. The Brillouin zone of the crystallographic unit cell (dashed red), spanned by a^* and c^*, encloses half the area of the Te unit cell (black), spanned by k_x and k_z, and is rotated by 45°.

periodic lattice distortion in the CDW state will be neglected here, as the resulting shadow bands, observed and discussed in Refs. [114] and [119], are weak. Bilayer splitting effects due to interactions between two adjacent Te layers split the bands [dotted black lines in Fig. 3.7 (b, c)] at the Fermi surface by $0.01 - 0.03\,c^*$ [114]. They are neglected in the tight-binding model, but play a role in behaviour of the CDW amplitude mode discussed in Sec. 3.4.3.

Tight binding model

The tight binding (TB) model used in this thesis, largely follows that described in Refs. [10] and [114]. However, next nearest neighbour interactions are included here, in particular those between the p_x and p_z bands [19]. As already mentioned by Brouet *et al.* [114], this reconciles the experimental FS and the TB fit as the interaction lifts the degeneracy at the band crossing points[3] and creates two independent FS sheets: a small electron pocket around Γ and outer hole-like pieces. First, the full model is described as developed by our collaborators E. A. Nowadnick, A. F. Kemper and T. P. Devereaux [19], then band structure and nesting conditions are briefly discussed.

[3]The behaviour resembles the general concept of anti-crossing in two-level systems [120].

The real space Hamiltonian can be expressed as

$$\begin{aligned} H &= -V_{p\sigma}\sum_{m,n}\left[c^{\dagger}_{m,n+1(p_x)}c_{m,n(p_x)}+c^{\dagger}_{m+1,n(p_z)}c_{m,n(p_z)}\right] \\ &- V_{p\pi}\sum_{m,n}\left[c^{\dagger}_{m+1,n(p_x)}c_{m,n(p_x)}+c^{\dagger}_{m,n+1(p_z)}c_{m,n(p_z)}\right] \\ &- V_{xx}\sum_{m,n,\alpha}\left[c^{\dagger}_{m+1,n+1(\alpha)}c_{m,n(\alpha)}+c^{\dagger}_{m-1,n+1(\alpha)}c_{m,n(\alpha)}\right] \\ &- V_{xz}\sum_{m,n}\left[c^{\dagger}_{m+1,n+1(p_x)}c_{m,n(p_z)}+c^{\dagger}_{m+1,n+1(p_z)}c_{m,n(p_x)}\right] \\ &+ V_{xz}\sum_{m,n}\left[c^{\dagger}_{m-1,n+1(p_x)}c_{m,n(p_z)}+c^{\dagger}_{m-1,n+1(p_x)}c_{m,n(p_z)}\right] \\ &- \mu\sum_{m,n,\alpha}c^{\dagger}_{m,n(\alpha)}c_{m,n(\alpha)} \;+\; h.c. \end{aligned} \tag{3.7}$$

where $c^{\dagger}_{m,n(\alpha)}$ creates an electron at site (m,n) in orbital $\alpha = p_x, p_z$ [19]. It includes both nearest and next-nearest neighbor hopping matrix elements within one tellurium plane, as denoted in Fig. 3.7 (a). Fourier transforming Eq. (3.7) leads to the two bands $\epsilon^{(\nu=\pm)}_{\mathbf{k}}$, where $\nu = +$ and $\nu = -$ label the electron and the hole band, respectively,

$$\epsilon^{\pm}_{\mathbf{k}} = \frac{1}{2}\left[h^{11}_{\mathbf{k}} + h^{22}_{\mathbf{k}} \pm \sqrt{(h^{11}_{\mathbf{k}} - h^{22}_{\mathbf{k}})^2 + 4(h^{12}_{\mathbf{k}})^2}\right]. \tag{3.8}$$

With the Te-Te distance set unity, the energies $h^{ij}_{\mathbf{k}}$ read

$$\begin{aligned} h^{11}_{\mathbf{k}} &= -2V_{p\pi}\cos k_z - 2V_{p\sigma}\cos k_x - 4V_{xx}\cos k_z \cos k_x - \mu, \\ h^{22}_{\mathbf{k}} &= -2V_{p\pi}\cos k_x - 2V_{p\sigma}\cos k_z - 4V_{xx}\cos k_z \cos k_x - \mu, \\ h^{12}_{\mathbf{k}} &= -4V_{xz}\sin k_z \sin k_x. \end{aligned} \tag{3.9}$$

The resulting energy bands are plotted in Fig. 3.8. Using the experimental distances between the rare-earth and the Te ions of 4.34 and $4.34/\sqrt{2}$ Å, respectively, the hopping matrix elements are $V_{p\sigma} = 2.99, V_{p\pi} = -1\,\mathrm{eV}$. Parameters are adjusted to achieve the best match to the ARPES-derived Fermi surfaces from Ref. [119]. If also the next nearest neighbour interactions $V_{xx} = 0.09, V_{xz} = 0.12\,\mathrm{eV}$ are included, the match to experiment is further improved. The chemical potential is set to yield a filling of 1.6 electrons/band. Zero energy separates the occupied from the unoccupied

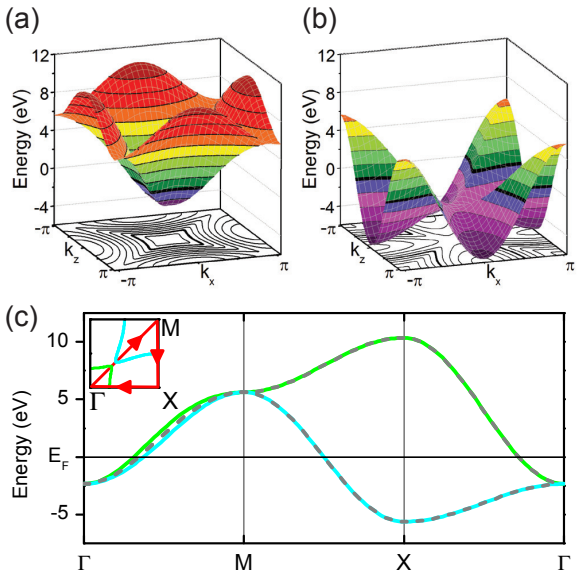

Figure 3.8: Band structure of $ErTe_3$. In a tight binding model, the hopping parameters were adjusted as to match the experimental FS. Panels (a) and (b) separately show the electron and hole band, respectively, using $V_{xx} = 0.09\,\text{eV}$ and a hybridization of $V_{xz} = 0.12\,\text{eV}$. Both the 2D band structure and the constant energy contours are plotted. Panel (c) shows the dispersion along the line $\Gamma - M - X - \Gamma$, as indicated in the inset, before (dashed lines) and after (full lines) the hybridization V_{xz} has been turned on.

states in the figure (black horizontal line). Panel (a) and (b) show the electron and hole band, respectively. Contours of constant energy are projected on the ground plane of the cube defined by the axes. The 2D Fermi surface is distinguished by a thicker line. Panel (c) shows the dispersion along the line $\Gamma - M - X - \Gamma$; the inset illustrates the corresponding path in the BZ.

The two dominant hopping parameters are $V_{p\sigma}$ and $V_{p\pi}$ along and, respectively, perpendicular to the overlapping p_x or p_z orbitals. $V_{p\sigma}$ alone would describe perfect 1D chains perpendicular to each other and result in a FS that consists of two sets of exactly straight lines, exhibiting perfect nesting. The coupling $V_{p\pi}$ between two parallel chains, either p_x or p_z, introduces a deviation from one-dimensionality and a curvature of the FS proportional to $V_{p\pi}/V_{p\sigma}$ [114]. Together, $V_{p\sigma}$ and $V_{p\pi}$ lead to slightly warped Fermi surface lines as depicted in Fig. 3.9 (a), but only V_{xz} couples p_x with p_z orbitals and thus models the interaction between perpendicular chains. Hence, $V_{xz} \neq 0$ corresponds to a hybridization of the energy bands lifting the band degeneracy along the $\Gamma - M$ Brillouin zone cut. Due to their interaction, the p_x and p_z

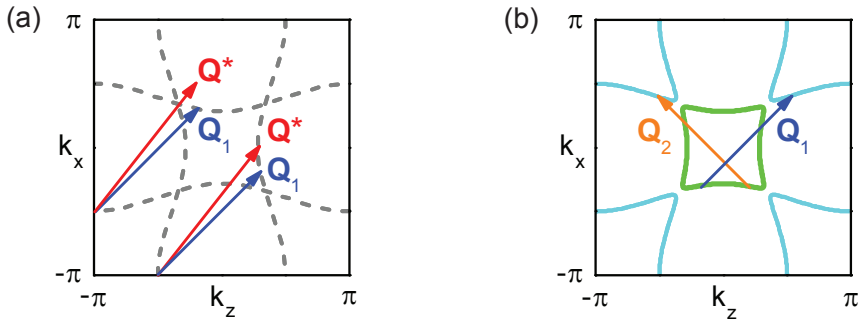

Figure 3.9: Fermi surface and nesting vectors derived from a tight binding model. The hopping matrix elements are optimized for $ErTe_3$. (a) Bands for $V_{p\sigma} = 2.99$, $V_{p\pi} = -1$ and $V_{xx} = 0.09\,\text{eV}$. The p_x and p_z bands cross, if there is no interaction between them, i.e. $V_{xz} = 0$. There are two energetically possible orientations for CDW ordering, $\mathbf{Q}_1$ and $\mathbf{Q}^\star$, where $\mathbf{Q}^\star$ is the wave vector predicted by nesting. (b) Theoretical Fermi surface for $V_{xz} = 0.12\,\text{eV}$ best reproducing the experimental findings [114]. Also shown are the two experimentally observed orthogonal ordering vectors $\mathbf{Q}_1$ and $\mathbf{Q}_2$ parallel to the crystallographic c and a axes, respectively, corresponding to the CDW transitions at T_{CDW1} and T_{CDW2}. Due to the small orthorhombicity of the crystal the first CDW $\mathbf{Q}_1$ always aligns along the c direction.

bands do not cross any further, but form sharp corners close to the lifted degeneracy points. This is shown in Fig. 3.8 and Fig. 3.9 (b).

Of course FS warping also affects the the nesting conditions. There is a competition between $\mathbf{Q}^\star$ which perfectly nests one of the FS chains (p_x in Fig. 3.9) but does not fit to the perpendicular one (p_z), and $\mathbf{Q}_1$ which nests both bands moderately good but none perfect. The competition between these different wave vectors has been studied by Yao *et al.* [10]. Via a calculation of the Lindhard function (c.f. Sec. 3.1) they find, that $\mathbf{Q}^\star$ is favoured, if the transition temperature T_{CDW} is lower than approximately 300 K and the dimensionless $\mathbf{q}$-independent electron-phonon coupling strength λ is between 0.093 and 0.103, while $\mathbf{Q}_1$ is favoured for higher transition temperatures and coupling constants (note the different nomenclature in Ref. [10]). The latter case is observed in the tritellurides.

In contrast, Johannes and Mazin [12] find that in metals electronic instabilities driven by nesting alone are so fragile that the correct nesting vector cannot be predicted in real systems. The Lindhard susceptibility has peaks of comparable size at the nesting vector $\mathbf{Q}^\star$ predicted from the band structure and at the CDW ordering vector $\mathbf{Q}_1$ determined experimentally in $R\text{Te}_3$ [110]. Thus, nesting alone is unlikely to determine the CDW ordering. Rather a concerted action of electronic and ionic

subsystems, i.e. a **q**-dependent electron-phonon coupling plays an indispensable role in density wave formation and the selection of the ordering vector in real systems [12]. This will be one of the major points in the results presented below.

3.2.3 The rare-earth series

Single crystals of $R\mathrm{Te}_3$ exist for almost all rare earth elements [111], because of their remarkably similar chemical properties [121]. Nevertheless, the magnetic state has a substantial influence on the spectroscopic properties such as crystal field excitations and on the possible formation of superconductivity if the CDW is suppressed [122, 123].

The common ionization state of the rare-earth atom is R^{3+} which leaves the $4f$ shell the only partially filled one, while all other shells are completely filled or empty. The $4f$-electrons are strongly localized and have a higher probability to be close to the nucleus compared to the $5s^2$ and $5p^6$ shells [124]. Hence, they can be considered local magnetic moments that depend on the $4f$-filling. The moments range from zero in non-magnetic La^{3+} to a maximum effective magnetic moment $\mu_{\mathrm{eff}} = g_{\mathrm{L}}\sqrt{J(J+1)}\,\mu_{\mathrm{B}} = 10.65\,\mu_{\mathrm{B}}$ per ion in Dy^{3+} [125]. Here, μ_{B} is the Bohr magneton, J the total angular momentum and g_J the Landé g-factor

$$g_J = \frac{3}{2} + \frac{S(S+1) - L(L+1)}{2J(J+1)}. \tag{3.10}$$

The values of the total quantum numbers S (spin), $L = \sum m_l$ (total orbital angular momentum) and J (total angular momentum) are determined via Hund's rules and L-S (Russell-Saunders) coupling. In Table 3.1 they are listed for all rare-earth elements. Also listed are the theoretical effective magnetic moments $p = \mu_{\mathrm{eff}}/\mu_{\mathrm{B}} = g_J[J(J+1)]^{1/2}$ and the de Gennes factors $(g_J - 1)^2 J(J+1)$. Of course the magnetic properties influence the phase diagram of rare-earth compounds. In case of the rare-earth tritellurides, this will be covered in the following section.

Another property of the rare-earths is referred to as lanthanide contraction. As the nuclear charge increases for heavier R elements, the electrons feel a stronger Coulomb attraction. Mainly the $4f$-electrons are affected as they are well embedded within the atom and shielded by the $5s$ and $5p$ states from the outside world. The incomplete screening of the increasing nuclear charge along the rare earth series causes a decrease in the ionic and atomic radii [121]. Consequently the lattice parameters of the $R\mathrm{Te}_3$

ion	shell	S	L	J	g_J	p	de Gennes factor
La^{3+}	$4f^0$	0	0	0	–	0	–
Ce^{3+}	$4f^1$	$\frac{1}{2}$	3	$\frac{5}{2}$	$\frac{6}{7}$	2.54	0.18
Pr^{3+}	$4f^2$	1	5	4	$\frac{4}{5}$	3.58	0.80
Nd^{3+}	$4f^3$	$\frac{3}{2}$	6	$\frac{9}{2}$	$\frac{72}{99}$	3.62	1.84
Pm^{3+}	$4f^4$	2	6	4	$\frac{3}{5}$	2.68	3.20
Sm^{3+}	$4f^5$	$\frac{5}{2}$	5	$\frac{5}{2}$	$\frac{2}{7}$	0.85	4.46
Eu^{3+}	$4f^6$	3	3	0	–	0.0	–
Gd^{3+}	$4f^7$	$\frac{7}{2}$	0	$\frac{7}{2}$	2	7.94	15.75
Tb^{3+}	$4f^8$	3	3	6	$\frac{3}{2}$	9.72	10.50
Dy^{3+}	$4f^9$	$\frac{5}{2}$	5	$\frac{15}{2}$	$\frac{4}{3}$	10.63	7.08
Ho^{3+}	$4f^{10}$	2	6	8	$\frac{5}{4}$	10.60	4.50
Er^{3+}	$4f^{11}$	$\frac{3}{2}$	6	$\frac{15}{2}$	$\frac{6}{5}$	9.59	2.55
Tm^{3+}	$4f^{12}$	1	5	6	$\frac{7}{6}$	7.57	1.17
Yb^{3+}	$4f^{13}$	$\frac{1}{2}$	3	$\frac{7}{2}$	$\frac{8}{7}$	4.53	0.32
Lu^{3+}	$4f^{14}$	0	0	0	–	0	–

Table 3.1: Magnetic ground states for $4f$ ions (rare-earths). For each ion, the shell configuration and the the ground state values of S, L and J predicted by Hund's rules are listed. Also shown is the effective magnetic moment $p = \mu_{\text{eff}}/\mu_{\text{B}} = g_J[J(J+1)]^{1/2}$ and the de Gennes factor $(g_J - 1)^2 J(J+1)$ calculated from the Hund's rule predictions. From [125].

crystals decrease as mentioned already in Sec. 3.2.1. As there is a similarity with applied pressure, the rare-earth substitution is referred to as chemical pressure in literature [110, 118].

3.2.4 Phase diagram

The properties of the rare-earth tritellurides are represented and summarized by the phase diagram shown in Fig. 3.10. The main features are two CDW states having perpendicular ordering vectors $\mathbf{Q}_1$ and $\mathbf{Q}_2$ oriented along the the c and a direction of the crystal, respectively. The first study on the effects of chemical pressure in

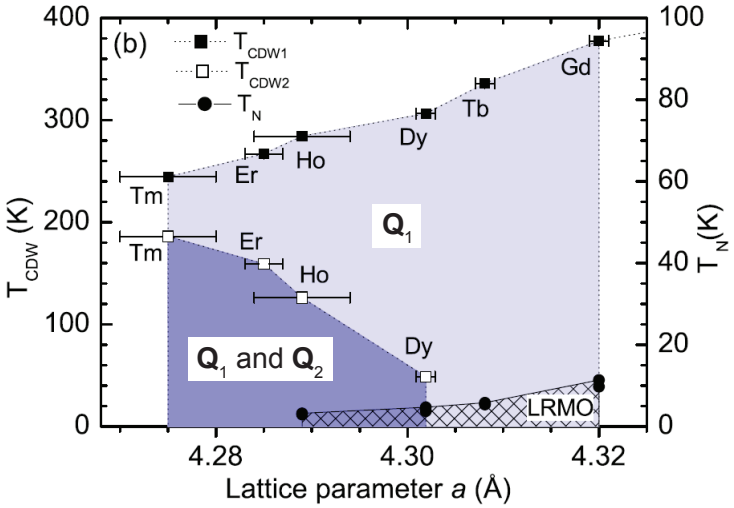

Figure 3.10: $R\mathrm{Te}_3$ phase diagram. Plotted are the transition temperatures as a function of the lattice parameter a for the heavy rare-earth members of the series. The phases of the first CDW, with ordering vector $\mathbf{Q}_1$ and the second CDW, ordered along $\mathbf{Q}_2$, are coloured in light and dark blue respectively. There is also a regime where the CDW coexists with long-range magnetic order (LRMO, hatched). From [126].

$R\mathrm{Te}_3$ was reported by DiMasi *et al.* [118]. The phase diagram is adapted from Ru *et al.* [110, 111].

Depicted is the ordering temperature as a function of the lattice parameter a so as to highlight the equivalence of chemical substitution and pressure. The first and second CDW phase is visualized by light blue and dark blue shaded areas, respectively. With decreasing atomic number and thus increasing radius of the R atom, the lattice parameters get larger (cf. Sec 3.2.3). This goes along with a monotonic increase of the CDW transition temperature T_{CDW1} from 244 K in TmTe_3 to 377 K in GdTe_3 [110, 111]. An extrapolation of the T_{CDW1} curve to the lattice parameters of the lighter $R\mathrm{Te}_3$ compounds (R = La, Ce, Pr, Nd) yields transition temperatures in excess of 450 K [111].

The increase of T_{CDW1} with decreasing (chemical) pressure results from subtle changes on the Fermi surface which improve the nesting conditions and enhance the density of states $N(E_{\mathrm{F}})$, while minimal changes in the topology of the Fermi surface are expected [114]. When the lattice expands, both $V_{p\pi}$ and $V_{p\sigma}$ decrease, but the curvature of the FS is only mildly affected as it depends on the ratio of the hopping parameters $V_{p\pi}/V_{p\sigma}$ as mentioned in Sec. 3.2.2. The bandwidth, however, is directly proportional to $V_{p\sigma}$ [114]. An expansion of the lattice decreases the band-

$R\mathrm{Te}_3$	YTe_3	SmTe_3	GdTe_3	TbTe_3	DyTe_3	HoTe_3	ErTe_3	TmTe_3
T_{CDW1}	334(3)	416(3)	377(3)	336(3)	306(3)	284(4)	267(3)	244(3)
T_{CDW2}	–	–	–	–	49(5)	126(6)	159(5)	186(5)

Table 3.2: CDW transition temperatures T_{CDW1} and T_{CDW2}. Based on the trend in T_{CDW1}, the transition temperatures for the compounds of $R = \mathrm{La}, \mathrm{Ce}, \mathrm{Pr}, \mathrm{Nd}$ are anticipated to be greater than 450 K. From [111].

width and, as a result, $N(E_{\mathrm{F}})$ increases almost linearly [110]. The variation in the density of states likely plays the dominant role as the mean-field transition temperature depends exponentially on $N(E_{\mathrm{F}})$ [5]. Further details can be found in Refs. [110] and [111].

The second transition to a bidirectional CDW phase only occurs for Dy and heavier members of the rare-earth series [110]. This may be due to the larger energy gap associated with the higher transition temperatures in the lighter $R\mathrm{Te}_3$ compounds. As a result, only small parts of the FS remain intact below T_{CDW1}, as seen by ARPES measurements [114]. Moving to heavier $R\mathrm{Te}_3$, progressively more of the FS becomes available for the second CDW transition at lower temperatures explaining the opposite trends of T_{CDW1} and T_{CDW2} in the phase diagram [110].

The transition temperatures T_{CDW1} and T_{CDW2} as obtained from resistivity measurements [110,113] are compiled for various $R\mathrm{Te}_3$ compounds in Table 3.2. The phase transitions were corroborated by specific heat and x-ray diffraction experiments [110] that also returned the lattice parameters and the CDW ordering vectors $\mathbf{Q}_1$ and $\mathbf{Q}_2$. CDW order was also observed in real space via STM measurements [127].

In some compounds, the CDW coexists with long range antiferromagnetic order (LRMO) at the lowest temperatures [126], as first reported by Iyeiri *et al.* [128]. From HoTe_3 to GdTe_3 the Néel temperature increases as does the de Gennes factor (cf. Table 3.1). Deviations from the expected linear behaviour [125] can be attributed to the effects of crystal electric fields on the Hund's rule multiplet [126]. In CeTe_3 even more complicated types of magnetic order like helimagnetism or an incommensurate magnetic order are conjectured to occur [128]. The interplay between magnetic order and the CDW is another subject of research in this material class [126]. It was reported, that at high pressure also superconductivity joins the competition for the FS in TbTe_3 [122]. This issue will be picked up in Sec. 3.4.2.

3.3 Results

Across the rare-earth tritelluride family, $LaTe_3$, $DyTe_3$, $HoTe_3$ and $ErTe_3$ samples were available covering most of the range of rare earths and, in particular, of the range of transition temperatures. At low energies, we studied phonons and amplitude modes (AM) of the CDW condensate as a function of temperature. High pressure experiments were performed in $LaTe_3$ and, particularly, in $ErTe_3$ to compare the effect of chemical and applied pressure and to obtain the pressure-temperature phase diagram. At high energies, signatures of the CDW energy gap were detected in $LaTe_3$, $DyTe_3$ and $ErTe_3$ and the gap anisotropies were studied.

3.3.1 Amplitude modes and low energy excitations

In this section the Raman scattering results on $LaTe_3$ at an applied pressure of 6 GPa, and on $DyTe_3$, $HoTe_3$ and $ErTe_3$ at ambient pressure are presented. The pressure was generated by means of the diamond anvil cell described in Sec. 2.3.1. At 6 GPa the lattice constants of $LaTe_3$ are similar to $DyTe_3$ and comparable to those of $HoTe_3$ and $ErTe_3$ [89,129,130]. The temperature dependences of electronic and lattice excitations were studied in all these compounds in the range $8 < T < 290\,\mathrm{K}$ with a spectral resolution of about $3\,\mathrm{cm}^{-1}$. In Fig. 3.11, the Raman response $R\chi''(\omega, T)$ is plotted as a function of the frequency shift ω. For clarity spectra at higher temperatures are offset. All four compounds show a qualitatively similar behaviour: The response at high temperatures, above the CDW transition, is flat and almost featureless as expected for a metal with an almost constant resistivity [110]. With decreasing temperature, several new modes appear in the CDW phase. This is due to the reduced crystal symmetry in the CDW state (band folding). As the CDW is incommensurate [118], also inversion symmetry is lifted which further increases the number of Raman active excitations as the strict mutual exclusion between Raman and infrared active phonons vanishes [131].

In the following, the attention is directed to the modes labeled A, B and C. Just below T_{CDW1}, the intensity at low frequency increases until a new mode A can be resolved. This peak further gains intensity and moves to higher energy. Due to the characteristic onset temperature, it is identified as the amplitude mode (defined in Sec. 3.1) associated with the first CDW transition. In addition, a second new peak (B) appears just below the phonon (C) of the high temperature phase. Phonon C

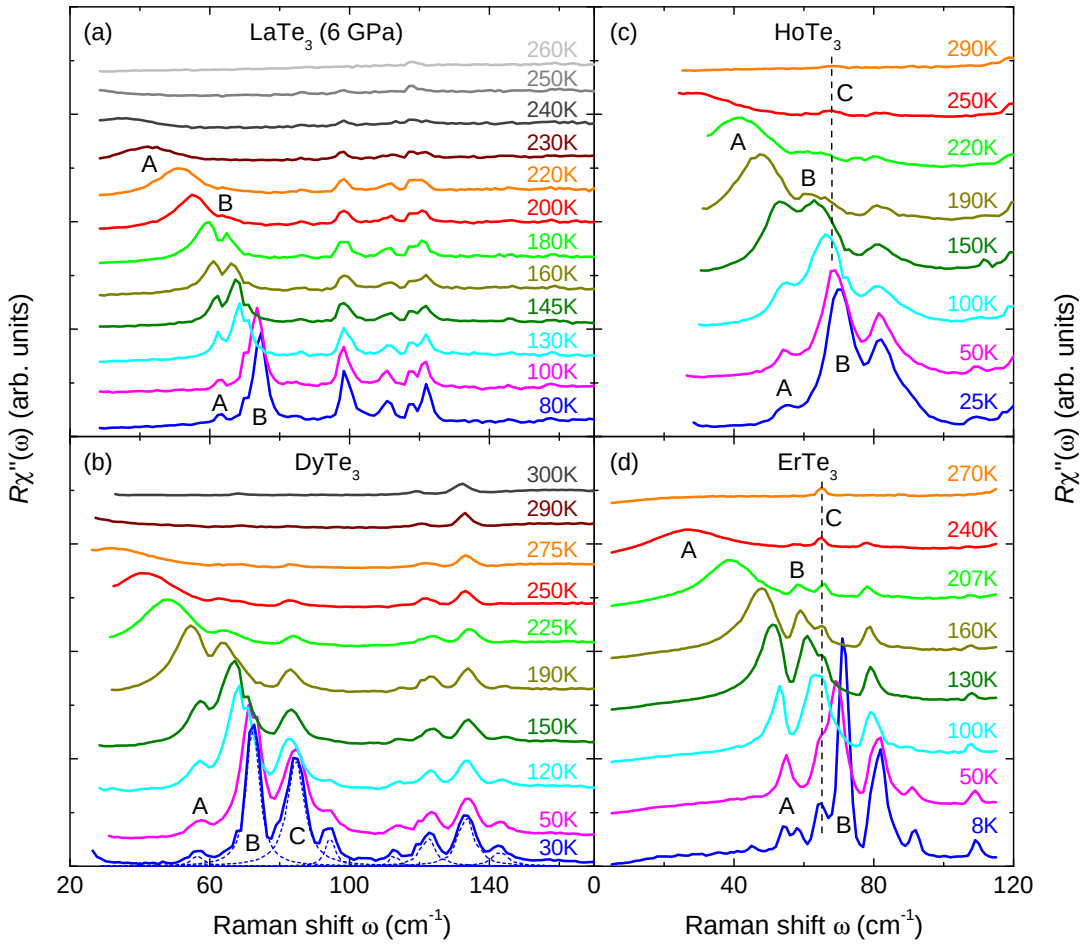

Figure 3.11: Temperature dependence of the low-energy Raman spectra of (a) $LaTe_3$ at 6 GPa and (b) $DyTe_3$, (c) $HoTe_3$ and (d) $ErTe_3$ at ambient pressure in $c'c'$ polarization. The spectra have been shifted for clarity. In all compounds a similar temperature dependence of the modes is observed. The AM appears below T_{CDW} at low energies, then sharpens and moves to higher energies with further cooling. In its course, the AM interacts with some of the phonons, nearby in energy. For the analysis, the peaks were fitted by single oscillators as indicated by dashed lines in panel (b). The modes labeled A, B and C were studied in detail.

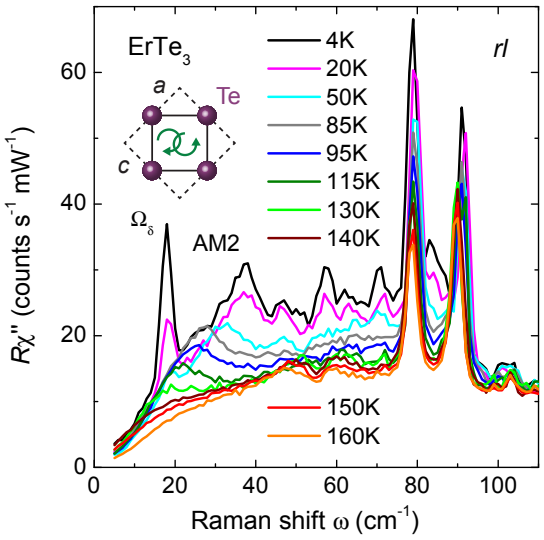

Figure 3.12: Temperature dependence of the second amplitude mode (AM2) in $ErTe_3$. In *rl* polarization (sketched in the inset) only excitations having B_{1g} or B_{2g} symmetry are projected out. A beat mode Ω_δ of AM1 and AM2 appears at $18\,cm^{-1}$. The other peaks are attributed to phonons or originate from crystal electric field level splitting.

stays at the same frequency throughout the whole temperature range, while peak B hardens and also gains intensity until A and B equally share the spectral weight. Upon cooling down further, the spectral weight is more and more transferred from peak A to B. Obviously, the two modes never appear in the same position suggesting that they repel each other (anti-crossing) as noted already by Yusupov *et al.* [21]. The Raman experiment is sensitive enough for resolving an additional change in the CDW ordering at $T \approx 2T_{CDW1}/3$ as will be discussed in detail in Sec. 3.4.3.

Figure 3.12 further scrutinizes the low energy part using additional polarization combinations. With crossed circular polarizations (*rl*) the measurement is equally sensitive to excitations in B_{1g} and B_{2g} symmetry [57], while A_{1g} symmetry, and with it the intense modes A and B, is suppressed by more than one order of magnitude. Only remnants of peak A and B can be seen close to 50 and $60\,cm^{-1}$, e.g. in the 160 K spectrum. Note, that the two modes at 80 and $90\,cm^{-1}$ do not correspond to the two strongest peaks at the lowest temperatures in Fig. 3.11. On cooling down below T_{CDW2} = 155 K, the spectral weight increases at low energies, and an additional peak appears, sharpens and moves to higher energies, until it reaches $37\,cm^{-1}$. This excitation is attributed to the AM of the second CDW transition as it appears just below T_{CDW2} and has the same characteristic temperature dependence as AM1 [19, 132, 133]. At

the lowest temperatures, a resolution-limited peak Ω_δ appears at $18\,\mathrm{cm}^{-1}$ which is exactly half the difference of the two AM frequencies. Hence, Ω_δ is attributed to the beat mode [19]. The peaks between 40 and $90\,\mathrm{cm}^{-1}$ may originate either from crystal electric field (CEF) splitting of the ${}^4I_{15/2}$ ground state multiplet of the rare-earth f-electrons (cf. Sec. 3.4.1) or are due to the lowered symmetry in the crystal distorted by the second CDW [110].

3.3.2 Electronic response in the charge density wave phase

At larger energy transfers, electronic excitations across the CDW energy gap can be observed. Fig. 3.13 shows Raman measurements of $LaTe_3$, $DyTe_3$ and $ErTe_3$ which cover energy shifts up to $8000\,\mathrm{cm}^{-1}$ ($\approx 1\,\mathrm{eV}$) with a resolution of $20\,\mathrm{cm}^{-1}$. Due to the lower resolution, the low energy excitations discussed in the previous section are not resolved any further, but appear as a large peak below $500\,\mathrm{cm}^{-1}$.

In $DyTe_3$ [Fig. 3.13 (b)], an additional sharp peak appears at $3490\,\mathrm{cm}^{-1}$ at low temperatures. It is not connected to the CDW order, but can be attributed to electronic transitions between rare-earth f-electron levels which will be discussed in Sec. 3.4.1.

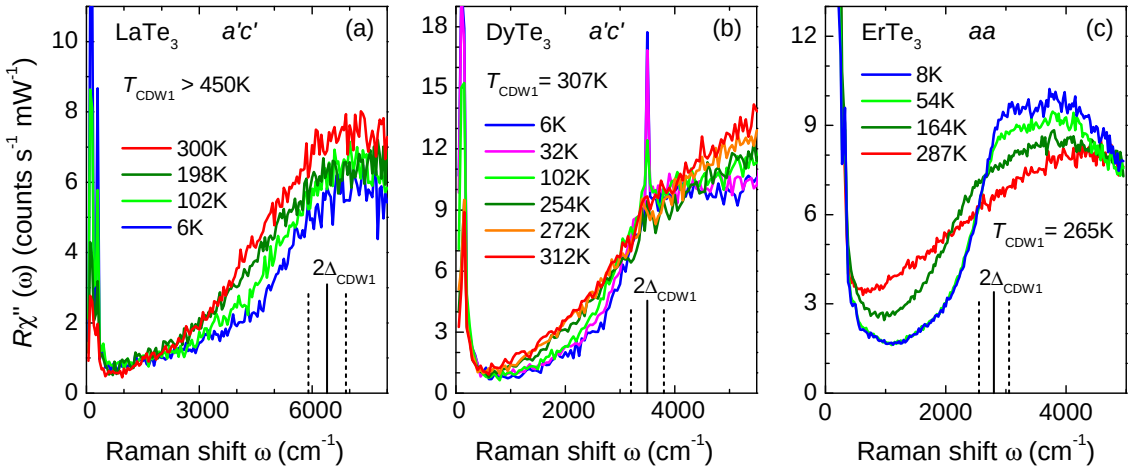

Figure 3.13: CDW energy gaps. A suppression of spectral weight below the gap energy is detected in (a) $LaTe_3$, (b) $DyTe_3$ and (c) $ErTe_3$. The gap edge $2\Delta_{\mathrm{CDW1}}$ (vertical line) is identified as the energy where the spectra change slope; the error is indicated by dashed vertical lines. In $LaTe_3$ with $T_{\mathrm{CDW1}} > 450\,\mathrm{K}$, the sample never reaches the metallic state. Thus the change in slope is present up to the highest temperatures measured. The signatures of the gap are most pronounced in $ErTe_3$, as aa polarization is more sensitive in the gapped areas of the Brillouin zone than $a'c'$. The CEF peak close to the gap edge in $DyTe_3$ [panel (b)] will be discussed in Sec. 3.4.1.

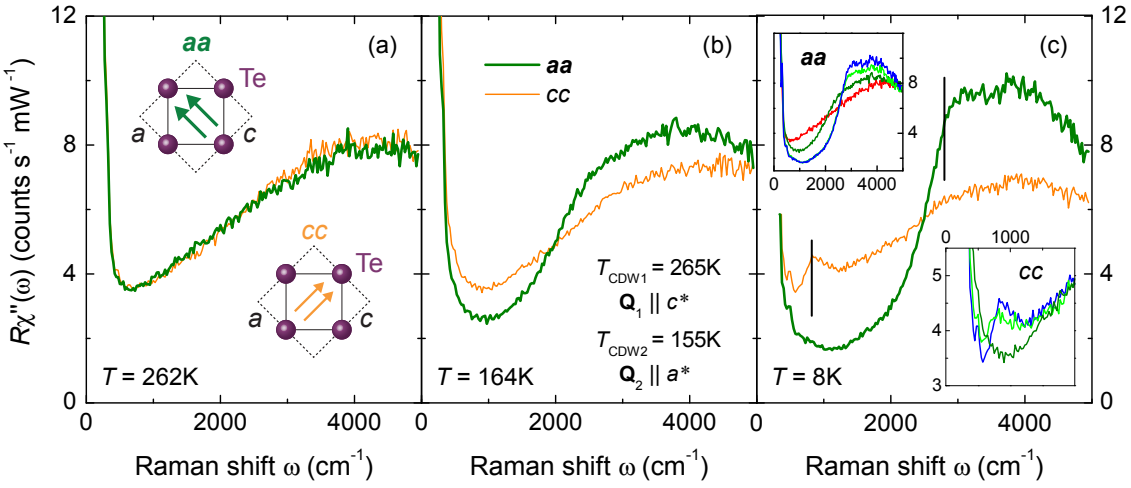

Figure 3.14: Polarization and temperature dependence of the high energy Raman spectra in $ErTe_3$. (a) At 262 K there is no difference in the electronic excitations at high energy for both polarizations. The insets sketch the incoming and scattered photon polarizations with respect to the Te planes. (b) At 164 K the anisotropy between the two polarizations is already well resolved. (c) In the limit $T \to 0$ the electronic gaps with edges at 820 and 2800 cm^{-1} (vertical lines) for both CDWs are fully developed. The upper left and lower right insets show the temperature dependences of both CDW gaps, using the same colour-code as Fig. 3.13 (c). Note that the signatures of the CDW transition at T_{CDW1} with $\mathbf{Q}_1 \parallel c^*$ are observed with incoming and scattered light polarizations parallel to the direction of a. The opposite is true for the transition at T_{CDW2}.

The main feature in Fig. 3.13 is the CDW energy gap. In $LaTe_3$ (a) the sample is deep in the CDW state up to the highest measured temperatures as $T_{CDW1}(LaTe_3) > 450$ K [111]. However, with decreasing temperature, the spectral weight decreases mainly between 2000 and about 6400 cm^{-1}. As the gap edge we identify the energy where the Raman continuum changes from a finite slope to constant. At the lowest temperatures the gap reaches its maximum value $2\Delta_{CDW1} = 6400 \pm 500\,cm^{-1}$ (vertical line). The errors are indicated by dashed vertical lines. The signature of the gap is not very pronounced in the Raman spectra of $LaTe_3$, but it is well resolved in the spectra of $DyTe_3$ [Fig. 3.13 (b)] and $ErTe_3$ [Fig. 3.13 (c)]. In the metallic state, above the transition temperature of $T_{CDW1} = 307$ K, the scattering intensity rises almost linearly for energies ranging from 1000 up to 5500 cm^{-1}. Below T_{CDW1}, there is a suppression of spectral weight inside the gap and a change of the slope of the electronic continuum at the gap edge. Both features become more pronounced at lower temperature. Again, the gap edge is identified as the energy where the spectra

change slope at $2\Delta_{\mathrm{CDW1}} = 3500 \pm 300\,\mathrm{cm}^{-1}$.

It turns out that the $a'c'$ polarization is not the best one for detecting the CDW gap, as will be discussed in Sec. 3.4.6. Rather, the *aa* and *cc* polarizations are most sensitive for observing the gap associated with the first ($\mathbf{Q}_1 \parallel c$) and second ($\mathbf{Q}_2 \parallel a$) CDW, respectively. The polarization selectivity is pointed out in Fig. 3.14. The electronic Raman response of $ErTe_3$ at 262 K, just below T_{CDW1}, is still isotropic. The spectra rise almost linearly between 800 and 3500 cm^{-1} and finally become flat in both *aa* and *cc* polarization. Upon lowering the temperature there is a transfer of spectral weight in the *aa* spectrum from low to high energies [Fig. 3.14 (b) and (c)], and an anisotropy develops. At the lowest temperatures, there is a relatively weak new structure in the *cc* spectrum in the range 500-1200 cm^{-1} which is attributed to the second CDW gap. The insets in panel (c) highlight the temperature dependences [same colour code as in Fig. 3.13 (c)] of the *aa* and *cc* polarized spectra right above and below T_{CDW1} and T_{CDW2}, respectively. In either case, spectral weight is progressively suppressed below the gap edges and piles up above. The full anisotropy without any leakage between the two orthogonal *aa* and *cc* directions, indicates that the crystal is single domain in the probed spot[4]. The maximum gap energies of the first and the second CDW are $2\Delta_{\mathrm{CDW1}} = 2800 \pm 250\mathrm{cm}^{-1}$ and $2\Delta_{\mathrm{CDW2}} = 820 \pm 100\mathrm{cm}^{-1}$, respectively.

3.4 Discussion

First, the results on crystal field excitations are analyzed. Subsequently, the amplitude modes (AMs) of the CDW condensate are used as a probe for the phase transition in high pressure experiments. Below the phase transition, the AMs show a characteristic temperature dependence resembling that of the BCS order parameter in superconductors, but challenging textbook CDW theory. Above the CDW transition, there is evidence for charge fluctuations. Further, the gap magnitude and anisotropy as detected in the electronic Raman response is discussed. Finally, the momentum dependence of the Raman vertex allows the study of the **k**-dependence of the electron-phonon interaction resulting in a proposal for an alternative route to charge density wave formation. Parts of the work have been published in Refs. [19, 132–135].

[4]Single domain areas were already observed in an earlier ARPES experiment on an $ErTe_3$ sample of the same source [119].

3.4.1 Electronic transitions in the 4f shell

In $DyTe_3$ and $CeTe_3$ pronounced peaks were detected at $3490\,cm^{-1}$ [cf. Fig. 3.13 (b)] and around $2300\,cm^{-1}$ (cf. Fig. 3.15). As these frequencies are well above the Debye frequency of about $125\,cm^{-1}$ [111]; a phononic origin of the peaks can be excluded. Additionally, it turns out that some of the modes appear in A_{2g} symmetry (cf. Figs. 3.15 and 3.16) which is forbidden for vibrational Raman scattering in the non-resonant case [136]. However, the frequencies of the modes are compatible with the level splitting of the rare-earth f-electron orbitals due to spin orbit (SO) coupling and crystal electric fields (CEFs) [137]. As to the symmetry, Mortensen *et al.* showed theoretically that an antisymmetric response (here A_{2g}) can be present and even dominate the electronic response for trivalent rare-earth ions in crystals [138]. In the following, the electronic configuration and possible splitting effects in Ce^{3+} and Dy^{3+} are discussed and compared with the observations[5] in $CeTe_3$ and $DyTe_3$.

The electronic configuration of Ce^{3+} is $[Xe]\,4f^1$ which corresponds to the total quantum numbers $S = 1/2$, $L = 3$ and $J = 5/2$ according to Hund's rules (cf. Table 3.1 in Sec. 3.2.3). The electronic states are typically labeled by spectroscopic terms of the form ${}^{2S+1}L_J$ where $L = 0, 1, 2, 3, ...$ is encoded as $S, P, D, F, ...$. In the case of Ce^{3+} this yields ${}^2F_{5/2}$ for the ground state. The first excited state ${}^2F_{7/2}$ is split off due to spin-orbit coupling and has an energy of $2253\,cm^{-1}$ [139]. Close to this energy, a multiplet of four peaks (marked by arrows in Fig. 3.15) is observed in the Raman spectra of $CeTe_3$. The $(2J+1) = 8$ fold degeneracy of the ${}^2F_{7/2}$ level is lifted by CEF effects [137]. However, a minimum degeneracy of two remains, as an electric field cannot break time reversal symmetry, i.e. the spin degeneracy[6]. This is referred to as the Kramers theorem [140]. Consequently, a maximum of four different energy levels can result from CEF splitting in Ce^{3+}, in agreement with the Raman results. Fig. 3.15 (a) demonstrates the consistency of the measurements (cf. Sec. 2.1.2), and panel (b) shows the symmetry analysis. As every atom in the RTe_3 crystal is in the same pseudo-tetragonal local environment (cf. Sec. 3.2.1), the symmetry analysis is based on the D_{4h} point group as described in Ref. [57]. Only the peak at $2110\,cm^{-1}$ appears in pure A_{1g} symmetry, while the other peaks at 2185, 2335, and $2400\,cm^{-1}$ are present in more than one channel. All four peaks are in an energy range of some $100\,cm^{-1}$ showing that the crystal fields of neighbouring atoms lead to a much

[5] In $LaTe_3$ and $ErTe_3$ all f-electron transitions are outside of the measured energy range [139].
[6] In a magnetic field, the degeneracy could be lifted completely.

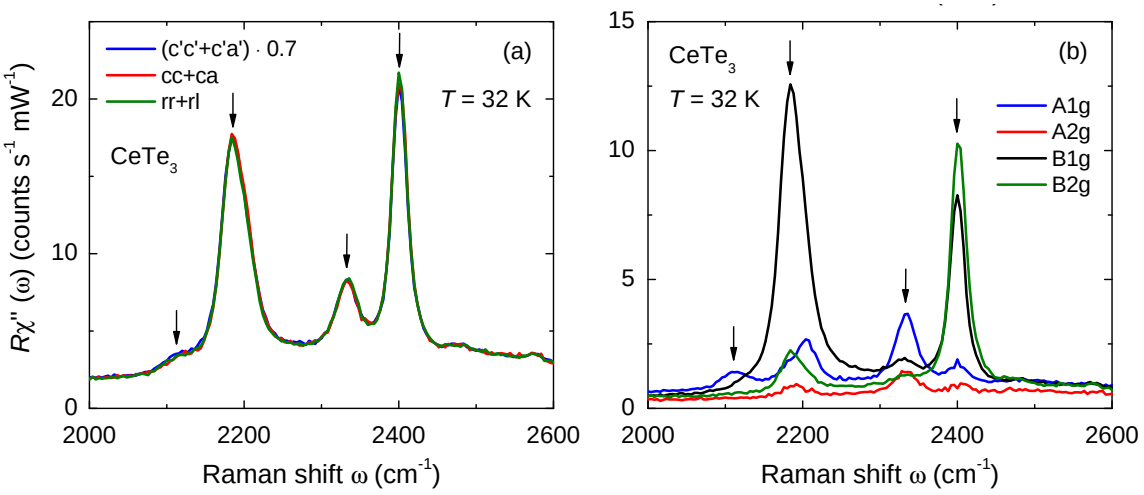

Figure 3.15: Crystal field splitting in $CeTe_3$. (a) Consistency check of the polarization analysis. (b) Due to crystal electric fields, the $^2F_{7/2}$ state of $CeTe_3$ ($4f$ orbitals) splits in energy. Four main peaks are observed at 2110, 2185, 2335, and 2400 cm^{-1} (marked by arrows). Possible origins of the smaller splittings observed around 2185 cm^{-1} are discussed in the text.

smaller energy splitting than spin-orbit coupling (2253 cm^{-1}), because the $4f$ orbitals (radius $\sim$0.3 Å) are efficiently shielded by the $5s$ and $5p$ orbitals (radius $\sim$1 Å) [141].

In $DyTe_3$ the transition from the $^6H_{15/2}$ ground state to $^6H_{13/2}$ requires an energy of 3460 cm^{-1} [139]. Again, these states of different total angular momentum are split due to spin-orbit coupling. The excited state is 14-fold degenerate ($2J+1$). Again, the Kramers degeneracy cannot be lifted by the crystal electric field, and not more than 7 different energy levels can appear. Experimentally, a peak is observed at 3490 cm^{-1} in the $DyTe_3$ crystal[7]. Fig. 3.16 (a) shows that the measurements are consistent. The symmetry analysis in panel (b) reveals that the peak consists of a B_{1g} and an A_{2g} contribution at 3490 and 3495 cm^{-1}, respectively. Indeed, a double peak is observed in $c'a'$ polarization which probes both A_{2g} and B_{1g} symmetry [panel (c)]. However, the energy difference of about 5 cm^{-1} seems to be too small to be explained in terms of crystal electric field splitting which is typically on the order of 100 cm^{-1} in rare-earth atoms [137, 142, 143] (cf. Fig. 3.15). However, the double peak can be explained in terms of Davydov splitting [144, 145], meaning that an exchange interaction between the weakly bound upper and lower part of the RTe_3 unit cell leads to a two-fold level splitting.

[7]It is mere coincidence that the peak is close to the CDW gap edge in $DyTe_3$. In $CeTe_3$ all observed f-electron transitions are well below the gap energy.

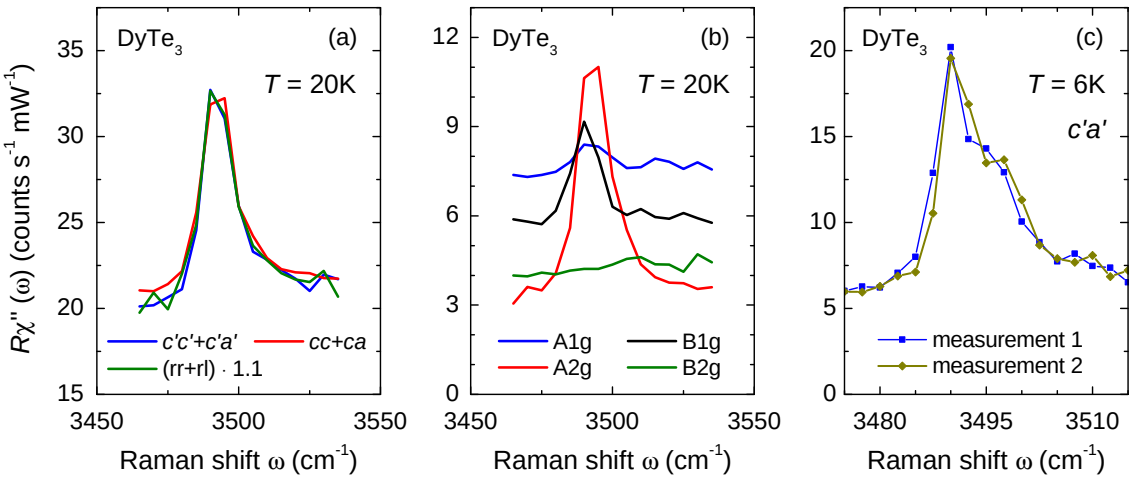

Figure 3.16: Crystal field splitting in $DyTe_3$. (a) Consistency check of the polarization analysis. (b) The excitation into the ${}^6H_{13/2}$ level consists of a B_{1g} and an A_{1g} contribution at $3490\,\mathrm{cm}^{-1}$ and $3495\,\mathrm{cm}^{-1}$, respectively. (c) At $T = 6\,\mathrm{K}$, two independent measurements in $c'a'$ polarization, probing B_{1g} and A_{2g} symmetry, were recorded to confirm the small splitting; indeed, a double peak structure is observed.

Still, it remains puzzling that the number of observable energy levels in $DyTe_3$ is smaller than in the iso-structural $CeTe_3$, despite the higher degeneracy. Either the lower scattering intensity in $DyTe_3$ prevents the observation of other levels, or the CEF splitting in the two compounds is sufficiently different due to the very different occupation of the f-orbitals (cf. Table 3.1). Further progress in assigning all specific peaks, including their symmetry, could be be achieved via detailed calculations of all involved f-orbitals, the excited states and their particular distortion inside the crystal.

In an alternative more speculative explanation, the CDW is at the origin of the observed splitting. The CDW introduces a periodic distortion of the lattice which in turn periodically modulates the crystal electric fields. A fit to resonant x-ray measurements indeed yields a splitting of about 2 meV ($16\,\mathrm{cm}^{-1}$) in $DyTe_3$, and 20 meV ($160\,\mathrm{cm}^{-1}$) in $CeTe_3$ [146]. In both materials this effect would be compatible with the Raman measurements shown in Figs. 3.15 and 3.16. However, it is unclear if the incommensurate CDW in the rare-earth tritellurides can give rise to discrete line positions. A decision could be made in a high pressure experiment: In one case, by applying pressure it should be possible to switch on and off the level splitting along with the CDW (cf. Sec. 3.4.2) and the concomitant periodic distortion. In the other case, the splitting would appear irrespective of the presence of the CDW or may even increase with pressure.

3.4.2 High pressure phase diagram of $ErTe_3$

In $ErTe_3$ the CDW order can not only be suppressed by increasing temperature, as shown in Fig. 3.11, but also by increasing pressure. In contrast to chemical pressure (cf. the phase diagram in Fig. 3.10), applied pressure can be used to gradually suppress the phase transition down to zero temperature in a single sample. The AM can be used as a probe for the CDW phase transition and, accordingly, to map out the pressure-temperature phase diagram [133, 134].

To this end, Raman spectra were measured at various applied hydrostatic pressure values in a home made diamond anvil cell (DAC) (cf. Sec. 2.3). The experiment is most sensitive to the first CDW, if the polarizations of both incoming and scattered light are set along the crystallographic a direction with the first CDW being oriented along the c direction. The orientation of the polarizations with respect to the Te plane is sketched in the inset of Fig. 3.17. The main part of the figure shows the evolution of the AM measured with a high resolution of $3\,\mathrm{cm}^{-1}$. Panel (a) displays the temperature dependence of the Raman response at 1 GPa as a function of T. At 150 K the two main features are a phonon at $95\,\mathrm{cm}^{-1}$ and the AM below $50\,\mathrm{cm}^{-1}$. The phonon (a) stays almost at the same frequency, when the temperature is changed, but (b) hardens considerably with increasing pressure. The AM loses spectral weight with increasing temperature and moves to lower energy until it disappears between 170 K and 180 K. Thus 175 K is identified as T_{CDW1} at 1 GPa. Above 175 K the sample is in the metallic state where the spectra depend only weakly on temperature. In a second set of measurements [panel (b)] the pressure is changed while the temperature is fixed at 80 K. Increasing pressure has a similar effect on the AM as increasing temperature: The AM is more and more suppressed and finally disappears completely. In the 2.3 GPa spectrum there might still be a broad low energy peak present. But in the range between 2.3 GPa and 2.8 GPa, the AM certainly vanishes; thus $p_{\mathrm{CDW1}} = 2.5 \pm 0.3\,\mathrm{GPa}$. Similar sets of measurements were taken at isobaric or isothermal conditions to obtain the phase diagram shown in Fig. 3.18. Up to 2 GPa, T_{CDW1} decreases linearly with increasing pressure. At higher pressures the phase separation line is expected to bend down for thermodynamical reasons as T_{CDW1} approaches zero [1].

$ErTe_3$ is a promising candidate to show a quantum critical point or to become superconducting close to $p_c = 2.5\,\mathrm{GPa}$, as the de Gennes factor of Er is only 2.55 in contrast to 10.50 in Tb (cf. Table 3.1). In $TbTe_3$ superconductivity was found

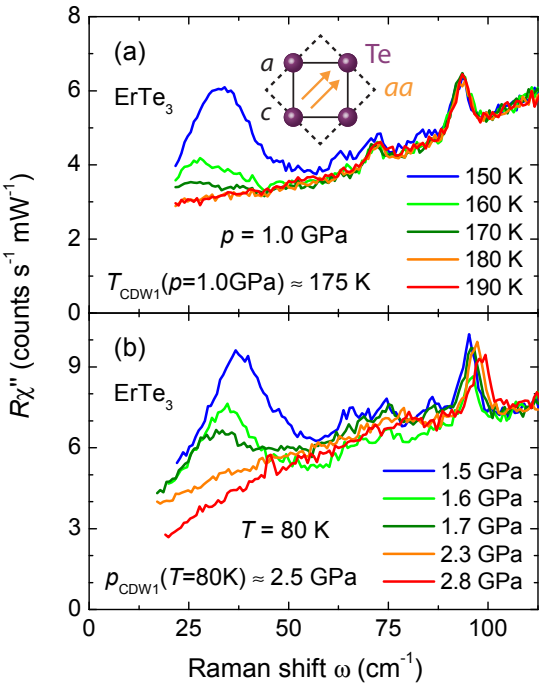

Figure 3.17: Raman spectra of $ErTe_3$ undergoing a CDW phase transition at (a) constant pressure and (b) constant temperature. The polarization of incoming and scattered light (represented by arrows) are both set along the a axis within the tellurium ac plane (dashed lines). In this configuration the AM of the first CDW with $\mathbf{Q}_{\mathrm{CDW1}} \parallel c$ can be detected. The evolution of the amplitude mode excitation below $50\,\mathrm{cm}^{-1}$ is used as a probe for the phase transition.

above 2.3 GPa at temperatures below $\approx 3\,\mathrm{K}$ [122] despite the stronger competition with magnetism. Thus, susceptibility measurements inside the pressure cell were set up as described in Ref. [88]. However, there was no evidence for superconductivity in $ErTe_3$. Regarding its magnetic properties (cf. Sec. 3.2.3), $LaTe_3$ is the most promising candidate to look for superconductivity. However, the CDW order was still not suppressed at 14.5 GPa (T_{CDW} (14.5 GPa)$\approx$ 70 K) and the sample did not survive a further increase of pressure.

A possible explanation for superconductivity in the rare-earth tritellurides is a competition for the Fermi surface. When the CDW is suppressed and the related energy gap closes, this part of the Fermi surface may then become available to Cooper pairing [122, 147]. It is still under debate, if superconductivity in $TbTe_3$ is connected to the fact that $TbTe_3$ has only one CDW and thus parts of the Fermi surface, which are not gapped by the first CDW transition, remain present [117, 119] at the lowest temperatures. This hypothesis can, in principle, be investigated in $ErTe_3$. Depending

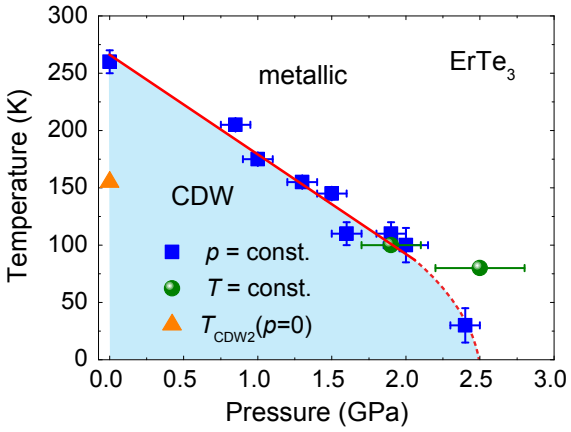

Figure 3.18: Phase diagram of $ErTe_3$. CDW phase transitions are indicated by blue squares and green spheres for isobaric and isothermal sets of measurements, respectively. The CDW phase is shaded blue. Below 2 GPa, T_{CDW1} decreases linearly with increasing pressure (solid red line), while at higher pressure values the phase separation line is expected to bend down (dashes). Above 2.8 GPa, CDW order is completely suppressed down to a temperature of 2 K. The orange triangle marks the transition into the second CDW state at ambient pressure.

on the applied pressure, the gap related to the second CDW can be opened and closed tuning the amount of electrons available to Cooper pairing. However, the second AM, i.e. the probe for the phase transition, could not be detected in the high pressure experiment. Thus, the critical pressure $p_c(\mathrm{CDW2}) \approx 1.5$ GPa was estimated from the ratio of the transition temperatures $T_{CDW2}/T_{CDW1} = 0.6$. Below 1.5 GPa we did not find evidence for superconductivity down to approximately 1.5 K. Below 0.85 GPa we lost the pressure transmission medium in the DAC.

3.4.3 Amplitude mode excitations

So far the AM was used as a probe for the phase transition. However, the exceptional purity of the tritellurides, in particular of $ErTe_3$, affords a window into a variety of properties that were considered to be theoretically solved such as the temperature dependence of AMs or their interaction with phonons. Rather, the current understanding needs to be augmented.

Spectra displaying the temperature dependence of the amplitude mode (AM) were shown in Fig. 3.11. More detailed measurements on $DyTe_3$ are plotted in Fig. 3.19. Panel (a) shows the high temperature behaviour. Above $T_{CDW1} = 306$ K, only a single phonon peak (C) is present in the plotted energy range. It survives the transition,

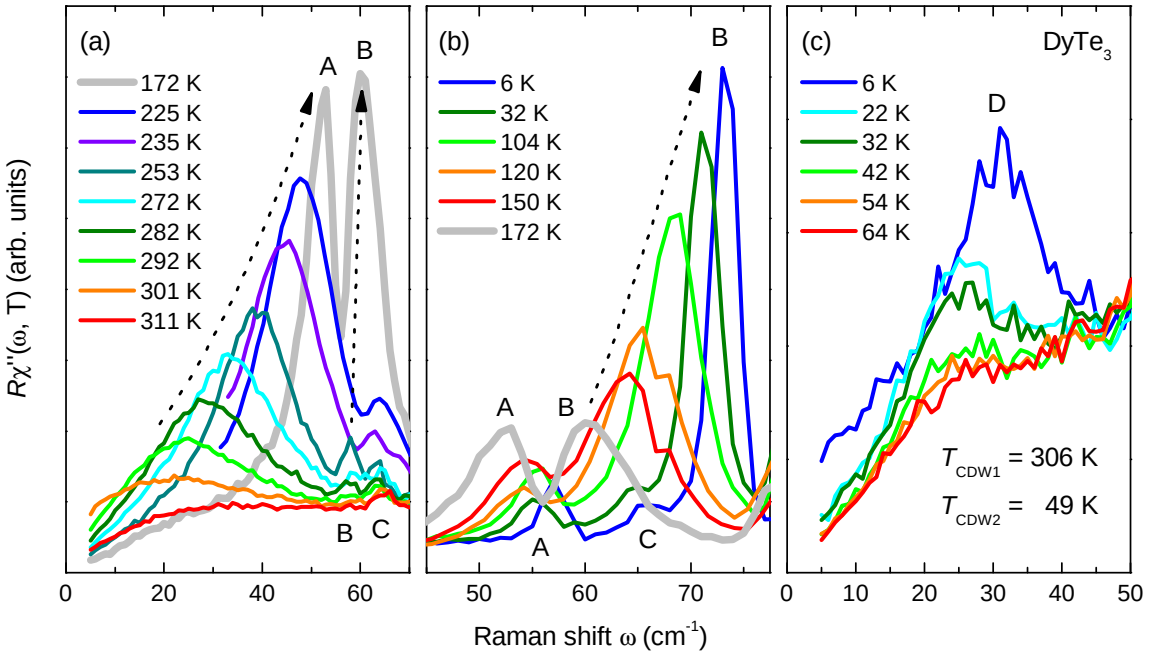

Figure 3.19: Detailed view of the temperature dependence of the A, B and C modes of $DyTe_3$ (a) above and (b) below T_{tr}. The arrows highlight the trend of modes A and B with increasing temperature. (c) Low frequency interval showing mode D for temperatures close to and below T_{CDW2}. The relative intensity ratio among panels (a-c) is 2:8:1.

without displaying any temperature dependence. Just below T_{CDW1}, the amplitude mode A appears at about $23\,cm^{-1}$, gets progressively sharper, gains intensity and moves to higher energies. In parallel, phonon mode B gets strongly enhanced, but hardly moves in position. These trends are visualized by dashed arrows. Temperature $T_{tr} = 172\,K$ is, by definition, where mode A and B have the same spectral weight [thick grey lines in Fig. 3.19 (a) and (b)]. At this crossover temperature, there is a qualitative change. Below T_{tr} [panel (b)], mode B starts behaving like an amplitude mode in that it gets stronger, sharpens and moves to considerably higher frequencies. In contrast, mode A hardens only slightly and loses spectral weight. Obviously, both modes have changed their character.

Below T_{CDW2}, an additional mode D appears at around $23\,cm^{-1}$ [Fig. 3.19 (c)]. This is the same low frequency limit as the one of mode A just below T_{CDW1} [132] and may be interpreted in terms of a sample specific impurity scattering rate [148]. In $ErTe_3$, the cleanest compound, mode A could be followed down to $8\,cm^{-1}$. Mode D moves to higher frequencies with further cooling and gains intensity. It thus can be

associated with the AM of the second CDW transition.

Peak A, B and C were fitted with Lorentzian profiles to study the temperature dependence of the peak frequencies and spectral weights. In addition to the results on $DyTe_3$, Fig. 3.20 also contains the data on $LaTe_3$ at 6 GPa, $HoTe_3$ and $ErTe_3$. In all compounds, the frequencies of modes A and B approach each other with decreasing temperature. At T_{tr}, A and B do not cross but repel each other as they have the same symmetry. This behaviour is referred to as anti-crossing in the following. The interaction strengths (off-diagonal matrix elements) used in the fits range from 4 to $6\,\mathrm{cm}^{-1}$. For $T \to 0$ the frequencies of both modes saturate. Phonon C is unaffected by the CDW transition. It stays constant in the whole temperature range and thus will be not discussed any further.

In addition to the peak positions, Fig. 3.20 also shows the spectral weight of the modes as a function of temperature. In order to compare the results obtained from different samples in different experimental setups (e.g. inside the pressure cell), the intensity was normalized to the total area below both peaks A and B. With decreasing temperature, the intensity of the A mode increases similarly as the BCS order parameter $\Delta_{BCS}(T)$ in conventional superconductors (dashed lines) [5]. At intermediate temperatures we find a transfer of spectral weight from mode A to mode B, defining T_{tr}. At the lowest temperatures, mode B looses spectral weight in $DyTe_3$, $HoTe_3$ and $ErTe_3$ which may be related to the second CDW transition and the amplitude mode associated with it.

Qualitatively, the same anti-crossing behaviour was observed in all rare-earth tritellurides studied so far. Differences in the mode frequencies and temperature dependences result from differences in T_{CDW1}, the lattice constants and the masses of the R atoms. A similar description of mode anti-crossing in RTe_3 was reported previously by Yusupov *et al.* [21] using a Ginzburg-Landau model. They found crossing temperatures T_{tr} of 190 K in $DyTe_3$ and 150 K in $HoTe_3$, in fair agreement with our results. As a coupling constant, $3.5 \pm 0.5\,\mathrm{cm}^{-1}$ was used for all RTe_3 compounds. A weakness of the approach is the use of a Ginzburg-Landau model in the whole temperature range, although it is only valid in the vicinity of the transition temperature. Approaching T_{CDW1} from below, the T dependence can be fitted almost in the limit of mean field theory, $\omega_{\mathrm{AM}} \propto (1 - T/T_{\mathrm{CDW1}})^{\beta}$, with $\beta = 0.3$ instead of 0.25.

Quantitatively, $\omega_{\mathrm{AM}}(T)$ in the whole temperature range is determined by the CDW condensate density. Mean field CDW theory predicts that the resonance frequency

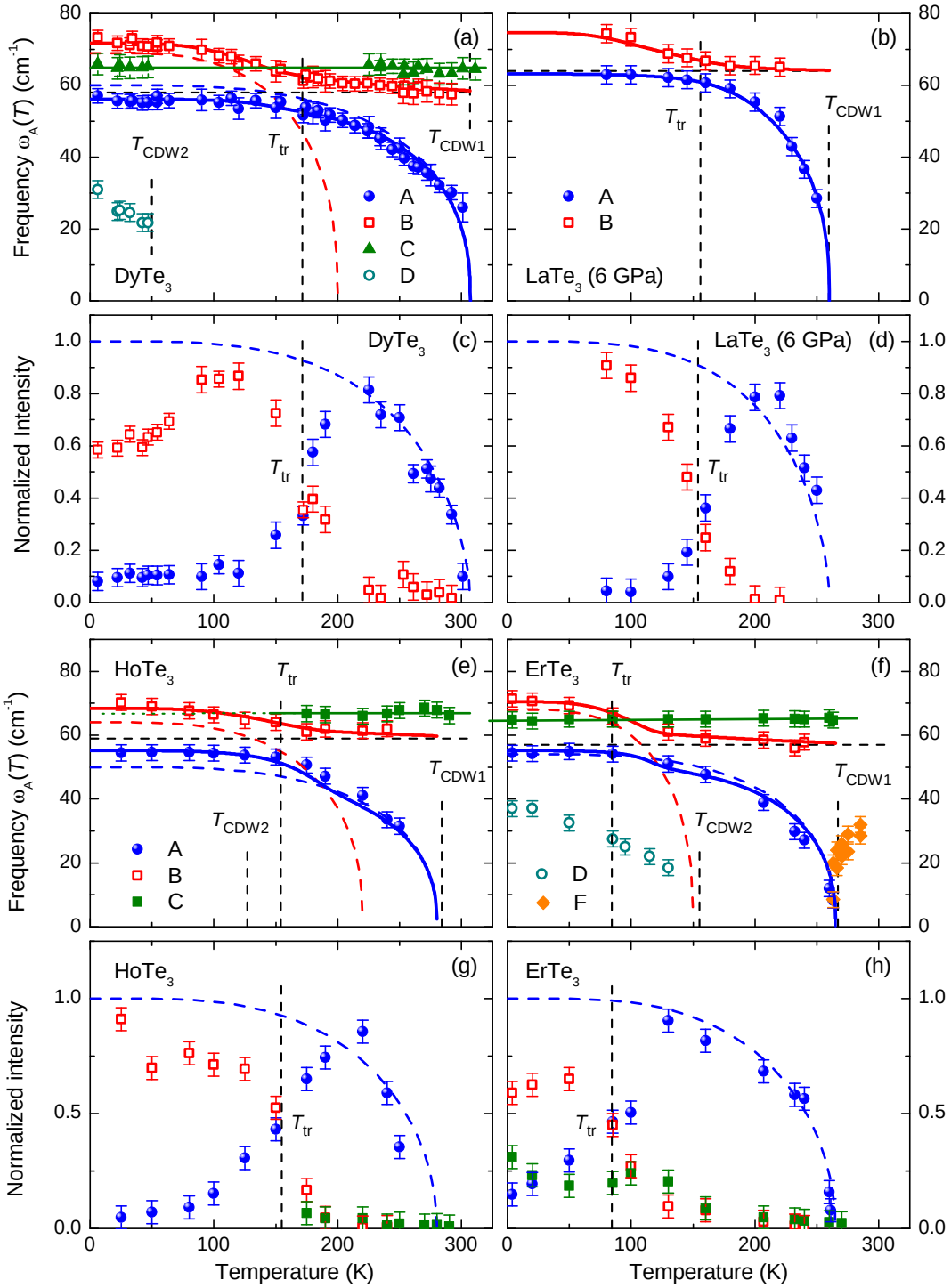

Figure 3.20: Temperature dependences of frequencies and normalized intensities for the low energy modes in $DyTe_3$, $LaTe_3$ at 6 GPa, $HoTe_3$ and $ErTe_3$. A is an amplitude mode (AM) between T_{CDW1} and T_{tr} and a phonon below while the opposite holds true for the B mode. C is a phonon unaffected by the CDW transitions; D is the AM associated with T_{CDW2}. Details are described in the text. In $ErTe_3$ charge fluctuations F above T_{CDW1} were observed [panel (f)]. They are discussed in Sec. 3.4.4.

of the amplitude mode $\omega_{\mathrm{AM}}^{(\mathrm{MF})}(T)$ is proportional to the square root of the condensate density $f_d(T)$ in the dynamic limit ($\omega \gg v_{\mathrm{F}}q$) [5]

$$\omega_{\mathrm{AM}}^{(\mathrm{MF})} = \sqrt{\lambda}\omega_{2k_F}\sqrt{f_d(T)}. \tag{3.11}$$

Here, ω_{2k_F} is the frequency of the unrenormalized CDW phonon mode at $\mathbf{q} = 2\mathbf{k}_{\mathrm{F}}$ (cf. Sec. 3.1, Eq. (3.6)). The condensate density can be approximated numerically by the BCS gap function $f_d(T) \propto [\Delta_{\mathrm{BCS}}(T)]^{4/5}$ [149]. In the $T = 0$ limit, $f_d = 1$ and thus $\omega_{\mathrm{AM}} = \sqrt{\lambda}\omega_{2k_{\mathrm{F}}}$. Then, the electron-phonon coupling constant λ can be estimated using the unrenormalized phonon frequency $\omega_{2k_F}(\mathrm{LaTe_3}) = 110 \pm 20\,\mathrm{cm}^{-1}$ from literature [130] and the $T = 0$ extrapolation of ω_{AM} from the Raman experiment. In the case of $\mathrm{LaTe_3}$ at 6 GPa this yields $\lambda(\mathrm{LaTe_3}) = 0.45 \pm 0.1$ indicating strong coupling.

However, the observed temperature dependence of the AM is not in agreement with the mean field prediction, particularly not for $T \lesssim T_{\mathrm{CDW1}}$. On cooling down below T_{CDW1}, the mean field temperature dependence, $\omega_{\mathrm{AM}}^{(\mathrm{MF})}(T) \propto \sqrt{f_d(T)} \propto [\Delta_{\mathrm{BCS}}(T)]^{2/5}$, does not match the Raman data but turns out to be an upper limit for the observed behaviour. In fact, the AM frequency increases at a lower rate, meaning that $\omega_{\mathrm{AM}}(T)$ is shifted to lower frequencies which can be interpreted qualitatively in terms of damping. Possible damping mechanisms are quasi-particle excitations, the excitation of phase modes (see Sec. 3.1), or scattering from randomly distributed impurities. The latter is supported by the low frequency limit of the AM observed close to T_{CDW1} ($23\,\mathrm{cm}^{-1}$ in $\mathrm{DyTe_3}$, $8\,\mathrm{cm}^{-1}$ in $\mathrm{ErTe_3}$). Phenomenologically, the observed temperature dependence can be described with $\omega_{\mathrm{AM}}(T) \propto f_d(T) \propto [\Delta_{\mathrm{BCS}}(T)]^{4/5}$ (red and blue dashed lines in Fig. 3.20) for all studied compounds. A theoretical model to support this observation is so far missing.

In the intermediate temperature range, we find also discrepancies to the expected behaviour. In fact, it is not possible to explain the Raman experiment with a single amplitude mode and anti-crossing with a phonon. Rather, a two-fold transition [132] at T_{CDW1} and at T_{tr} (solid red and blue lines) is compatible with the data presented in Fig. 3.20. This model is supported by calculations of the phonon dispersion in the CDW state of the rare-earth tritellurides. Due to the Te bi-layers, there are two unstable phonon branches at almost the same $\mathbf{k}$-vector[8] [130]. As the temperature is

[8] The momentum difference of the two branches here is much smaller than the difference between the two possible nesting vectors $\mathbf{Q}_1$ and $\mathbf{Q}^\star$ introduced in Sec. 3.2.2.

lowered, the CDW ordering vector $\mathbf{Q}_1$ shrinks by few percents [110] until it is energetically more favourable for the system to settle into the other predicted soft mode (red dashed line in Fig. 3.20) [132]. This view is also supported by x-ray diffraction measurements [110]. Ru *et al.* observed in $TbTe_3$ that $\mathbf{Q}_1$ in the $(11Q_1)$ superlattice peak decreases linearly from 0.297 at $T_{CDW1} = 336\,K$ to 0.292 at 180 K and then saturates at an almost constant value at a temperature close to T_{tr} [110]. The minute change in $\mathbf{Q}_1$ involved in this step, does not measurably alter the size of the gapped area on the Fermi surface and, consequently, it is unlikely to be seen in the electrical resistivity [110, 132], particularly, in comparison to the drastic modification of the FS occurring at T_{CDW1} and T_{CDW2}. Recently, the two-fold transitions observed here for $LaTe_3$ at 6 GPa, $DyTe_3$, $HoTe_3$ and $ErTe_3$ were corroborated by optical conductivity and ultrafast pump-probe experiments in $TbTe_3$ [150]. The additional transition in $TbTe_3$ occurs at $T_{tr} \approx 165\,K$ [150] fitting to the trend observed by Raman scattering for the RTe_3 family. T_{tr} roughly scales with T_{CDW1} and thus increases from about $115 \rightarrow 150 \rightarrow 160 \rightarrow 170$ for $ErTe_3$, $HoTe_3$, $LaTe_3$ at 6 GPa and $DyTe_3$, respectively (cf. Fig. 3.20).

The behaviour close to zero temperature is also explained by a two-fold transition. The higher limiting frequency of mode B at $T = 0$ fits to the theoretical prediction, that the energy of the second renormalized phonon branch, connected with the shorter low temperature $\mathbf{Q}_1$ vector, is higher than the one of the other branch [130]. In the example of $DyTe_3$ [see Fig. 3.20 (a)], the high frequency limit of the first and second branch is $60\,cm^{-1}$ and $69\,cm^{-1}$, respectively, corresponding to an energy difference of about 1 meV between the two unstable phonon branches. Altogether, we arrive at a consistent picture for the evolution of the collective excitations in RTe_3 over the whole range of existence of the CDW.

3.4.4 Fluctuations above T_{CDW1}

Charge fluctuations considerably suppress the mean-field transition temperature in low dimensional systems like the tritellurides [5, 68]. To illustrate the size of the effect, the transition temperature is calculated from BCS mean-field theory using $2\Delta/k_B T_c = 3.52$. From the experimental CDW gap sizes, Δ_{CDW1} between 180 and 400 meV [19, 114], one would expect transition temperatures T_{CDW1} between 1200 and 2600 K, i.e. well above the melting temperature of the crystals[9]. In contrast,

[9] In the rare-earth tritellurides, $2\Delta_{CDW1}/k_B T_{CDW1} \sim 15$ [19].

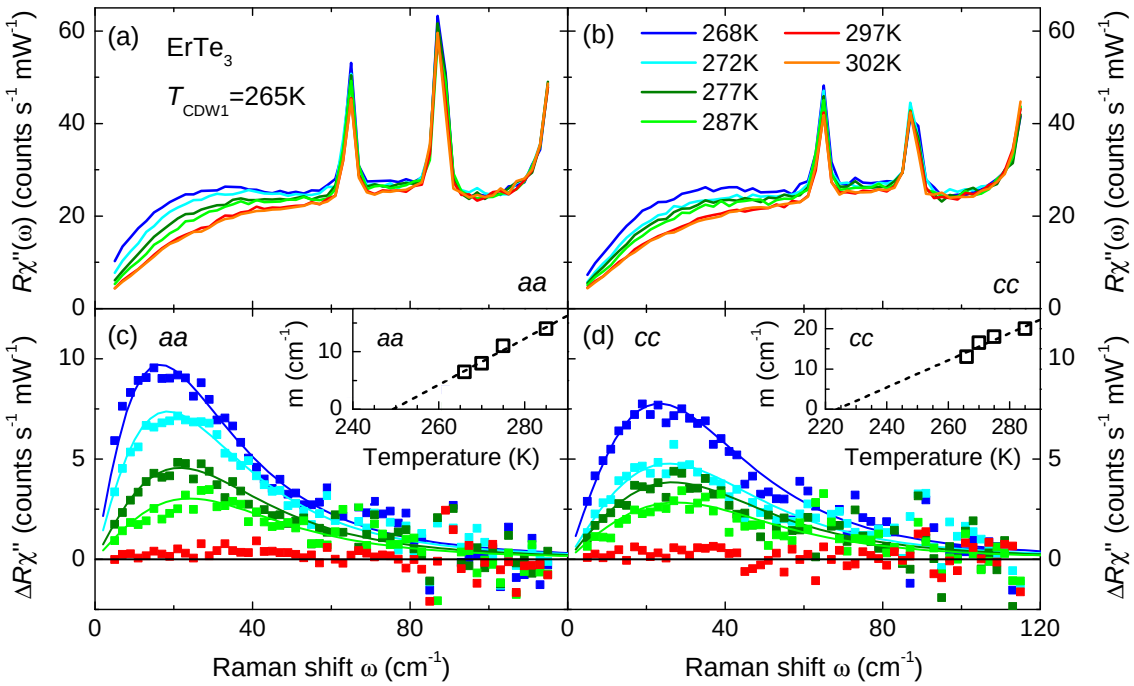

Figure 3.21: Normal state Raman scattering response and fluctuation contribution in $ErTe_3$ at low energies. (a) and (b) display the presence of a fluctuation-induced response in *aa* and *cc* polarization for a temperature range of about 30 K above T_{CDW1}. (c) and (d) show the fits according to Ref. [58] for the fluctuation contribution $\Delta R\chi'' = R\chi''(\omega, T) - R\chi''(\omega, 302\,\mathrm{K})$. The masses attributed to the fluctuations depend linearly on temperature (insets).

the experimental CDW transition temperatures range from 240 to about 500 K [111] implying that the CDW ordered state emerges from a fluctuation regime. Signatures of CDW precursor effects were observed by x-ray diffraction [110] and by optical (IR) spectroscopy [151, 152]. Only electronic Raman scattering shows the fluctuations directly and further provides information on their symmetry properties.

In experiment there is direct evidence for the charge fluctuations in *aa* and *cc* polarization as shown in Fig. 3.21. Instead of the essentially temperature independent continuum that is expected for a metal with an almost constant resistivity [110, 153], strongly T dependent shoulders at low energy are observed for $T_{CDW1} < T < 300\,\mathrm{K}$. As no additional intensity is detected in the spectrum at 302 K, it was subtracted from those at lower temperatures to highlight the fluctuation contribution to the Raman response. Panels (c) and (d) show the remaining temperature dependent contribution. Approaching T_{CDW1} from higher temperatures, the fluctuation peak softens and gets stronger. This behaviour is exactly opposite to what is observed for the amplitude

mode [cf. Fig. 3.20 (f)].

The fluctuation peak closely follows the prediction of Caprara *et al.* [58] for the exchange of charge fluctuations [solid lines in Fig. 3.21 (c) and (d)]. From the theory [58] a mass m can be assigned to the fluctuations. In the framework of Raman scattering, it is convenient to express m in units of wavenumbers, i.e. energy. m can be interpreted in terms of an inverse charge ordering (CO) correlation length ξ_{CO} that diverges at the phase transition, $m \propto \xi_{\mathrm{CO}}^{-2} \propto (T - T_{\mathrm{CO}})$ [58]. The temperature dependence of m, plotted in the insets of Fig. 3.21, follows the predicted linear behaviour, but extrapolates to a charge ordering temperature T_{CO} smaller than T_{CDW1} for $m \to 0$, i.e. $\xi_{\mathrm{CO}} \to \infty$.

As the Raman response is similar in *aa* and *cc* polarization, the symmetry of the fluctuation peaks is compatible with $A_{1\mathrm{g}}$, which indicates the survival of the C_4 rotational symmetry of the pseudo-tetragonal phase. This is compatible with a "stripe liquid" phase that does not break the any of the lattice symmetries [10]. A charge stripe liquid has been seen in the nickelates, albeit detected indirectly via the damping of magnetic fluctuations in $La_{1.725}Sr_{0.275}NiO_4$ [154]. In contrast, the presence of precursor effects due to nematic order that was intensively debated in the cuprates [2,155] and in the iron arsenides [156], can be excluded here since the excess intensity would appear in $B_{1\mathrm{g}}$ symmetry.

3.4.5 CDW gap size

The energy gap is one of the key features of a CDW system, as it corresponds to the energy the system gains through the phase transition. In the rare-earth tritellurides the energy gap is large and reaches values up to $\Delta \simeq 400\,\mathrm{meV}$ in $CeTe_3$ and $LaTe_3$ [116]. In addition to the gap size, Raman spectroscopy also provides information on the gap anisotropy (cf. Fig. 3.14) and facilitates detecting the first and second CDW gap separately.

To begin with, Fig. 3.22 compiles the results of Raman, ARPES and IR measurements as a function of the lattice parameter a, i.e. chemical pressure. Between ARPES and Raman the gap energies agree to within the experimental error, as both methods are capable to detect the maximum gap due to their momentum resolution. IR systematically underestimates the gap as it provides an average over the entire Fermi surface which contains gapped and also ungapped regions [cf. Fig. 3.7 (b) and (c)]. The averaged (IR) gap drops faster than the maximum gap (ARPES, Raman)

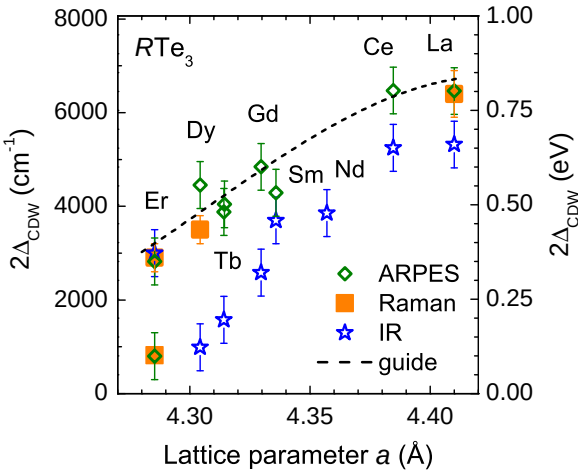

Figure 3.22: CDW gap as determined by different experimental methods. Plotted are the maximum gap values from ARPES [114, 119] and Raman scattering (this work) together with the momentum-averaged gap as derived from IR spectroscopy [89, 157] versus the lattice parameter a.

with decreasing lattice parameter (cf. Fig. 3.22). This can be explained by a broader distribution of gap values that causes the average to drop faster than the maximum gap with increasing (chemical) pressure [89].

3.4.6 Gap anisotropy and Raman vertex

The anisotropy of both CDW gaps is illustrated in Fig. 3.23 for the example of $ErTe_3$. At 54 K both CDWs are present in the sample. There is a clear signature of the large gap associated with the first CDW transition in aa polarization and of the small gap of the second transition in cc polarization. The gap edges are marked by vertical dashed lines. In the crossed polarization ac neither of the gaps is detected. The gaps are observed completely separately in the different polarizations; there is no polarization leakage requiring that the sample is single domain in the probed spot.

Now, the Raman selection rules based on the electronic unit cell are derived, according to the band structure model presented in Sec. 3.2.2, and the effective mass approximation [57] detailed in Sec. 2.1. Then, the Raman vertex is given by the second derivative, i.e. the curvature, of the energy bands plotted in Fig. 3.8. Both the Raman vertex and the energy bands at the Fermi surface are shown in Fig. 3.24. In the panels of the first column, the k_x and k_z bands intersect each other (grey lines), i.e. there is no band hybridization ($V_{xz} = 0$). In this case the Raman vertices, visualized

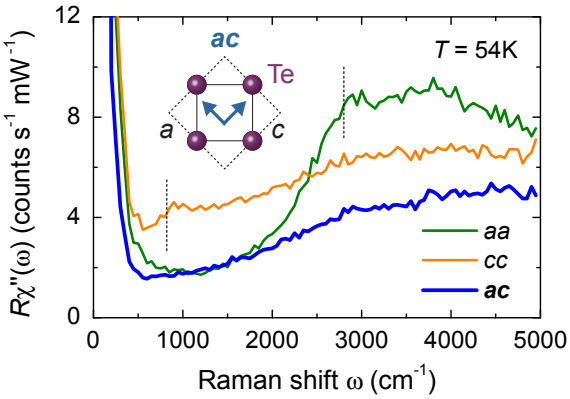

Figure 3.23: CDW gap signatures in the electronic Raman response of $ErTe_3$. The inset sketches the incoming and outgoing photon polarizations for the *ac* configuration. At $T = 54\,\mathrm{K}$ both CDWs are present in the sample but the large gap associated with the first CDW is only detected in *aa* polarization, while the second gap is observed in *cc*. The spectrum in *ac* polarization shows no signature of any gap. Gap edges are marked by dashed vertical lines.

in false color representation, stay between 0 (black) and 1 (red) in the entire Brillouin zone for *aa*, *cc* and *ac* polarization; no particular regions are strongly highlighted. In the second and third column, the band degeneracies are lifted ($V_{xz} = 0.12\,eV$). As a result, strong band curvatures are introduced close to the lifted degeneracies and the Raman vertices for parallel polarizations are enhanced by more than two orders of magnitude (yellow-white) along the diagonals of the Brillouin zone. This focusing enhances the light scattering precisely in those regions of the Fermi surface that are connected by the CDW ordering wavevectors. Panels (d)–(f) and (g)–(i) show the calculations for the electron pocket around the Γ-point (green) and the hole bands at the corners of the Brillouin zone (blue), respectively. For crossed light polarizations (bottom row of Fig. 3.24), there is no strong enhancement of γ_{ac}^2.

The electronic Raman response can be directly derived from the Raman vertices and the momentum dependences of the CDW gaps using the formalism of Ványlos and Virosztek [158]. The spectra calculated by our collaborators are shown in panels (j)–(l). For the calculation it is assumed that at $T < T_{\mathrm{CDW2}}$ the two perpendicular CDWs with ordering vectors $\mathbf{Q}_1$ and $\mathbf{Q}_2$ have fully developed gaps Δ_1 and Δ_2, respectively. $\mathbf{Q}_1$ and $\mathbf{Q}_2$ connect the corners of the electron pocket encircling the Γ point with the corners of the hole pockets. In agreement with experiment, the two gaps appear individually in the two parallel polarizations and no mixing can be observed [panels (j) and (k)]. In *ac* configuration both gaps are in principle visible [panel (l)], but the

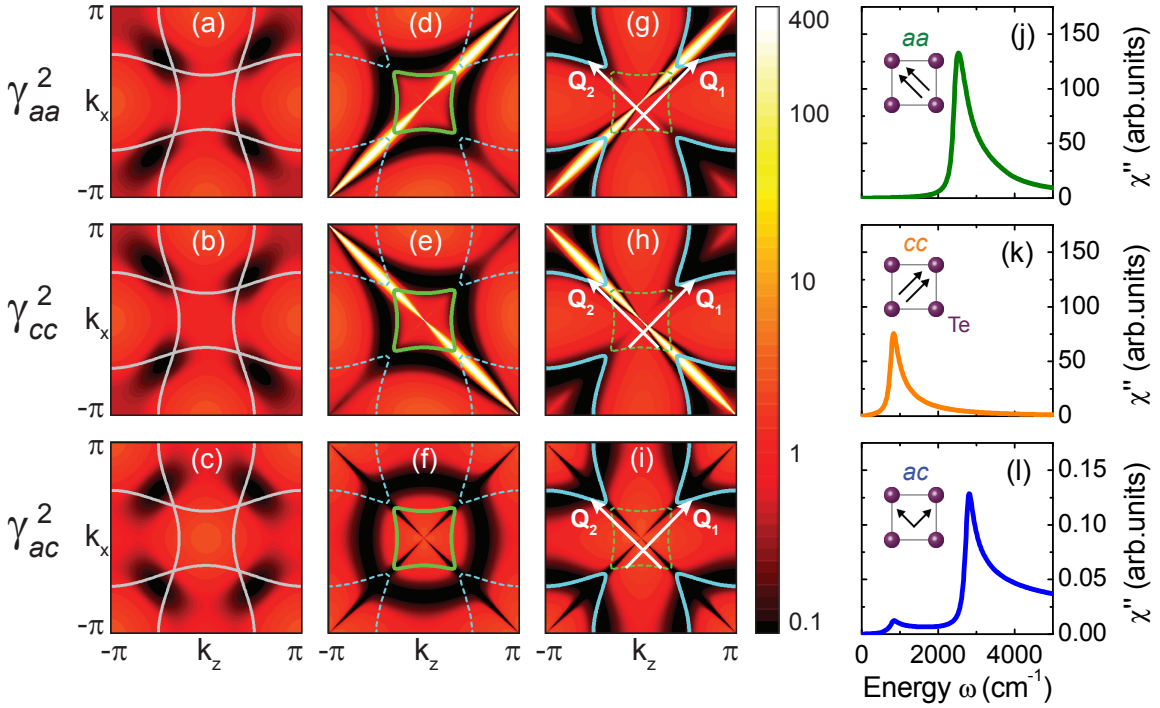

Figure 3.24: Theoretical prediction for the Raman vertices and spectra of $ErTe_3$ as derived from a tight binding band structure (a)-(c) The first row shows the vertices without 2D coupling ($V_{xz} = 0$) and the corresponding Fermi surfaces. (d)-(f) Raman vertices for the bands corresponding to the central part of the Fermi surface (green) and (g)-(i) to the outer part (light blue). The focussing effect due to the lifted degeneracy enhances the vertices by more than two orders of magnitude as indicated by the colour code. The ordering vectors are displayed in the third row. (j)-(l) All spectra are calculated at $T < T_{CDW2}$ and include both CDWs. (j), (k) For parallel polarizations one observes only the CDW with ordering vector perpendicular to the light polarizations. The response of the respective orthogonal CDW is too weak to be visible. (l) For *ac* polarization both gaps can be resolved but the overall intensity is more than three orders of magnitude lower than that in the two other configurations. This is well below the detection limit, and, in fact, no signatures of the gaps can be observed experimentally in *ac* polarization (see Fig. 3.23).

expected intensity is three orders of magnitude smaller than in *aa* and *cc* and thus cannot be detected in the experiment (see Figs. 3.23). The only scattering mechanism included in the theory is the creation of electron-hole pairs where the CDW mixes particles with wavevectors $\mathbf{k}$ and $\mathbf{k} + \mathbf{Q}_{1,2}$. Consequently, the light scattering cross section is enhanced where energy is gained due to the CDW gap opening at the Fermi surface. In the spectra, this results in a peak at the gap edge $2\Delta_{\mathrm{CDW1,2}}$ and a suppression of spectral weight below. In the real spectra, Fig. 3.23, this gap signature is superposed on the phonon response and the electron-hole continuum arising from ungapped parts of the Fermi surface. Hence, the scattering intensity in experiment does not drop to zero inside the gap and in the high-frequency limit [57].

Summarizing, the lifting of band degeneracies dramatically affects the Raman selection rules by locally enhancing the Raman vertex which is proportional to the band curvature. The sensitivity of the experiment focusses exactly on those parts of the FS which are relevant for the CDW.

3.4.7 Electronic susceptibility and CDW ordering vector

From this more technical aspect of Raman scattering we now make the connection to how the band hybridization can effect the CDW ordering vector. Above we described an enhancement of electron-photon (Raman) scattering close to the lifted band degeneracies. Now we make use of an analogy to electron-phonon scattering, where the electrons scatter from a phonon rather than a photon and the electron-phonon coupling vertex replaces the Raman vertex [148]. In particular for the case of stress phonons, the electron-phonon coupling vertex is given by the electronic part of the elastic constants, which describes how easy it is to deform an electron gas. The electrons react to a perturbation which is either the Raman photon or the displacement of ions in the lattice (phonons). Then, the coupling constant is the Raman vertex or the electronic stress tensor and both of them are proportional to the inverse effective mass tensor [69,159–161]. As a result for the system studied here, the electron-phonon coupling vertex is as anisotropic in momentum space as the Raman vertex. In particular, the coupling is enhanced close to the lifted degeneracies. In these regions in momentum space, the electronic system is much more susceptible to a deformation, i.e. CDW formation. Due to this analogy we can probe the CDW very efficiently with Raman scattering [19].

Standard CDW theory only includes a momentum independent electron-phonon

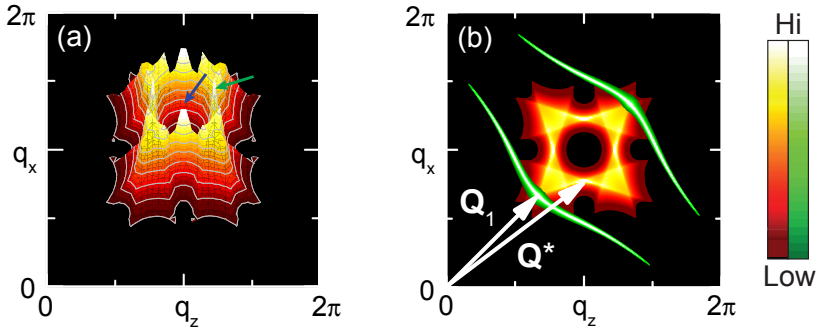

Figure 3.25: Comparison of the susceptibilities as a function of momentum transfer $\mathbf{q}$. (a) 3D plot of the real part χ'_L of the Lindhard susceptibility. There is little structure around the rim. There are two orthogonal but equivalent ordering directions $\mathbf{Q}^\star$ as indicated by a blue and a green arrow. (b) 2D superposition of the real parts of the Lindhard susceptibility (χ'_L, yellow-red) and the projected susceptibility for interband scattering transitions (χ'_P, green). For clarity, only one ordering direction is shown. It is the focusing effect of the stress tensor which selects the experimentally observed ordering wave vector $\mathbf{Q}_1$.

coupling. In this case CDW formation can be explained in terms of the complex Lindhard susceptibility,

$$\chi_L(\mathbf{q},\Omega) = 2\sum_{\mathbf{k}\alpha\beta} \frac{f(\epsilon^\alpha_{\mathbf{k}+\mathbf{q}}) - f(\epsilon^\beta_{\mathbf{k}})}{\Omega + i\delta + \epsilon^\alpha_{\mathbf{k}+\mathbf{q}} - \epsilon^\beta_{\mathbf{k}}}. \tag{3.12}$$

Here, $\mathbf{q}$ is the difference of the momenta $\mathbf{k}$ and $\mathbf{k}'$ of a scattered electron, Ω is the associated energy transfer, and α, β label the bands. The Fermi functions f in the numerator describe the transition from an occupied to an empty state. In the static limit, $\Omega + i\delta \to 0$, one obtains the real part of the susceptibility (introduced in Sec. 3.1) which must diverge in order to trigger the static electronic CDW [12]. In the general case, $\Omega + i\delta \neq 0$, the susceptibility also depends on the frequency of the external perturbation.

For the tritellurides the normal charge susceptibility χ_L has been studied by several authors [10, 12]. Fig. 3.25 (a) shows the real part of the Lindhard susceptibility within the first Brillouin zone calculated from the $ErTe_3$ band structure described in Sec. 3.2.2. Note that χ_L is not a function of momentum $\mathbf{k}$, but of momentum transfer $\mathbf{q}$. Within this picture, the selection of the ordering vector is not pronounced; the maxima in the susceptibility are almost equally high for a manifold of ordering vectors. In contradiction to experiment, the highest maxima are obtained for the ordering

vector $\mathbf{Q}^\star$ [blue arrow in Fig. 3.25 (a)] which raised the question as to whether there is another mechanism responsible for finally selecting the experimentally observed ordering vector $\mathbf{Q}_1$.

In the following, we show how the strongly enhanced coupling between electrons and stress phonons in regions of strong band curvature close to the lifted band degeneracies can select the ordering along $\mathbf{Q}_1$. We consider only interband contributions which are generally accentuated by nesting as shown in Fig. 3.9. The momentum dependent electron-phonon coupling vertex gives a contribution to the electronic susceptibility that projects out inter-band scattering transitions [162]

$$\chi_P(\mathbf{q},\Omega) = 2\sum_{\mathbf{k}} \gamma_{\mathbf{k}}^{+}\gamma_{\mathbf{k}}^{-} \frac{f(\epsilon_{\mathbf{k}+\mathbf{q}}^{+}) - f(\epsilon_{\mathbf{k}}^{-})}{\Omega + i\delta + \epsilon_{\mathbf{k}+\mathbf{q}}^{+} - \epsilon_{\mathbf{k}}^{-}}. \tag{3.13}$$

Here, $\epsilon_{\mathbf{k}}^{\pm}$ are the two bands defined in Eq. (3.8). Formally, χ_P is similar to the Lindhard susceptibility, but it is weighted by the effective mass vertices $\gamma_{\mathbf{k}}^{\pm} = \gamma_{aa}^{\pm} + \gamma_{cc}^{\pm}$ derived from the bands as described and depicted in the previous section (Fig. 3.24)[10].

Fig. 3.25 (b) illustrates the importance of including the electron-phonon coupling vertex, by plotting the real parts, χ_L' (yellow) and χ_P' (green), of both susceptibilities. Whereas the Lindhard susceptibility χ_L' has maxima of comparable height for several different ordering vectors [Fig. 3.25 (a)] and therefore does not lead to an unambiguous selection of one of them, χ_P' contributes to the instability at the proper location in $\mathbf{q}$ space. Finally, both susceptibilities overlap at the experimentally observed ordering vector $\mathbf{Q}_1$ [Fig. 3.25 (b)]. Furthermore, as noted by Yao *et al.* [10], any enhancement of the averaged electron-phonon coupling strength (cf. Sec. 3.1) will drive the system further towards the observed order along $\mathbf{Q}_1$. These two effects conspire to minimize the dependence on model details.

To support these findings, it can be shown theoretically that even χ_P alone, in principle, can give rise to a phonon renormalization in a similar way as nesting does. The phonon energy is lowered at the $\mathbf{q}$ values where the susceptibility is large (cf. Eq. (3.6) in Sec. 3.1), as shown in Fig. 3.26. In the calculation, the bare phonon frequency $\omega_{\mathbf{q}}$ was assumed to be independent of momentum, as any mild momentum dependence will not affect the general behaviour near the experimental nesting vector $\mathbf{Q}_1$. In panel (a), the colour code represents the the renormalized phonon frequency

[10]Note that χ_P is only C_4 symmetric in the larger momentum range $\mathbf{q}_{x(z)} = (0, 4\pi)$ and vanishes for $V_{xz} = 0$.

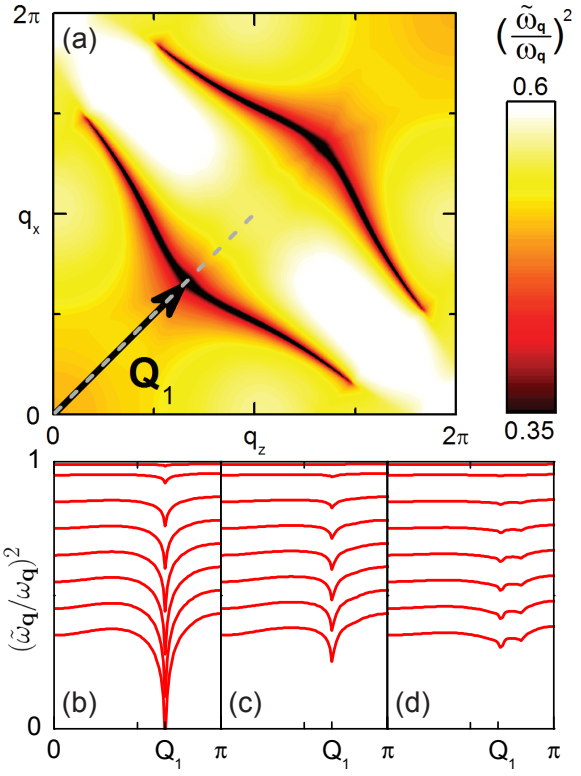

Figure 3.26: Renormalized phonon dispersion relation. (a) Renormalized phonon frequency $(\tilde{\omega}_{\mathbf{q}}/\omega_{\mathbf{q}})^2$ with electron-phonon coupling $\lambda_{\mathbf{q}=0} = 0.5$ and diagonal hopping terms set for clarity to 10 times smaller values than those used in Figs. 3.8, 3.9 (b) and 3.24. The arrow represents the ordering wavevector $\mathbf{Q}_1$ as determined experimentally. (b)-(d) Cuts along the line $q_x = q_z$ [dashed line in panel (a)] for various values of the electron-phonon coupling starting at $\lambda = 0.01$ (top curve) and then ranging between $\lambda = 0.05$ and $\lambda = 0.65$ (bottom curve) with incremental steps of 0.1. Each panel is for a different value of the hybridization parameters: (b) $V_{xx}/10$, $V_{xz}/10$; (c) $V_{xx}/4$, $V_{xz}/4$; and (d) V_{xx}, V_{xz}.

$(\tilde{\omega}_{\mathbf{q}}/\omega_{\mathbf{q}})^2$ in $\mathbf{q}$-space. In the calculation, the dimensionless electron-phonon coupling constant[11] (for $\mathbf{q} = 0$) is $\lambda = 0.5$ [19]. To emphasize the effect, the diagonal hopping terms V_{xx} and V_{xz} are set to 10 times smaller values than those used in Figs. 3.8, 3.9 (b) and 3.24. To get a feeling for the relevant parameters, panels (b)–(d) further display the phonon softening along the $(0,0) - (\pi,\pi)$ Brillouin zone cut [dashed line in panel (a)] for $V_{xz}/10$, $V_{xz}/4$ and V_{xz} and λ in the range from 0.05 to 0.65. For a large coupling, $\lambda = 0.65$, and small interaction $V_{xz}/10$, even χ_P alone can bring the CDW phonon frequency down to zero energy at the wavevector $\mathbf{Q}_1$ and thus induce

[11] The electron-phonon coupling can be estimated from the $T = 0$ limit of the amplitude mode frequency as described in Sec. 3.4.3; $\lambda = 0.4 \pm 0.1$

the static lattice distortion that goes along with the CDW. This predicted phonon renormalization remains to be experimentally confirmed by neutron or inelastic x-ray scattering (RIXS), since Raman scattering is limited to small momentum transfer $\mathbf{q} \ll \mathbf{Q}_1$. The focusing effect of the large curvature of the energy bands given by the mass tensor is very sensitive to the hybridization parameter V_{xz} [Fig. 3.26 (b)–(d)]. In the case of $ErTe_3$ the main mechanism driving the CDW transition is still the standard Lindhard theory, while the additional contributions presented here are corrections for selecting the ordering direction.

As an outlook, it seems interesting to which extent this novel scenario can be of more general relevance for driving phase transitions into other broken symmetry ground states, for instance in the proximity of superconductivity competing or coexisting with CDW order.

Chapter 4

Magnetic phase transitions in manganese silicide

MnSi is one of the most intensively studied itinerant magnets showing a variety of indications for non-trivial spin-charge and spin-lattice effects. Since Raman scattering provides access to anisotropic electron and lattice dynamics one can expect new insight and crucial tests of theoretical ideas. Below, the results obtained as a function of temperature, polarization and magnetic field are summarized and discussed, after briefly outlining basic material properties. Most of the results presented in this chapter have been published in Ref. [64].

4.1 MnSi phase diagram and chiral magnetic order

To set the stage for the following sections, the phase diagram of MnSi and the different types of magnetic order are briefly reviewed. The phase diagram of MnSi [29] is determined by a competition of three well separated energy and length scales [24, 31]. The strongest one is ferromagnetic exchange between itinerant electrons that favours a parallel alignment of spins on length scales of a few lattice constants. On an intermediate scale, the Dzyaloshinsky-Moriya (DM) interaction favours a canted arrangement of neighbouring spins [25–27]. It is an anisotropic super-exchange interaction resulting from the missing inversion symmetry and spin orbit coupling. Together with the ferromagnetism the spins arrange in a helix along $\mathbf{q}$ that extends over many lattice constants and has a pitch of about $2\pi/q = 180\,\text{Å}$ (Fig. 4.2). The weakest energy scale is due to the crystal electric field which locks the propagation direction of the helix to the [111] directions of the crystal. A typical size of magnetic domains is 10^4 Å [164].

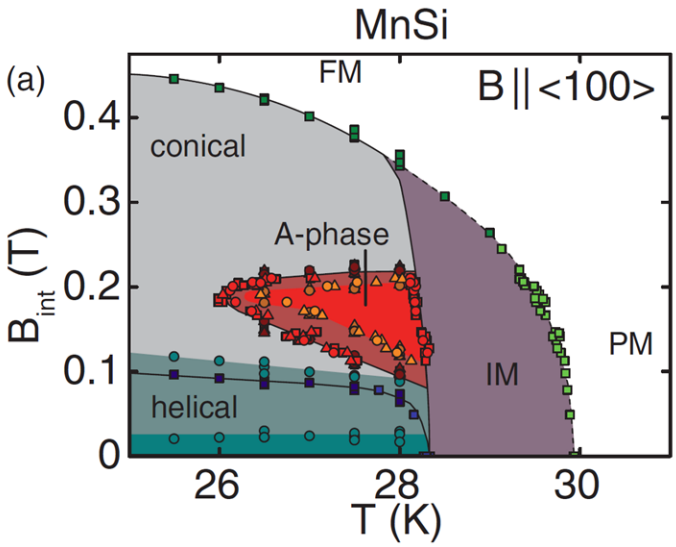

Figure 4.1: Magnetic phase diagram of MnSi. The external field is oriented along the [100] direction of the crystal. The interplay of magnetism, temperature and crystal symmetry results in differently ordered phases denoted as PM (paramagnetic), FM (field polarized ferromagnetic), IM (intermediate), helical, conical and the A-phase (skyrmion lattice) as described in the text. From [163].

The phase diagram is shown in Fig. 4.1 [163]. Above the ordering temperature $T_C \approx 29\,\mathrm{K}$ MnSi is paramagnetic, but magnetic fluctuations are present up to $10\,T_C$ [166]. Roessli *et al.* find that the fluctuations are chiral and incommensurate with the underlying lattice [167]. Right above T_C (region labeled as IM (intermediate) in Fig. 4.1), several different experimental techniques find anomalies, e.g. in susceptibility, specific heat, ultrasound attenuation and neutron scattering [48, 163, 168, 169]. First attempts to explain the observations in this regime were proposed recently by Janoschek *et al.* in terms isotropic fluctuations that drive the phase transition first order [48] in agreement with a Brazovskii type scenario [49].

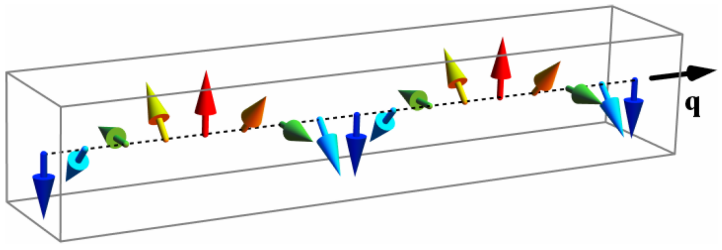

Figure 4.2: Spin arrangement in the helical phase. The magnetization winds around the propagation direction **q**. From [165].

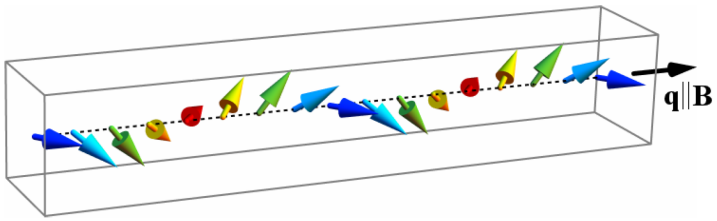

Figure 4.3: Spin arrangement in the conical phase. The spins tilt to the direction of the magnetic field **B**, while the pitch of the helix remains unchanged. With increasing field, the angle of the cone decreases. The ordering vector **q** orients along **B**. From [165].

If an external magnetic field **B** is applied in the ordered state, the spin helix depins from the [111] directions and orients along the external field, **q** ∥ **B**. The crystal gets magnetized by tilting the spins into the direction of **B** as shown in Fig. 4.3; the pitch of the helix remains unaffected [170], since it is determined by the ferromagnetic exchange and the Dzyaloshinskii-Moriya interaction strength. The magnetization increases linearly as the angle of the cone closes. In MnSi, it saturates in the field polarized state having $0.4\,\mu_B$ per Mn atom at 0.62 T and 1.4 K which is smaller than the value of $1.4\,\mu_B$ which is obtained in the paramagnetic region [171].

Yet there is another tiny phase pocket between the helical, the conical and the paramagnetic state which was identified as the skyrmion phase [39]. The concept of skyrmions was first proposed in particle physics by Tony Skyrme [172]. In the case of solid state magnetism it is a topologically stable field configuration with particle-like properties. This new type of magnetic order, depicted in Fig. 4.4, consists of spin vortices which are arranged in a triangular lattice. The skyrmion lattice orients perpendicular to the external field **B** but is independent of the crystal orientation [39].

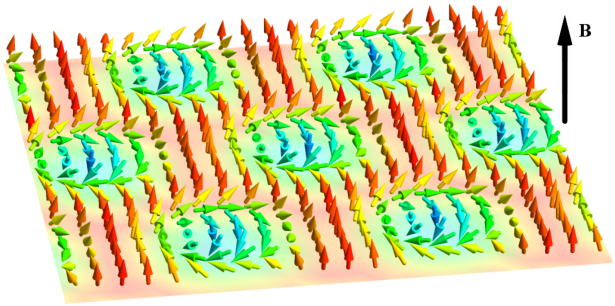

Figure 4.4: The Skyrmion lattice. A topologically stable spin configuration consisting of magnetic vortices. The triangular skyrmion lattice is oriented perpendicular to the external field **B**. From [165].

4.2 Crystal structure of MnSi

MnSi crystallizes in the non-centrosymmetric cubic $B20$ structure [173, 174] with a lattice constant of $a = 4.558$ Å [166]. It can be assigned to space group $P2_13$ (No. 198) and the unit cell contains four Mn and four Si atoms at the Wyckoff $4a$ positions. This corresponds to atoms located at $(u, u, u), (1/2 + u, 1/2 - u, -u), (-u, 1/2 + u, 1/2 - u), (1/2 - u, -u, 1/2 + u)$ [174]. The positional parameters u in the case of MnSi are $u_{Mn} = 0.138$ and $u_{Si} = 0.845$ [166]. Allowed symmetry operations are four three-fold rotation axes around the [111] directions and three screw axes that combine a two-fold rotation around the [100] directions followed by a displacement of $(a/2, 0, 0)$.

To visualize the $B20$ structure, it can be thought of as a distorted fcc rock salt structure where the Mn and Si atoms approach each other as they are displaced in different [111] directions [175]. For comparison, the positional parameters for a rocksalt structure would be $u_{Mn} = 0.25$ and $u_{Si} = 0.75$. The distortions lower the symmetry in comparison to rock salt [53, 175] and result in an unusual local coordination of the atoms [174]. Each Mn atom is surrounded by seven Si atoms; one at a distance of 2.305 Å in a [111] direction, three at 2.701 Å, and another three at 2.836 Å. The six nearest neighbour atoms of the same type are at the equidistance of 2.795 Å.

In an ideal $B20$ structure the atoms would be placed at $u_{\text{ideal}} = 1/(4\tau) = 0.1545$ and $1 - u_{ideal} = 0.8455$, with the golden ratio $\tau = (1 + \sqrt{5})/2$. The nearest neighbour coordination would be seven atoms of the other kind, each of them at the same distance of $a\sqrt{3}/(2\tau)$ being 2.440 Å in case of MnSi. However, the distortion from the

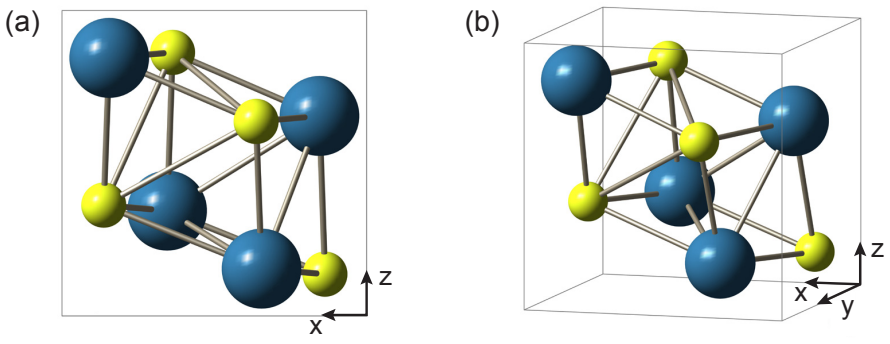

Figure 4.5: Crystallographic unit cell of MnSi. Depicted is a view on a (100) surface (a) and a perspective view (b). The unit cell consists of four manganese (yellow) and four silicon atoms (blue); it has cubic symmetry but lacks a center of inversion. (crystal structure pictured using *Balls & Sticks* [108])

ideal structure is essential for the stability of the structure [176] and occurs in every real $B20$ crystal [177]. From this point of view, the $B20$ structure can be considered the crystalline approximation of a face centered icosahedral quasicrystal[1] [177].

The high-quality single crystals used in this work were prepared in an ultra-high vacuum compatible image furnace [179]. With optimized parameters the residual resistivity ratio (RRR) of the single-crystals grown can be as high as 300. Further details about the preparation and the characterization can be found in Ref. [30]. The sample used for the Raman experiments had a RRR of approximately 100.

4.3 Infrared conductivity vs. conventional transport

Transport and Hall conductivity experiments revealed a plethora of unusual electron properties [34,36,37,56]. Unconventional electron dynamics was also observed by optical transport and interpreted in terms of anisotropic scattering rates $\Gamma = 1/\tau$ [51]. Here the advantages of Raman scattering become apparent immediately, though several conclusions derived from the Fermi-surface integrated infrared (IR) response shed light on various anomalies already earlier. To prepare for the discussion on anisotropies of the carrier relaxation rates (Sec. 4.5.2), it is briefly summarized what is already known from conductivity experiments that do not provide any resolution in momentum space in cubic crystals.

IR spectroscopy is a standard procedure to derive transport lifetimes $\tau(\omega, T)$ or scattering rates $\Gamma = 1/\tau$ as well as the optical mass $m^*/m_b = 1 + \lambda(\omega, T)$ from the reflectivity [180,181] or from ellipsometry data; here, m_b is the band mass, and $\lambda(\omega, T)$ the mass enhancement. In MnSi, Mena *et al.* measured the optical conductivity and compared it with longitudinal transport [51] as shown in Fig. 4.6 (a). On cooling down, the optical conductivity increases as expected for a metal. To fit the data, an extended Drude model [180] is applied,

$$\sigma(\omega) = \frac{\omega_P^2}{4\pi} \frac{1}{1/\tau(\omega) - i\,\omega\, m^\star(\omega)/m}. \tag{4.1}$$

With $\omega_P = 18700\,\mathrm{cm}^{-1}$ the plasma frequency, one obtains the frequency dependence of the effective mass m^* and the scattering rate $\Gamma = 1/\tau$ as shown in Fig. 4.7.

Two features are particularly remarkable. First, m^* assumes negative values at

[1] The Nobel price in Chemistry 2011 was awarded to Dan Shechtman "for the discovery of quasicrystals". He observed an icosahedral point group symmetry in a metallic solid [178].

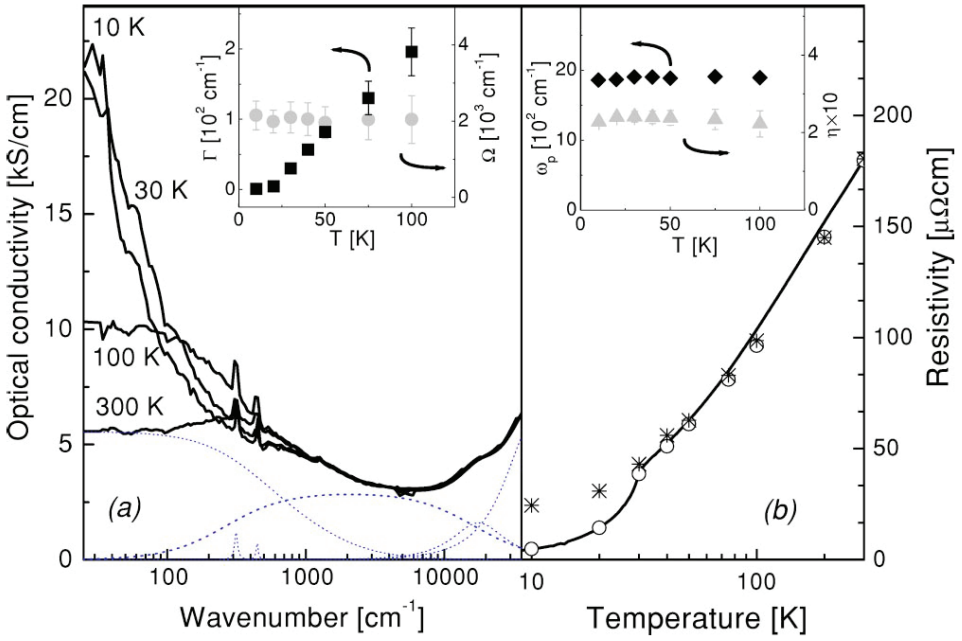

Figure 4.6: Optical conductivity (a) and DC transport (b) in MnSi. The DC resistivity obtained from transport measurements is compared with the DC resistivity derived from the optical conductivity via a Drude fit (stars, Eq. (4.1)) and a phenomenological fit (open circles, Eq. (4.2)). The fit parameters are presented in the insets. From [51].

300 K and frequencies below about 180 cm^{-1} which was not commented by Mena *et al.* but will be picked up in Sec. 4.5.2. At low temperature there is a strong increase of the optical masses towards low frequency [Fig. 4.7 (a)]. Second, the scattering rate $\Gamma = 1/\tau(\omega)$ [Fig. 4.7 (b)] changes its frequency dependence from constant at 300 K, which is the expected Drude behaviour, to linearly increasing between 30 and 300 cm^{-1} for all the lower temperatures shown. With decreasing temperature it stays linear in energy and gets steeper. In contrast, a ω^2 dependence is expected from Fermi liquid theory at low frequencies. In the $\omega \to 0$ limit, shown in Fig. 4.6, the Drude scattering rates (stars) deviate from the Fermi liquid behaviour observed in transport measurements (solid line) in the helical phase.

Since the conventional Drude fit fails to reproduce the DC resistivity ρ_{DC} at low temperature, the authors propose a phenomenological non-Drude model [51] which was originally proposed for the cuprates having strongly momentum-dependent single particle scattering rates [52],

$$\sigma(\omega) = \frac{\omega_{\mathrm{P}}^2}{4\pi} \; \frac{i}{(\omega + i\,\Gamma)^{1-2\eta}\,(\omega + i\,\Omega)^{2\eta}}. \tag{4.2}$$

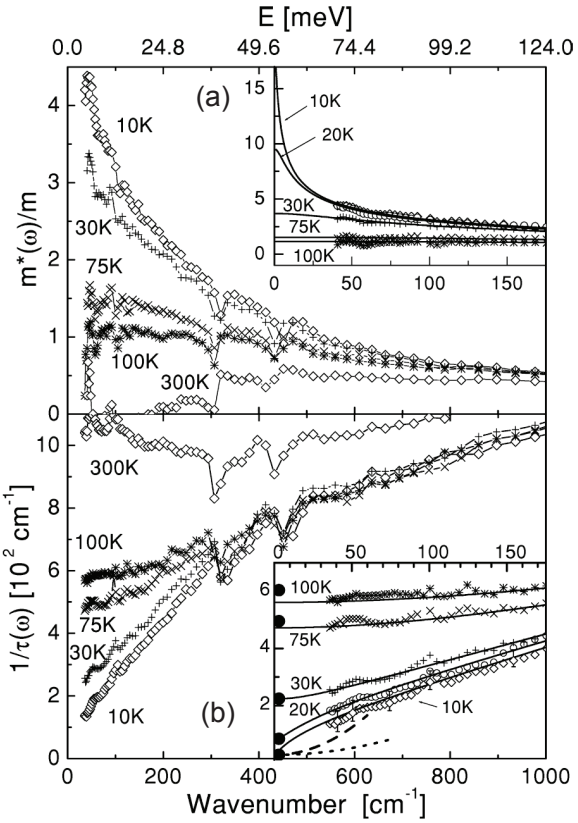

Figure 4.7: Dynamical carrier properties of MnSi obtained from optical spectroscopy [51]. (a) Effective mass and (b) frequency-dependent scattering rate as obtained from the optical conductivity at different temperatures. Insets: Same quantities below 200 cm^{-1}. Symbols represent the experimental data and thick lines the calculation from a non-Drude fit (Eq. (4.2)). In the inset of panel (b) the DC extrapolation values (solid dots) correspond to the derived DC resistivity (open circles) shown in Fig. 4.6(b). In addition, the frequency dependences expected from Fermi-liquid theory (dashed line) and spin fluctuations (dotted line) are plotted for 10 K. From [51].

Using the fitting parameters shown in the inset of Fig. 4.6, more weight is given to ρ_{DC}. Then, the DC optical conductivity can be matched with ρ_{DC} requiring a minimal set of adjustable parameters [51]. The corresponding $\omega \to 0$ extrapolation is shown in the insets of Fig. 4.7. In the case of 20 and 10 K, the non-Fermi liquid fit has a negative curvature below 50 cm^{-1} yielding the reduced DC relaxation rates plotted as open circles in Fig. 4.6 (b). The Fermi liquid behaviour in transport measurements in the helical phase of MnSi, is well established [32, 51, 182], however, it remains an open question whether the carrier relaxation depends on the momentum k [54, 56], calling for measurements providing some k resolution such as Raman scattering.

4.4 Results

Raman spectra on MnSi were recorded in the temperature range $1.8 < T < 310\,\mathrm{K}$ for different light polarizations. As an example, Fig. 4.8 shows the Raman response $R\chi''_{\mathrm{i,s}}$ at 288 and 17 K, with a full set of polarization combinations of (i) incoming and (s) scattered light. The spectra are offset by $0.7\,\mathrm{counts}\,(\mathrm{s}\cdot\mathrm{mW})^{-1}$ each. Along with the measurements the linear combination of symmetry components contributing to the spectra are given. All spectra consist of sharp peaks, originating from lattice excitations, and a very weak continuum arising from electron-hole or other excitations having a broad spectrum. In the following sections results on phonons and the electronic continuum are presented separately. The main emphasis is placed on the temperature range below 50 K close to the helimagnetic transition at $T_{\mathrm{C}} = 29\,\mathrm{K}$. In addition to temperature, also a magnetic field of 4 T was used as a control parameter to suppress the helimagnetic modulation.

4.4.1 Phonons

In the raw data shown in Fig. 4.8 a number of phonons are present. To give an overview, for all symmetries the phonon frequencies measured at 17 and 288 K are listed in Table 4.1. Also listed, for comparison, are the results published by Tite *et al.* [183] who measured well above room temperature using various high laser powers. According to our model for the laser heating (cf. Sec. 2.2.4) their laser power and focus size yield temperatures up to 650 K in the probed spot. The huge heating ΔT implies an inhomogeneous broadening of the phonon lines explaining the different line widths reported in Ref. [183] and in the results presented here. Tite *et al.* assume a linear temperature dependence of the phonon frequency $\omega_{\mathrm{ph}}(T)$ above room temperature and extrapolate $\omega_{\mathrm{ph}}(T)$ down to 295 K in satisfactory agreement with the data presented here (cf. Table 4.1). But in this work, most importantly, the temperature range was extended down to 4 K, including the helimagnetic phase transition.

The energies of the two strongest T_2 lines are only slightly different from those of the E phonons. Therefore, the E and T_2 modes in the $x'x'$ and rl spectra appear as double peak structures as these polarization configurations contain both symmetry contributions. Fig. 4.9 provides a closer look on the double peak structure around $320\,\mathrm{cm}^{-1}$ at 17 K. In $x'x'$ polarization [panel (a)], comprising contributions from

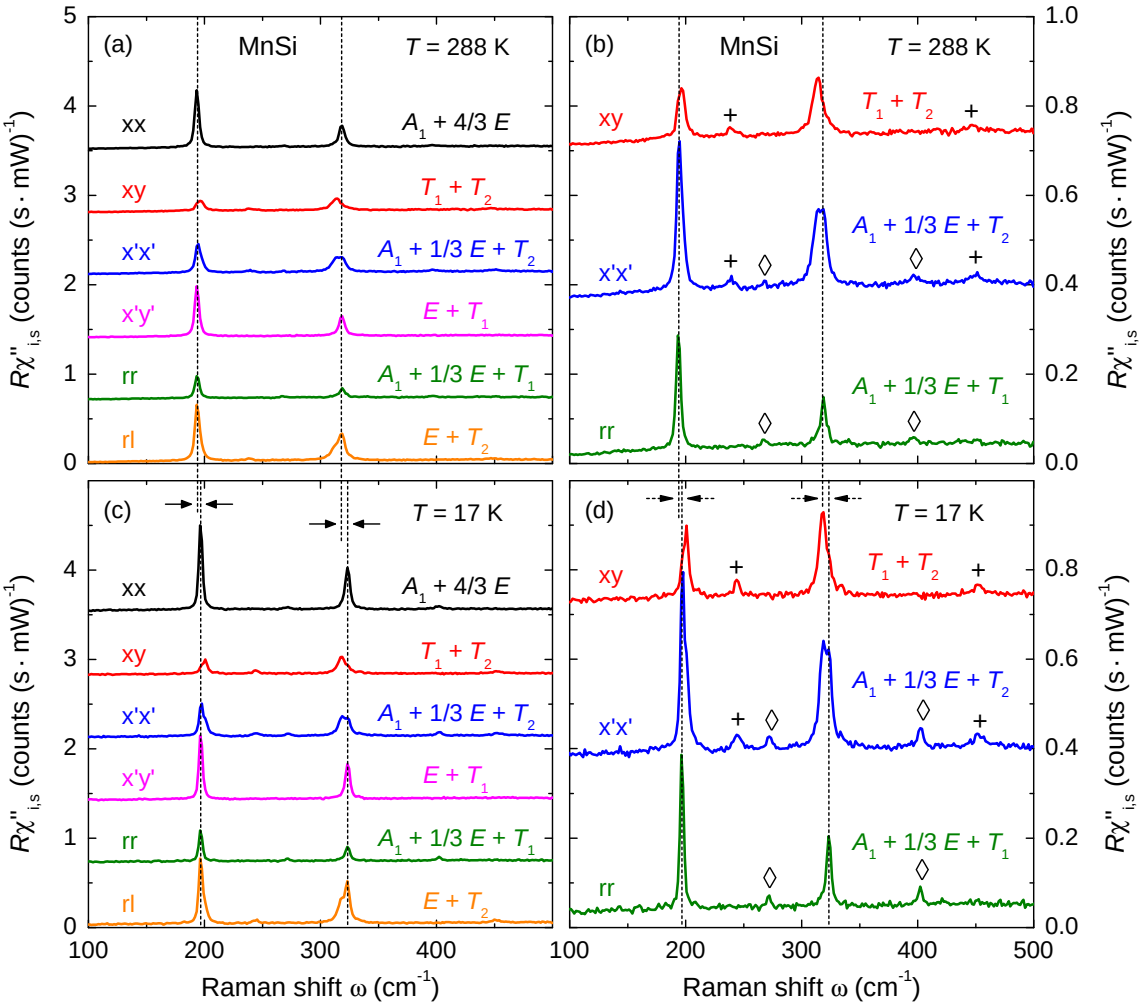

Figure 4.8: Raman spectra of MnSi at (a, b) 288 and (c, d) 17 K. Plotted is the Raman susceptibility $R\chi''_{i,s}(\omega, T)$ as a function of the frequency shift ω. The spectra are measured with different sets of light polarizations with respect to the crystallographic axes. For each polarization combination the symmetry components are indicated. To point out the small frequency differences between E and T_2 phonons, the positions of the two E phonons are marked by dashed lines. Whenever both E and T_2 excitations contribute to a spectrum, double peak structures appear. Upon lowering the temperature, all phonons harden. The black horizontal arrows indicate these frequency shifts for the E phonons. Panels (a) and (c) show a full set of six polarization combinations, consecutively offset by 0.7 counts $(\mathrm{s}\cdot\mathrm{mW})^{-1}$. Panels (b) and (d) only show xy, $x'x'$ and rr spectra offset by 0.35 and on an expanded intensity scale to point out the weak A_1 (diamonds) and T_2 (crosses) phonons.

	Phonon frequency ω_{ph} [cm^{-1}]		
	$T \approx 295\,\mathrm{K}$ (Ref. [183])	$T = 288\,\mathrm{K}$ (this work)	$T = 17\,\mathrm{K}$ (this work)
A_1	268	268	271
A_1	398	396	402
E	193	**193.5**	**196.9**
E	319	**318.5**	**323.4**
T_2	194	**196.3**	**200.9**
T_2	236	239	244
T_2	316	**313.9**	**318.6**
T_2	–	–	332
T_2	448	447	452

Table 4.1: Energies of the Raman active phonon modes in MnSi. At low temperatures all nine predicted peaks are resolved. There are no phonons in T_1 symmetry. Room temperature measurements are shown together with the phonon positions derived in Ref. [183]. The frequency values of the four intense phonons can be determined with an accuracy of about $\pm 0.2\,\mathrm{cm}^{-1}$ using Voigt fits (bold face). The other phonons are determined with a precision of $\omega_{\mathrm{ph}} \pm 1\,\mathrm{cm}^{-1}$.

A_1, E and T_2 symmetry, a double peak is present originating from the E phonon at $323.6\,\mathrm{cm}^{-1}$ and the T_2 phonon at $328.6\,\mathrm{cm}^{-1}$. In $x'y'$ polarization the E phonon peak can be observed individually at $323.4\,\mathrm{cm}^{-1}$ [panel (b)]. The T_2 phonons can be observed independently in xy polarization (Fig. 4.8). Details as to the derivation of the line positions and widths can be found in Sec. 2.2.3.

The less intense phonons are hardly visible on the scale of Fig. 4.8 (a) and (c). On the expanded scale of panels (b) and (d) they are clearly observable. There are two weak A_1 and three weak T_2 phonon lines, marked by diamonds ($\diamondsuit$) and crosses ($+$) in Fig. 4.8, respectively. For the weak phonons the frequency error is approximately $\pm 1\,\mathrm{cm}^{-1}$. In the temperature range above 40 K, spectra were recorded with steps of approximately 50 K. Around the transition at $T_{\mathrm{C}} = 29\,\mathrm{K}$, we measured spectra at temperatures spaced by not more than 1 K. With decreasing temperature all phonons shift to higher energies. At the transition this trend is reversed, and the phonons

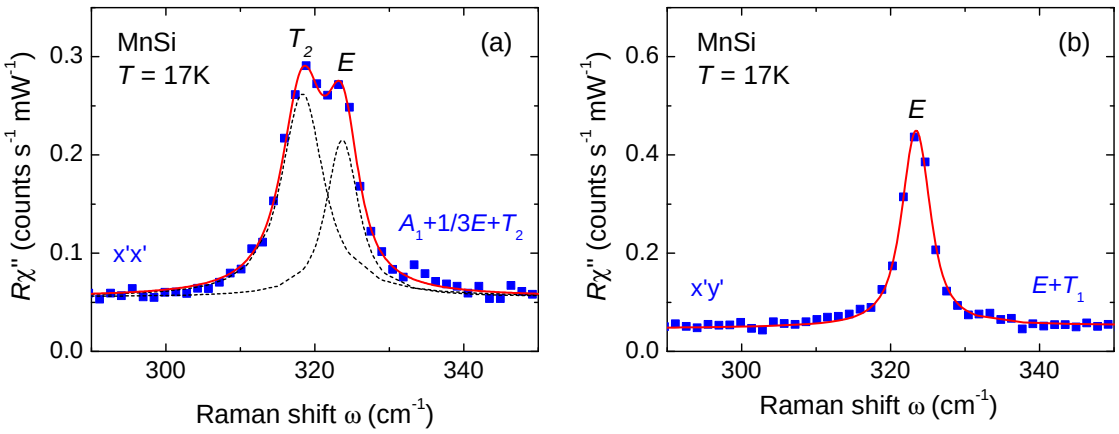

Figure 4.9: Voigt fits of phonons in MnSi. (a) in $x'x'$ polarization the Raman spectrum contains contributions from A_1, E and T_2 symmetry. Two phonons of different symmetry result in a double peak. In $x'y'$ polarization the E phonon peak can be observed individually, but its position and width differ by 0.26 and 0.74 cm^{-1}, respectively, from those found in $x'x'$. The differences are in the order of the experimental accuracy of frequency ($\pm 0.2\,\mathrm{cm}^{-1}$) and width ($\pm 0.3\,\mathrm{cm}^{-1}$). As the fit of a single peak requires less free parameters, $x'y'$ spectra are used to determine the positions and widths of E phonons (cf. Table 4.1 and Figs. 4.12).

soften by typically half a percent. The results for the temperature dependence of the position and line width of the four strong phonons will be discussed in Sec. 4.5.1.

Via linear combinations of the spectra measured at different polarizations, the pure symmetries can be extracted as explained for tetragonal systems in Ref. [57] and for cubic MnSi in Sec. 2.1.2. Then, one spectrum comprises all excitations having the same symmetry as shown in Fig. 4.10. However, by adding and subtracting the spectra, artifacts (marked by stars) may be introduced originating from tiny frequency shifts of the intense phonons. A Factor group analysis predicts nine optical phonons: Two in E, five in T_2, and two in A_1 symmetry [63]. As expected, no phonons are present in T_1 symmetry where vibrational Raman transitions are forbidden in general [138]. We find all nine predicted phonons (marked by vertical arrows), including the so far missing T_2 phonon at 332 cm^{-1}, which can be resolved in the high energy shoulder of the strong T_2 peak at 318.6 cm^{-1}. A comparison with the phonon positions in the iso-structural compound FeSi [63] supports this finding. The inset of Fig. 4.10 (a) shows all symmetries containing weak phonons on an expanded scale. Panel (b) demonstrates that the six spectra shown in Fig. 4.8 (c) are consistent. This holds true for both the phonons and the continuum. While the symmetry resolved spectra

are less precise in determining the phonon positions and linewidths for the artifacts mentioned above, they are essential in the discussion of the electronic continuum, where narrow artifacts can be disregarded.

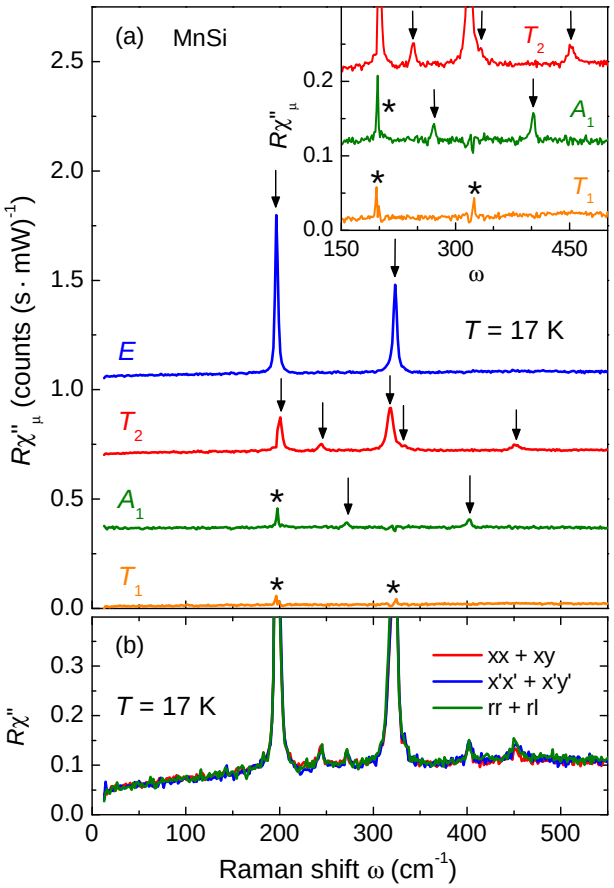

Figure 4.10: Symmetry resolved spectra of MnSi at 17 K. (a) Pure symmetries can be obtained via linear combinations of Raman spectra measured with different polarization settings according to Eq. (2.5). For clarity the spectra are offset by 0.35 counts $(\mathrm{s}\cdot\mathrm{mW})^{-1}$. All Raman active phonons $(2E + 5T_2 + 2A_1)$ predicted by factor group analysis [63] are observed (marked by arrows). In the A_1 and T_1 spectra, there are additional peaks due to polarization leakage (marked by stars). The inset shows the weaker phonons of T_2 and A_1 symmetry on an expanded intensity scale (spectra offset by 0.1 counts $(\mathrm{s}\cdot\mathrm{mW})^{-1}$). The T_1 spectrum contains the chiral excitations. It is featureless except for polarization leakage (stars), but the intensity of the continuum is in the same order of magnitude as the other symmetries. (b) Consistency check. Two measurements with the same incoming polarization and orthogonally polarized scattered photons cover the full response of the sample, thus their sums must be invariant.

4.4.2 Electronic continuum

The electronic continua observed in the pure symmetries are plotted in Fig. 4.11 for various temperatures in the range $13 \leq T \leq 288\,\mathrm{K}$. The continua were obtained by subtracting the individually fitted phonons from the spectra (see Sec. 2.2.3). Although the fits were reproducible and stable there are occasionally remainders of phonons after the subtraction, particularly in the low temperature spectra having phonon line widths comparable to the spectral resolution. The data are relatively noisy in general since the scattering cross sections are low, and the spectra in pure symmetries are the result of subtraction procedures (cf. Sec. 2.1.2). Note that the intensities are lower than $0.05\,\mathrm{counts}\,(\mathrm{s}\cdot\mathrm{mW})^{-1}$. This corresponds to 1 Raman photon per milliwatt laser power and frequency interval of $2\,\mathrm{cm}^{-1}$ arriving at the CCD detector every 20 seconds.

In all symmetries, the spectra exhibit a substantial temperature dependence at low energies. The E, T_1 and T_2 spectra are also temperature dependent at higher energies. At 13 K, the A_1, E, and T_1 spectra are too steep below $50\,\mathrm{cm}^{-1}$ to allow the extrapolation to zero at $\omega \to 0$ to be observed. In fact, $\chi''(-\omega) = -\chi''(\omega)$ is

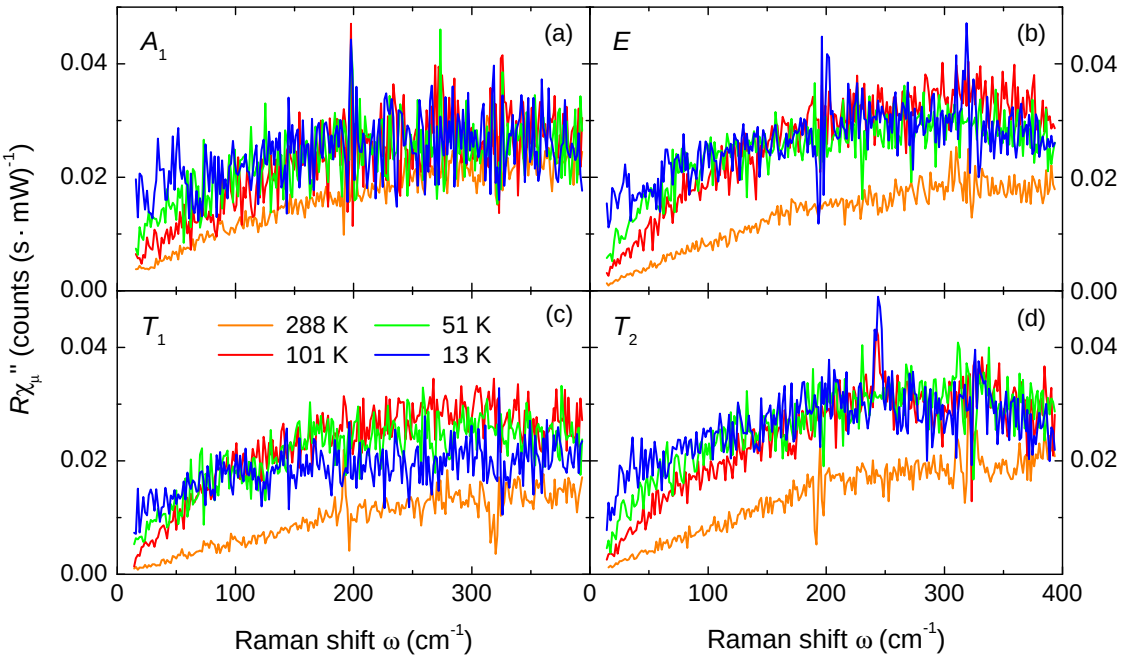

Figure 4.11: Temperature and symmetry dependence of the electronic continua in all pure symmetries $\mu = A_1, E, T_1, T_2$. The response is obtained via linear combinations of xy, $x'y'$, rr and rl spectra. Phonons were fitted with Voigt profiles and subtracted.

expected since, for causality reasons, the response is antisymmetric. Only the T_2 spectra show the expected linear energy dependence at all temperatures and extrapolate approximately to zero. The variation with temperature implies a substantial increase of the initial slope of the response. Note that also the T_1 component of the response shows a distinct temperature dependence. Particularly, it is different from zero at all temperatures as shown in Fig. 4.11. Possible mechanisms will be discussed in Sec. 4.5.2.

As discussed in detail by Opel and coworkers [81], the inverse initial slope, $(\partial\chi''(\omega)/\partial\omega)^{-1}$ corresponds to a Raman resistivity and is therefore a useful quantity to be compared with transport measurements. It can be extracted from the Raman response in a similar fashion as the conductivity from optical spectra (IR). In the Raman case, the requirements as to the known spectral range are much more relaxed than in optical spectroscopy since the Kramers-Kronig transform converges rapidly [81]. The results of this analysis, in particular those in the zero-frequency limit, will be shown and discussed in the following.

4.5 Discussion

The results on lattice and carrier properties show rather conventional behaviour at high temperatures while anomalies are present close to T_C and in the magnetically ordered state below. First, the phonons will be discussed, followed by the electronic response. In each case, we start with the behaviour above the helimagnetic transition at T_C followed by a detailed study close to T_C. The argumentation largely follows Ref. [64].

4.5.1 Temperature dependence of the phonons

For a detailed analysis we selected the four phonons with the highest intensities which are both E phonons and two of the five T_2 phonons. Their positions and linewidths were derived from Voigt fits as explained in Sec. 2.2.3 and shown exemplarily in Fig. 4.9. The temperature dependences of the frequencies and linewidths are plotted in Figs. 4.12 and 4.13. From room temperature down to 35 K, the typical blue shift and line narrowing is observed. Right above T_C, in the range between 35 and 29 K, there is a dip in all phonon frequencies. Below the transition the phonons anomalously soften by approximately 0.5 cm^{-1} as can be seen more clearly in panels (c) and (d). Except

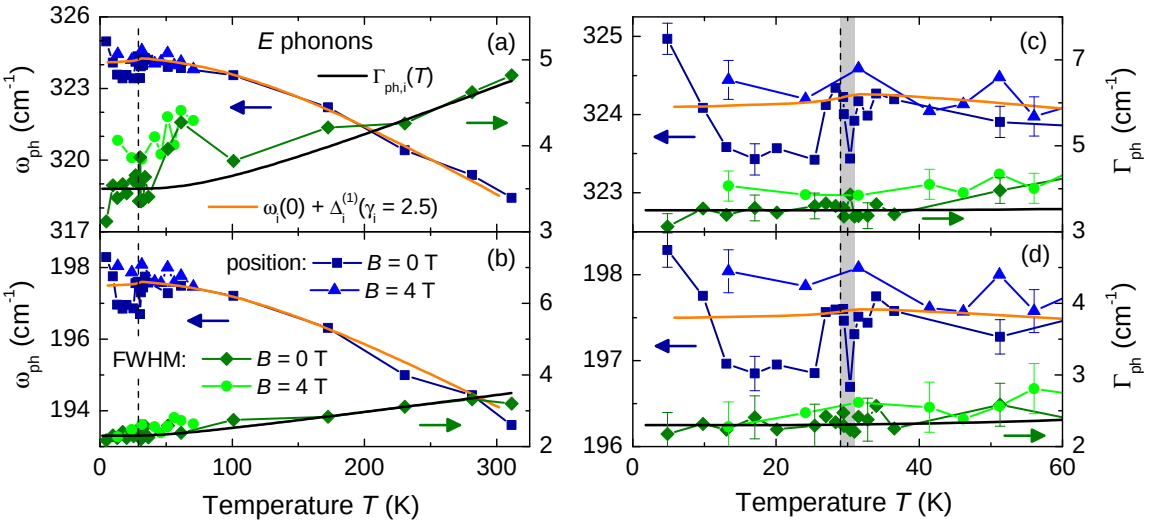

Figure 4.12: Temperature dependence of the E phonons. Plotted are the frequencies (left scales) and linewidths (right scales) of the two strongest lines (labeled by $E^{(318)}$ and $E^{(194)}$ according to their room temperature positions) with representative error bars. (a) and (b) show the analysis for the full temperature range, (c) and (d) zoom in on low temperatures. For both phonons, $E^{(318)}$ and $E^{(194)}$, the linewidth can be described by the model of anharmonic decay [184] [black lines, Eq. (4.4)]. The main contribution to the frequency change is due to thermal expansion and can be described by a constant Grüneisen parameter $\gamma_i = 2.5$ above 35 K [orange line, Eq. (4.9)]. Right above T_C (dashed vertical line) in the fluctuation disordered regime [50] (shaded) there is a dip in the phonon frequency. If the helical order is suppressed by a magnetic field of 4 T (triangles and circles), the anomalies in the phonon frequencies disappear.

for the high-energy T_2 mode all lines harden again below approximately $1/2\,T_C$. The T_2 mode at 201 cm^{-1} [Fig. 4.13 (d)] reaches the same energy as found at T_C whereas the E lines (Fig. 4.12) even exceed the low-temperature extrapolation value expected from the range $T > T_C$.

All anomalies in the temperature dependence[2] of the phonon energies vanish completely in a magnetic field of 4 T (see Fig. 4.12), being well above the upper critical field of the helimagnetic modulation at 0.6 T. Magnetization measurements indicate that a crossover temperature T_{cr}, that separates the regimes governed by either magnetism or temperature, continues to exist above the critical field. For MnSi at $B = 4$ T, the crossover from field polarized ferromagnetism to paramagnetism is approximately at $T_{cr} = 40$ K [185]. However, no anomalies in the phonon positions and widths are detected at this crossover suggesting that the phonon anomalies originate

[2]Temperature is measured with a Cernox resistor having a vanishingly small magneto-resistance of less than 0.2% for magnetic fields up to 4 T.

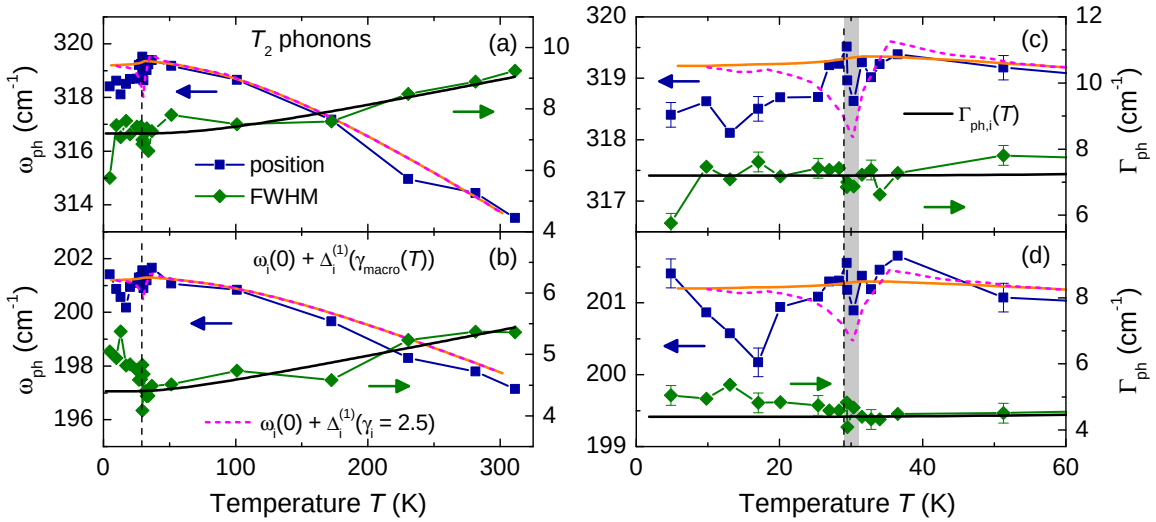

Figure 4.13: Temperature dependence of T_2 phonons. Shown are the frequencies (left scales) and linewidths (right scales) of the two strongest lines (labeled by $T_2^{(314)}$ and $T_2^{(197)}$ according to their room temperature positions) with representative error bars. (a) and (b) show data for the full temperature range, (c) and (d) zoom in on low temperatures. The phonon width deviates from the predictions of the Klemens model [184] [black lines, Eq. (4.4)] only for the $T_2^{(197)}$ phonon below T_C (dashed vertical line). Above 35 K the frequency change of both phonons can be explained in terms of a thermal expansion shift $\Delta_i^{(1)}(T)$ [orange lines, Eq. (4.9)] assuming a constant $\gamma_i = 2.5$ for all phonon modes i. There is a dip in the phonon frequency right above T_C in the fluctuation disordered region [48, 50] (shaded). The dip can be reproduced qualitatively if the macroscopic Grüneisen parameter $\gamma_{macro}(T)$ is inserted into Eq. (4.9) as described in the text (dashed magenta line). In the helimagnetic phase the phonon frequencies are lower than those predicted by the thermal expansion.

from chiral order, but not from ferromagnetism.

Previous to the discussion of the phonon temperature dependences some theoretical concepts are introduced. In the harmonic approximation of lattice dynamics, the phonon frequencies are not temperature dependent, and the phonon lifetime is infinite. To describe real systems, anharmonic contributions to the lattice potential have to be taken into account. Because of the anharmonicity, an optical mode can exchange energy with other lattice modes [184]. Collisions between phonons take place and result in a finite phonon lifetime and a renormalized resonance frequency. Frequency shift and broadening can be described in terms of the real and imaginary part of the self energy [186]

$$\Sigma_i(T) = \Delta_i(T) + i\,\Gamma_i(T) \tag{4.3}$$

corresponding to the position and width of phonon i, respectively. The anharmonic effects can be treated with perturbation theory and were extensively studied by several authors [184, 186–188].

Here we limit the discussion to optical phonons in the center of the Brillouin zone, because only these can be observed by Raman scattering. In the presence of anharmonic interactions and assuming energy and momentum conservation, an optical phonon with $\mathbf{q} = 0$ decays into two acoustic phonons of opposite wave vectors $\omega_1(\mathbf{q}, j_1) + \omega_2(-\mathbf{q}, j_2) = \omega_{\mathrm{ph}}$. The indices j_1 and j_2 label acoustic phonon dispersion branches. In the commonly used Klemens model [184] it is assumed that the most relevant decay channels are symmetric, $\omega_1(\mathbf{q}, j_1) = \omega_2(-\mathbf{q}, j_1) = \omega_{\mathrm{ph}}/2$, and within the same acoustic phonon branch, e.g. j_1. Then the temperature dependence of the linewidth of phonons reads

$$\Gamma_{\mathrm{ph},\,i}(T) = \Gamma_i(0)\left[1 + \frac{2 \cdot \lambda_{p-p,i}}{\exp(\frac{\hbar\omega_i(0)}{2k_{\mathrm{B}}T}) - 1}\right]. \tag{4.4}$$

The width $\Gamma_i(0)$ and position $\omega_i(0)$ of the i-th Raman line for $T \to 0$ can be obtained by extrapolating $\Gamma_{\mathrm{ph},\,i}(T)$ to zero temperature from the range above T_{C} before the anomalies set in. As temperature rises, the linewidth increases by two times the Bose factor at $\omega_i(0)/2$ in the symmetric decay channel. $\lambda_{p-p,i}$ was introduced as the only fitting parameter and is interpreted as phonon-phonon coupling strength. More general calculations including asymmetric decay channels result in a better agreement with experiment in some semiconductors [186, 189]. In MnSi, however, asymmetric phonon decays as well as four phonon processes turn out to be negligible, and the Klemens model provides a reasonable fit to the linewidth of all phonons studied, except $T_2^{(197)}$ at low temperatures.

The frequency shift of the peaks is described by the real part $\Delta_i(T)$ of the self energy in Eq. (4.3). The temperature dependence of phonon i reads

$$\omega_{\mathrm{ph},i}(T) = \omega_i(0) + \Delta_i(T). \tag{4.5}$$

Here, only the two lowest-order contributions, $\Delta_i(T) = \Delta_i^{(1)}(T) + \Delta_i^{(2)}(T)$, will be discussed. A more detailed description including higher order terms can be found in Refs. [186] and [189]. The leading term, $\Delta_i^{(1)}(T)$, originates from the thermal lattice expansion. Note that the lattice expansion results from the phonon amplitude, hence

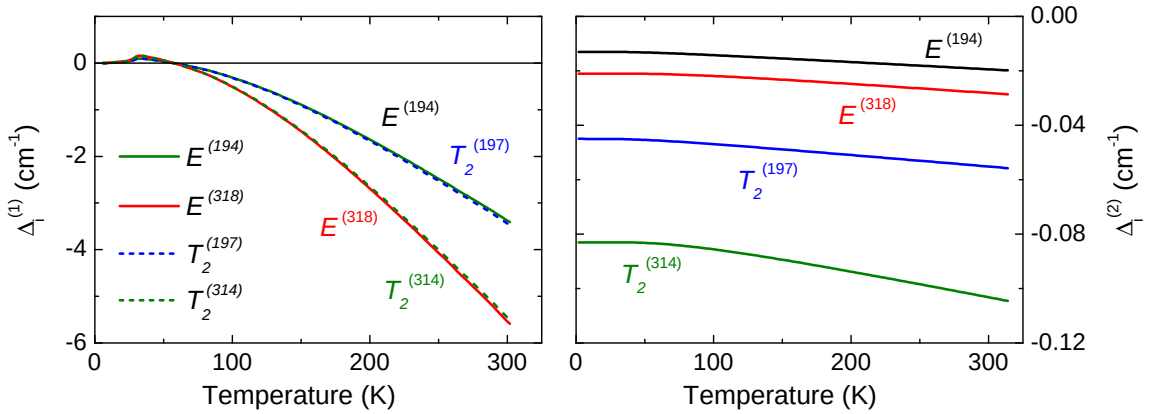

Figure 4.14: First and second order contributions to the phonon frequency shift. (a) The first order contribution to the phonon width $\Delta_i^{(1)}(T)$ is due to thermal expansion while (b) the second order contribution $\Delta_i^{(2)}(T)$ results from anharmonic decay. $\Delta_i^{(2)}(T)$ is about two orders of magnitude smaller than $\Delta_i^{(1)}(T)$ and thus negligible.

the occupation number, and not from the decay of optical phonons. The second term, $\Delta_i^{(2)}(T)$, describes the frequency shift due to phonon decay. Before we derive $\Delta_i^{(1)}(T)$ we show that $\Delta_i^{(2)}(T)$ is small for the phonon energies and the temperature range studied here.

The second-order contribution $\Delta_i^{(2)}(T)$ results from the anharmonic decay of phonons. In analogy to a harmonic oscillator the resonance frequency drops when damping is included. The approximate relationship between the linewidth Γ_i (Eq. (4.4)), the eigen-frequency $\omega_i(0)$, and the resonance frequency $\omega_{\mathrm{ph},i}$ (peak maximum), $\omega_{\mathrm{ph},i} = \sqrt{\omega_i(0)^2 - \Gamma_i^2}$, of a damped harmonic oscillator yields a shift

$$\Delta_i^{(2)}(T) = -C_i \left[1 + \frac{4 \cdot \lambda_{p-p,i}}{\exp \frac{\hbar\omega_0}{2k_\mathrm{B}T} - 1} \right], \tag{4.6}$$

with $C_i = \Gamma_i(0)^2/2\omega_i(0)$ and all other parameters as defined above. The additional factor 2 in the numerator as compared to Eq. (4.4) is due to the damped harmonic oscillator approximation. For the phonon-phonon coupling $\lambda_{p-p,i}$, the values obtained from Eq. (4.4) are used again. It turns out that $\lambda_{p-p,i}$ is stronger for E than for T_2 phonons and also stronger for the high frequency modes (cf. Table 4.2). For the phonons considered here, the frequency $\omega_i(0)$ is high in comparison to the width $\Gamma_i(0)$ (cf. Table 4.2). Consequently, the coefficient C_i is small and the contribution of $\Delta_i^{(2)}$ to the phonon shift (Fig 4.14) is at least two orders of magnitude smaller than

	Fit parameter			
	$E^{(194)}$	$E^{(318)}$	$T_2^{(197)}$	$T_2^{(314)}$
$\omega_i(0)$ [cm^{-1}]	197.5	324.1	201.2	319.2
$\Gamma_i(0)$ [cm^{-1}]	2.3	3.5	4.4	7.2
$C_i = \Gamma_i(0)^2/2\omega_i(0)$ [cm^{-1}]	0.013	0.019	0.048	0.081
$\lambda_{p-p,i}$	0.15	0.2	0.07	0.14

Table 4.2: Parameters used to calculate the temperature dependence of phonon positions and widths. According to their symmetry and room temperature frequency, the phonons i are labeled $E^{(194)}$, $E^{(318)}$, $T_2^{(197)}$, and $T_2^{(314)}$. $\omega_i(0)$, $\Gamma_i(0)$ are experimentally determined constants. The phonon-phonon coupling strength $\lambda_{p-p,i}$ results from the fit of the phonon width according to Eq. (4.4) and was used again in Eq. (4.6).

the thermal expansion shift $\Delta_i^{(1)}$ and therefore negligible.

$\Delta_i^{(2)}$ gives significant contributions only for broad phonons with low frequencies, or temperatures in excess of the Debye temperature Θ_{Debye} being as high as 600 K here [188, 190, 191]. Obviously, the dominating contributions to the widths and the frequency shifts of the phonons result from different mechanisms and thus are not directly interrelated. This explains why the anomalies in the phonon frequencies do not have a direct correspondence in the linewidths.

The first order term $\Delta_i^{(1)}$ depends on the unit cell volume. In general, a smaller unit cell volume results in higher phonon resonance frequencies since the forces between the atoms increase with decreasing distance[3]. The frequency shift can be quantified via the microscopic Grüneisen parameter γ_i of mode i being defined as the negative logarithmic derivative of a normal-mode frequency ω_i with respect to the volume V [192],

$$\gamma_i = -\partial(\ln \omega_i)/\partial(\ln V). \tag{4.7}$$

The related thermodynamic quantity is the macroscopic Grüneisen parameter $\gamma_{\text{macro}}(T)$ which is a weighted average of all contributions including lattice, charges and magnetism [193]. For the phonon part it can be shown that the relative weight is given

[3]The phonon width is, in first order, not affected by a decreasing unit cell, as it depends on the anharmonicity of the lattice potential rather than its strength. This can be seen in Fig. 3.17, where, with increasing applied pressure, a phonon is shown to shift in frequency but does not measurably change its width.

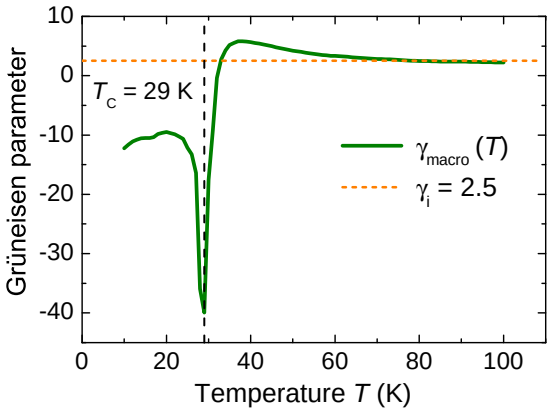

Figure 4.15: Grüneisen parameters in MnSi. The macroscopic Grüneisen parameter $\gamma_{\mathrm{macro}}(T)$ (green) is derived from thermodynamic properties and compared with the constant phonon Grüneisen parameter $\gamma_i = 2.5$ (orange) which describes the shift of the Raman modes i due to thermal expansion.

by their individual contributions to the specific heat [192]. While $\gamma_{\mathrm{macro}}(T)$ is approximately constant in conventional insulators, it may vary considerably with temperature in complex metallic systems whenever different contributions determine the thermodynamic properties [193, 194]. $\gamma_{\mathrm{macro}}(T)$ can be determined from experimentally accessible thermodynamic properties alone [194],

$$\gamma_{\mathrm{macro}}(T) = \frac{3 \cdot \alpha(T) \cdot K(T) \cdot V^{\mathrm{mol}}(T)}{C_p^{\mathrm{mol}}(T)}. \tag{4.8}$$

For the calculation of $\gamma_{\mathrm{macro}}(T)$, published data of the coefficient of thermal expansion $\alpha(T)$, the bulk modulus $K(T)$, the molar volume $V^{\mathrm{mol}}(T)$, and the molar heat capacity $C_p^{\mathrm{mol}}(T)$ were available up to 100 K [50, 168, 169, 174]. The resulting temperature dependence of γ_{macro} is shown in Fig. 4.15.

Each of the contributing quantities is temperature dependent having strong anomalies close to T_{C}. The dominating contribution to γ_{macro} (T) is that of the coefficient of thermal expansion $\alpha(T)$. It is close to zero and varies by about one order of magnitude in the temperature range between 0 and 30 K.[4]

If the phase transition is suppressed by a magnetic field, thermal expansion and heat capacity do not show distinct anomalies around 30 K and vary only mildly. As a result, also the anomalies in γ_{macro} (T) should vanish. However, the published

[4]The temperature dependence of α is in reasonable agreement in different sources of literature [44, 169, 195].

thermodynamical data in the field polarized state are incomplete and the Grüneisen parameter could not be calculated quantitatively for a comparison with the zero field model.

Upon approaching T_C from low temperatures, Eq. (4.8) yields large negative values of approximately -15. Slightly above the transition there is a pronounced dip-hump structure with the minimum at 30 K, the maximum at 35 K and a sign change in between. Upon further increasing the temperature, $\gamma_{\mathrm{macro}}(T)$ asymptotically approaches the constant value of 2.5 from above. Therefore, γ_{macro} was set to 2.5 above 100 K, because not all quantities entering Eq. (4.8) were available up to room temperature.

In MnSi magnetostrictive effects contribute to the anomalies of $\gamma_{\mathrm{macro}}(T)$ around T_C, and relatively large values even at elevated temperatures are to be expected. For instance, the magnetic contributions to $\alpha(T)$ play an important role up to at least 200 K and are of the same order of magnitude as the non-magnetic ones [195]. At low temperatures magnetic order drives $\alpha(T)$ even negative, i.e. the lattice expands upon cooling, and leads to the strong dip of $\gamma_{\mathrm{macro}}(T)$ around T_C [168, 169, 195].

It is not the purpose of this study to systematically disentangle the various contributions to $\gamma_{\mathrm{macro}}(T)$ or to determine their respective weight. Rather, we wish to find out to which extent $\Delta_i^{(1)}(T)$ can be understood in terms of bulk properties and where microscopic effects can be pinned down. We first calculate $\Delta_i^{(1)}(T)$ using Eq. (4.7). For constant γ_i, Eq. (4.7) can be integrated [187] yielding an expression for the frequency shift $\Delta_i^{(1)}(T)$ of phonon i,

$$\Delta_i^{(1)}(T) = \omega_i(0) \left\{ \exp\left[-3\gamma_i \int_0^T \alpha(T')dT' \right] - 1 \right\}. \tag{4.9}$$

The phonon frequency $\omega_i(0)$ is the only free parameter which can be determined for each branch i by a fit to the high-temperature data. The temperature dependences of $\omega_{\mathrm{ph},i}(T)$ according to Eq. (4.9) are plotted as orange lines in Figs. 4.12 and 4.13. At temperatures above 100 K the frequency changes of the Raman phonons are well described by $\Delta_i^{(1)}(T)$ with a constant Grüneisen parameter $\gamma_i = 2.5$ in good agreement with the asymptotic limit of $\gamma_{\mathrm{macro}}(T)$. At lower temperatures, γ_{macro} is not constant any further. Approaching the phase transition from above, the phonon frequencies may increase slightly as does $\gamma_{\mathrm{macro}}(T)$ (cf. Fig. 4.15). Similarly, the experimentally observed dip at $30\,\mathrm{K} > T_C$ has a corresponding anomaly in $\gamma_{\mathrm{macro}}(T)$. At T_C all phonon frequencies jump back to the value at $T > 30$ K and then soften again. The phonon

anomaly at T_C is unparalleled in any of the macroscopic quantities. While the $T_2^{(314)}$ phonon seems to stay at lower frequency, the other phonons reach frequencies above $\omega_i(0)$. The prediction according to Eq. (4.9) shows only a tiny kink which originates from $\alpha(T)$ (since all other quantities in Eq. (4.9) are constant). For $T \to 0$, $\Delta_i^{(1)}(T)$ vanishes as $\int \alpha \, dT'$ in the exponent goes to zero.

To summarize this part, we find that the widths of the four strongest phonons can be well understood in terms of symmetric anharmonic decay in the entire temperature range studied. The phonon energies are compatible with the thermodynamic properties in the temperature range above 50–100 K. More specifically, constant and mode-independent Grüneisen parameters γ_i which, additionally, coincide here with γ_{macro} are sufficient. Below 50–70 K, γ_{macro} increases towards a maximum at 35 K (see Fig. 4.15). A similar maximum may be present for the $T_2^{(197)}$ phonon [Fig. 4.13 (d)]. As to the other three lines the experimental accuracy is insufficient to resolve deviations from the simple expectation on the basis of constant γ_i parameters. While the anomaly at 30 K right above T_C is still clearly visibly in the temperature dependence of both γ_{macro} and the phonon frequencies we find phonon anomalies without a corresponding anomaly in the bulk right at T_C in contrast to what is found in insulating magnets [196–198]. The results with applied field demonstrate that there are no phonon anomalies without short or long ranged chiral order.

In order to disentangle thermodynamic and microscopic properties we insert γ_{macro} in Eq. (4.9) and recalculate $\Delta_i^{(1)}(T)$. This is motivated by the proximity of the anomalies in the phonon energies $\omega_{\mathrm{ph},i}(T)$ and of $\gamma_{\mathrm{macro}}(T)$ but cannot be justified mathematically since Eq. (4.7) yields Eq. (4.9) only for a constant γ_i. As shown in Fig. 4.13 the shift obtained in this way (dashed magenta lines) is identical to that for $\gamma_i = 2.5$ (orange lines) down to approximately 50 K but deviates below. The anomaly of $\omega_{\mathrm{ph},i}(T)$ observed right above T_C has now a correspondence in the prediction while that at T_C cannot be reproduced. Similar results are found for E symmetry but are not plotted to avoid overloading Fig. 4.12.

The interrelation of microscopic and thermodynamic properties can also be visualized by looking at the difference between the experimental frequencies $\omega_{\mathrm{ph},i}(T)$ and those calculated on the basis of Eq. (4.9) using $\gamma_{\mathrm{macro}}(T)$. As demonstrated in Fig. 4.16, the anomaly above T_C vanishes almost completely (with small phonon-specific variations) while that at T_C is rather pronounced. Although the use of $\gamma_{\mathrm{macro}}(T)$ in Eq. (4.9) is sloppy, it is safe to conclude that the anomaly in the fluc-

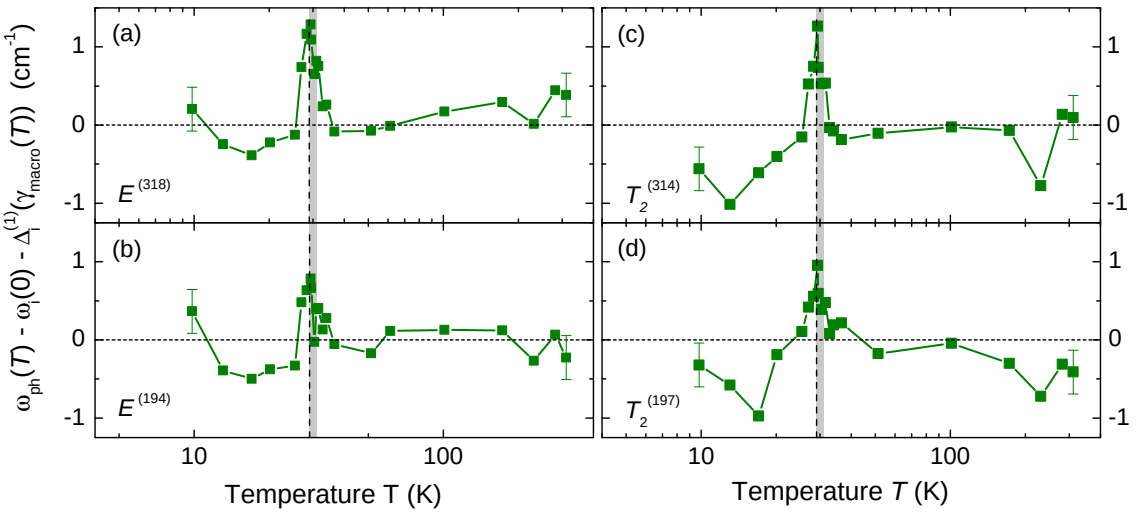

Figure 4.16: Difference of the experimental phonon energies $\omega_{\mathrm{ph}}(T)$ and those calculated via Eq. (4.5) and (4.9) using $\gamma_{\mathrm{macro}}(T)$. Note the logarithmic temperature scale. The anomalies above T_{C} vanish almost completely while those at T_{C} have no correspondence in the thermodynamical properties.

tuation disordered regime has a correspondence in the macroscopic properties while that at T_{C} is of microscopic origin. In this way the temperature dependence indicates that the phonons and $\gamma_{\mathrm{macro}}(T)$ react differently to the formation of helimagnetic order whereas the thermodynamic properties and the phonons are similarly affected by the fluctuations. The discrepancies between microscopic and macroscopic properties are largest at T_{C} (Fig. 4.16). However, they are significant also below. We recall that the Grüneisen parameter turns negative right above T_{C} meaning that the phonon frequencies anomalously increase along with the volume. In the case of MnSi this anomaly in γ_{macro} can be traced back to the thermal expansion [182, 195]. The strong discrepancies between microscopic and macroscopic properties highlight that the global volume changes observed around T_{C} are insufficient to explain the phonon anomalies. Rather, there are interactions that leave a much stronger imprint on the phonons studied here than on the overall bulk properties. In fact, Fawcett *et al.* [44, 199] found large magnetic contributions in studies of the specific heat and the elastic properties below T_{C} which they interpreted in terms of a magnetic Grüneisen parameter γ_{mag}. The authors found a γ_{mag} as large as -45 and constant in a temperature range from 14 to 32 K except for significant deviations very near to T_{C}. Also Pfleiderer and coworkers argue that there is a sizable anomalous contribution to the thermal expansion beyond the conventional T^2 variation [182].

In contrast to the itinerant helimagnet MnSi studied here the understanding of the spin-phonon interaction in insulating magnets is much more advanced as shown in various publications [196–198]. There, the temperature dependence of the phonon energies can be readily described by the mean-field-like variation of the macroscopic magnetization. A similar proportionality may be compatible with the data of the $T_2^{(314)}$ line [Fig. 4.13 (c)] below T_C but not for any of the other lines. The anomalies found in the fluctuation range ($T_C < T < 32\,\mathrm{K}$) cannot be explained in this scenario. Similarly, the non-monotonic variation of the phonons $E^{(194)}$, $T_2^{(197)}$, and $E^{(318)}$ need further attention in the low-temperature limit. We conclude that the four phonon lines studied here exhibit unexpected features in the fluctuation range right above T_C at the phase transition and in the ordered state below T_C which do not have a correspondence in Heisenberg-type magnets.

4.5.2 Carrier properties

For the normal state, Opel and coworkers demonstrated that the relaxation or memory function approach proposed by Götze and Wölfle theoretically [200] and worked out for IR spectroscopy by Allen and Mikkelsen [180] can be adapted to facilitate the derivation of lifetimes $\tau_{\gamma\gamma}(\omega, T)$ or scattering rates $\Gamma_{\gamma\gamma} = 1/\tau_{\gamma\gamma}$ and mass enhancement factors $1 + \lambda_{\gamma\gamma}(\omega, T) = m^*_{\gamma\gamma}(\omega, T)/m_b$ from the electronic Raman continuum (see Fig. 4.11) [81]. Here, m_b is the band mass, and $m^*_{\gamma\gamma}$ the effective mass as derived from Raman scattering. Opel *et al.* showed in particular that absolute numbers for all quantities can be obtained. In the context here, γ is short hand for $\gamma(\mathbf{k})$ and represents the Raman vertex which projects out symmetry dependent parts of the Brillouin zone. For simplicity and in order to avoid confusion with the Grüneisen parameters, we label the derived quantities by the symmetry projection $\mu = A_1$, E, T_1, T_2 rather than the vertex γ.

For the analysis of the electronic part we use symmetry-resolved spectra such as those shown in Fig. 4.11. There, one realizes that the continuum in $\mu = T_1$ symmetry is approximately as strong as those in the other symmetries. This is unusual, since in the non-resonant Raman response, T_1 contributions are expected to be absent in non-magnetic metallic systems and are usually found to be weak [201]. Excitations of T_1 symmetry (similarly as A_{2g} excitations in tetragonal systems) correspond to anti-symmetric off-diagonal elements in the Raman tensor α which occur whenever the off-diagonal elements are not equal, $\alpha_{i,j} \neq \alpha_{j,i}$. Here, the origin of the T_1 continuum

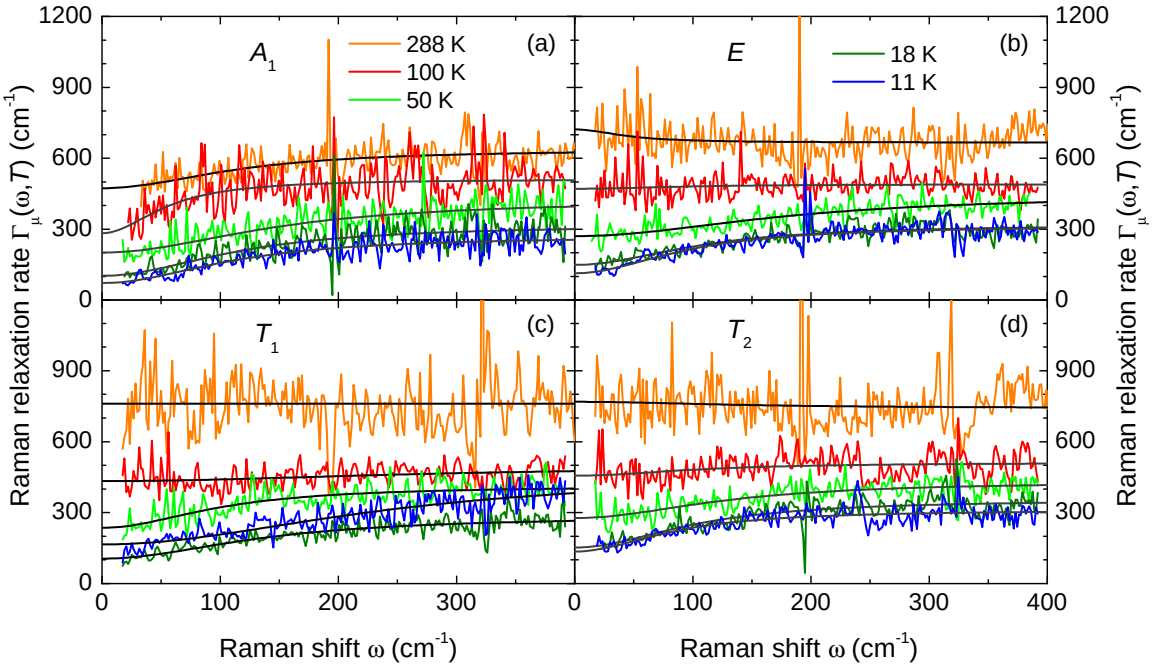

Figure 4.17: Temperature and symmetry dependence of the relaxation rates $\Gamma_\mu(\omega, T)$. The rates were obtained from the electronic continua as shown in Fig. 4.11. To calculate $\Gamma_\mu(\omega, T)$ the procedure described by Opel and coworkers [81] was used. The smooth lines are phenomenological fits to the data according to Eq. (4.11).

cannot be identified unambiguously as discussed in Sec. 2.1.4. Nonetheless, we show the results of the memory function analysis, that remains valid for all energy dependent relaxational processes, we can discuss possible implications of the T_1 response only on a preliminary level.

Fig. 4.17 shows the dynamical relaxation rates $\Gamma_\mu(\omega, T)$ derived from the energy dependent response $R\chi''_\mu(\omega, T)$ (Fig. 4.11) as described by Opel *et al.* [81]. They have similar temperature dependences at high energies for all symmetries but exhibit substantial differences close to zero energy. While Γ_{T1}, and Γ_{T2} become rather flat at room temperature, Γ_{A1} dips down at low energy thus reducing the overall temperature dependence between 13 and 288 K. In contrast, $\Gamma_E(288\,\mathrm{K})$ increases slightly towards low energy. The rates reflect the variation of the raw data (Fig. 4.11) but, owing to the derivation procedure [81], show some features in a more pronounced fashion such as the low-energy variation with temperature.

The dynamical mass renormalization factors $1 + \lambda_\mu(\omega, T)$ can be derived from $R\chi''_\mu(\omega, T)$ in the same way. Thus, it is expected that $1+\lambda_\mu(\omega, T)$ similarly emphasizes the variations close to zero energy. In fact, Fig. 4.18 (b) shows an anomaly of $1 +$

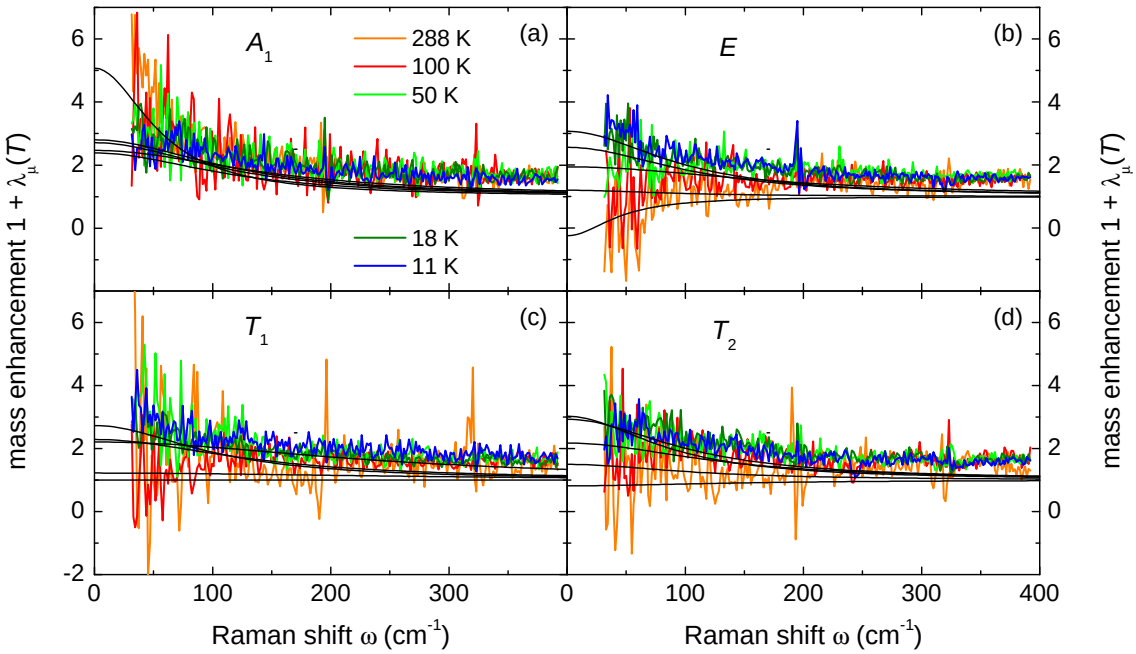

Figure 4.18: Temperature and symmetry dependence of the optical masses $1 + \lambda_\mu(T)$ obtained via the same formalism as the relaxation rates. The smooth lines are derived from the fits to the relaxation rates via Kramers-Kronig transformation, hence obey causality (see text). They are in reasonable agreement to the data except for a constant offset.

$\lambda_E(\omega, T)$ at 288 K. While all other masses increase monotonically with decreasing energy (other panels of Fig. 4.18), as typically expected for metals, $1 + \lambda_E(\omega, 288\,\mathrm{K})$ is reduced and even becomes negative at low energies. On the high energy side the renormalized masses saturate between 1 and 2 as expected. For the A_1, T_1, and T_2 symmetries the masses decay monotonically with increasing frequency. In the zero-energy limit they reach temperature dependent values between 0.8 (T_2) and 5 (A_1).

The dynamical carrier properties found here with inelastic light scattering are in overall agreement with those derived from the IR reflectivity [51] presented in Sec. 4.3. While the magnitudes and temperature dependences of $\Gamma_\mu(\omega, T)$ and $1 + \lambda_\mu(\omega, T)$ are similar below 100 K for both methods, there are important differences which may lead to new insights: (i) In contrast to the IR results, the masses found here are above unity (except for the E symmetry channel below 100 K) indicating the existence of interactions at all temperatures and energies. (ii) The symmetry dependence is significant. This is a unique feature of inelastic light scattering and indicates the

existence of anisotropies in the Brillouin zone which cannot be derived from the optical conductivity.

While the results in the A_1 and T_2 symmetries are compatible with metallic behaviour at all temperatures the E spectra deviate remarkably from what one expects for a metal. The deviation is seen best in the dynamics of the mass at 288 K which varies non-monotonically. At room temperature this observation is paralleled by the IR results [51] as summarized in Sec. 4.3.

As to the interpretation, the relaxation rates are more intuitive. The increase towards zero energy indicates either a new relaxation channel or pseudogap-like behaviour at higher temperatures. Similar anomalies have in fact been observed in organic conductors [202] and cuprates [203]. For heavy Fermion systems this type of temperature dependence can be explained in terms of a Kondo-like interaction [204]. However, it is unusual that the anomaly appears here at high temperature and vanishes below 100 K. Obviously, at least parts of the Fermi surface exhibit insulating behaviour at higher temperature. Whether or not this can be observed in ordinary transport remains open at the moment since there is no data available at elevated temperature. In addition, the metallic parts could short circuit the insulating ones in a similar fashion as in the cuprates [205]. We note that a vanishing or even negative mass [Fig. 4.18 (b)] can also result from multiband effects which, however, need to be studied numerically on the basis of a realistic band structure.

Fermi surfaces and Raman selection rules

For a preliminary understanding of the selection rules in MnSi we look at the Fermi surfaces as derived from band structure calculations [53]. However, as opposed to the cuprates [57, 66] or the iron-based compounds [201, 206], it is much more difficult in MnSi to directly map the symmetries on separate bands or regions in the Brillouin zone since the Fermi surface is more complicated.

Fig. 4.19 shows the results of Jeong and Pickett [53] which were obtained without spin-orbit coupling[5]. The spin majority and minority bands cannot be distinguished by electronic Raman scattering. In addition to the Fermi surfaces around high symmetry positions Γ $(0, 0, 0)$ and R (π, π, π), there are four other Fermi surfaces of similar shapes that resemble three tubes intersecting around the Γ point [53]. From

[5]Since spin-orbit coupling effects are expected to be small for Mn [53] they are unlikely to have an effect on the symmetry-based arguments that will be used to interpret the Raman results.

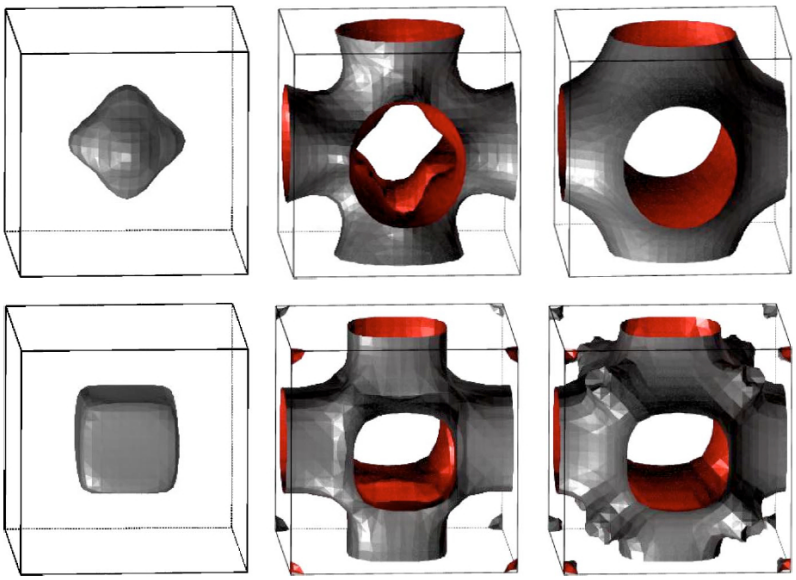

Figure 4.19: Fermi surfaces in MnSi. Majority (top row) and minority spin (bottom row) Fermi surfaces for a fixed magnetic moment equal to the experimental value of $0.4\,\mu_B$/Mn. From [53].

the shape of the Fermi surfaces a tentative relationship between momentum space and the carrier properties can be established. According to the lowest order Brillouin zone harmonics for cubic crystals [207], carriers on the Fermi surfaces around the Γ- and R-point may be projected out predominantly in A_1 symmetry. In addition, the lowest order non-trivial A_1 vertex $\gamma_{A1}^{(1)} = \cos k_x + \cos k_y + \cos k_z$ has its nodes very close to the big tubular Fermi surfaces. Fig. 4.20 shows the surface where the Raman vertex vanishes, $\gamma_{A1}^{(1)} = 0$, and thus the sensitivity of the experiment is zero. Electrons close to the big tubular Fermi surfaces should not contribute to A_1, but predominantly to the spectra of the orthogonal symmetries E and T_2. The E spectra are dominated by the necks around the X points $(\pi, 0, 0)$ and the T_2 spectra are more sensitive in the centers of the octants. More detailed information about the projections may be obtained in the effective mass approximation (cf. Sec. 2.1.3) where the band curvatures yield the Raman vertex, i.e. the sensitivities, in the non-resonant case [57, 206]. In MnSi the method is hard to apply, as the band structure is much more complicated than in the rare-earth tritellurides (cf. Sec. 3.4.6) and the Raman response is less symmetry selective.

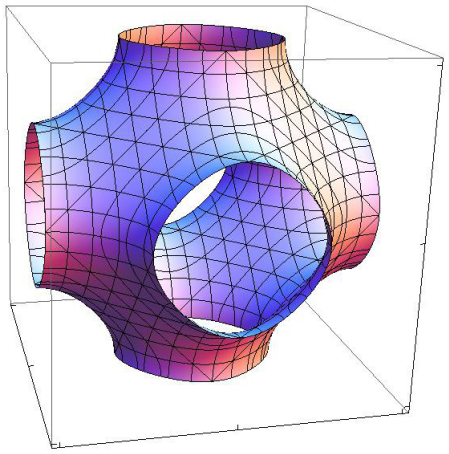

Figure 4.20: Nodes of the lowest order A_1 Raman vertex. Plotted is the hyper-surface in a cubic Brillouin zone, where the lowest order Raman vertex $\gamma_{A1}^{(1)}$ vanishes and thus the Raman experiment is insensitive. Electrons close to this part of the Brillouin zone are not projected out in the A_1 spectra. Note the resemblance to large parts of the Fermi surfaces shown in Fig. 4.19

Static relaxation rates

We now focus on the static (DC) limit. To reliably extract the zero-energy extrapolation values of $\Gamma_\mu(\omega \to 0, T)$ and $1+\lambda_\mu(\omega \to 0, T)$ from the relatively noisy Raman data (Fig. 4.11) we use phenomenological functions having the correct analytical behaviour in the limits $\omega \to 0$ and $\omega \to \infty$: (i) $\Gamma_\mu(\omega, T)$ (as opposed to the imaginary part of the single particle self energy Σ'') is a symmetric function, $\Gamma_\mu(-\omega, T) = \Gamma_\mu(\omega, T)$, (ii) $\lambda_\mu(\omega \to 0, T > 0)$ is finite and symmetric, and (iii) $\Gamma_\mu(\omega, T)$ saturates at high energy. The latter condition is a restriction in the spirit of the Mott-Joffe-Regel limit [208, 209] that applies when the quasi-particle mean free path at high temperature becomes progressively shorter and finally comparable to the lattice constant. As phonons are the dominant scatterers in metals at high temperatures, the mean free path cannot decrease further and the resistivity saturates. In the case of two-particle response functions there are contributions to the carrier response beyond the mean free path, and general statements as to the high-energy behaviour become impossible [210]. Since all of the relaxation rates derived here saturate, the introduction of a temperature dependent limiting value $\Gamma_\mu^{\max}(T)$ is justified experimentally but is not well supported theoretically.

On this basis, the minimal model is the parallel-resistor formalism with a quadratic

energy dependence at $\omega \to 0$ [211],

$$\frac{1}{\Gamma_\mu(\omega,T)} = \frac{1}{\Gamma^*_\mu(\omega,T)} + \frac{1}{\Gamma^{\max}_\mu(T)}. \tag{4.10}$$

where $\Gamma^*_\mu(\omega,T) = c(T)+a(T)\omega^2$ dominates at low frequencies while $\Gamma^{\max}_\mu(T)$ describes the high energy part. Inversion yields

$$\Gamma_\mu(\omega,T) = \frac{[c(T)+a(T)\omega^2]\cdot\Gamma^{\max}_\mu(T)}{c(T)+a(T)\omega^2+\Gamma^{\max}_\mu(T)}, \tag{4.11}$$

with the zero frequency limit $\Gamma_\mu(0,T)$ given by

$$\Gamma_\mu(0,T) = \frac{c(T)\Gamma^{\max}_\mu(T)}{c(T)+\Gamma^{\max}_\mu(T)}. \tag{4.12}$$

The fits to the relaxation rates $\Gamma_\mu(\omega,T)$ according to Eq. (4.11) are shown in Fig. 4.17. As expected, the $\omega \to 0$ extrapolation [Eq. (4.12)] depends on both the high frequency limit $\Gamma^{\max}_\mu(T)$ and the offset $c(T)$. Each point in Fig. 4.21 is obtained from Eq. (4.12) with the parameters found in the $\Gamma_\mu(\omega,T)$ fits.

In Fig. 4.21, the static Raman relaxation rates $\Gamma_\mu(0,T)$ are compared with conventional transport $\rho(T)$. In a Drude model, the resistivity is related to the carrier relaxation rate $\Gamma_\rho(T) = \hbar/\tau(T)$ via the plasma frequency ω_{pl} as $\Gamma_\rho(T) = \epsilon_0\,\omega^2_{\mathrm{pl}}\,\rho(T)$. Here, ϵ_0 is the vacuum permeability and $\omega_{\mathrm{pl}} = 2.3\,\mathrm{eV}$ [51]. To match the Raman $\Gamma_\mu(\omega=0,T)$ and the resistivity $\Gamma_\rho(T)$ above T_{C} (cf. Fig. 4.21), an additional factor of 0.73 was introduced. A factor smaller than one can be explained by the frequency cutoff at $400\,\mathrm{cm}^{-1}$ in the relaxation rate analysis (Fig. 4.17). In any case, it cannot be expected that the relaxation rates obtained from the light scattering experiment and from transport coincide completely since the higher order corrections to the respective response are different and in the ten percent range [81, 213]. The experimental error of about $\pm 30\,\mathrm{cm}^{-1}$ was estimated from the scatter of neighboring points in Fig. 4.21 and the error of the DC extrapolation of $\Gamma_\mu(\omega,T)$ plotted in Fig. 4.17.

The A_1 relaxation rates are significantly smaller than those in the other symmetries and also below the results from transport, at least for $T > T_{\mathrm{C}}$ (Fig. 4.21). This can either be an effect of screening [57] or, more likely, of the selectivity of the A_1 Raman vertex. As described above, the A_1 vertex blacks out the big tubular Fermi surfaces that, however, seem to be relevant for transport.

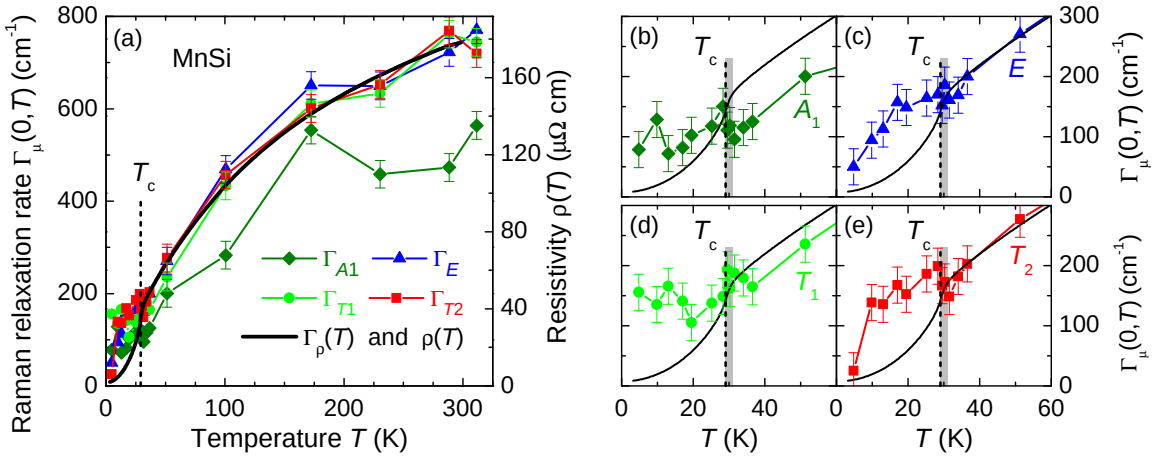

Figure 4.21: Static Raman relaxation rates and transport data. Panel (a) shows the Raman relaxation rates $\Gamma_\mu(\omega = 0, T)$ (points, left axis) as a function of symmetry μ as derived from $\Gamma_\mu(\omega, T)$ (see text). If the longitudinal DC resistivity $\rho(T)$ (black line, right axis) [212] is converted into a relaxation rate $\Gamma_\rho(T)$ using a Drude model with the experimental plasma frequency $\omega_{\mathrm{pl}} = 2.3\,\mathrm{eV}$ [51], an extra factor of 0.73 is needed to match transport and Raman data. Above T_C (dashed vertical line) the Raman data in E, T_1 and T_2 symmetry agree with $\rho(T)$, while the data in A_1 symmetry do not. (b)-(e) Zoom in on low temperatures. The phase transition has only a minor effect on $\Gamma_\mu(\omega = 0, T)$. Above T_C close to the fluctuation disordered regime (shaded), there may be a dip in A_1 and T_2 symmetry. Below the phase transition $\Gamma_\mu(\omega = 0, T)$ decreases slower than $\Gamma_\rho(T)$.

Similar to what is observed in IR experiments (cf. Sec. 4.3), the Raman DC relaxation rates in the helical state, stay well above the transport data and decrease at a lower rate for all symmetries (Fig. 4.21). The A_1 and T_1 Raman relaxation rates even saturate at a finite value for $T \to 0$, while E and T_2 finally approach the values expected from transport. The observation of this decrease makes it unlikely that the saturation observed in the A_1 and T_1 channel and in IR [51] is an artifact resulting from the rather small relaxation rates, and we conclude that the discrepancies between IR, transport, and Raman scattering in the ordered state need to be taken seriously. More specifically, the convex and the concave T^2-like behaviour found in Raman and, respectively, in ordinary transport seem to be two sides of the same coin which need to be explained theoretically.

The significance of the observations at low temperature is confirmed by the agreement of all three experimental methods above T_C (Figs. 4.6 and 4.21). The Raman data points of $\Gamma_\mu(0, T)$ in $\mu = E$, T_1 and T_2 symmetry agree with $\Gamma_\rho(T)$ in the temperature range from 310 to 30 K. It is remarkable that also the relaxation rates in

T_1 symmetry follow the DC resistivity curve at high temperatures. Provided that T_1 in fact projects chiral excitations one can argue that they continue to be present above the helimagnetic phase, as the crystal structure lacks inversion symmetry also in the high temperature phase. Thus, chiral excitations can be created with inelastic photon scattering even up to room temperature as anticipated in thermal expansion experiments [195]. However, as discussed in Sec. 2.1.4, a final interpretation of the T_1 data is premature.

Right above T_C in the fluctuation disordered regime, the DC relaxation rates dip down in T_2 and maybe in A_1 symmetry [Figs. 4.21 (e) and (b)]. Note that this goes along with the dip in the phonon frequencies (Figs. 4.12 and 4.13). The simultaneous observation of the anomaly in the phonon energy and in the electronic continuum at the same temperature makes us confident that the effect is significant. While the phonon softening is also observed independently in the thermal expansion, the non-monotonic variation in the carrier relaxation is a new observation underpinning the impact of the phase transition and the preceding fluctuations on the electrons. Obviously both effects are not very symmetry selective, meaning that extended parts of the Fermi surface are involved or, in other words, that the anomalies are not dominated by a single vector in momentum space. For instance, if the helices would immediately align along the $\langle 111 \rangle$ direction one would expect a strong effect in T_2 symmetry being most sensitive in the center of the octants. The weak symmetry dependence right above T_C, could in fact be a consequence of isotropic fluctuations and thus supports the Brazovskii scenario proposed by Janoschek *et al.* [48].

The detailed analysis below 40 K clearly reveals unexpected interactions between spin, charge, and lattice at the phase transition. Progress in this still speculative discussion is probably only possible if the data are analyzed with a phenomenological model and on the basis of a realistic band structure. It remains a future project to study, i.e. the Raman response of skyrmions which was up to now elusive. In addition, the momentum dependence of the relaxation rates in connection with anomalous transport properties such as the topological Hall signal remains to be explored.

Chapter 5

Summary

This thesis reports inelastic light scattering results on the impact of charge and spin ordering on lattice and carrier excitations in metallic compounds. Phases with complex order, such as incommensurate charge density wave (CDW) order in the rare-earth tritellurides and itinerant helimagnetism in MnSi, were studied as a function of temperature, magnetic field and chemical- as well as applied-pressure. In both cases, the instability in the electronic system is closely related to the lattice properties motivating a study of their interplay. Using Raman scattering, phonons as well as electronic excitations, including collective modes and fluctuations, can be probed. The polarization selection rules facilitate a classification of the symmetry of excitations and provide some momentum resolution for the study of anisotropies in the electronic system.

A major part of the work was devoted to the setup of the experiment resulting in a substantially higher sensitivity that finally allowed the study of materials with low scattering cross section in a diamond anvil pressure cell and in applied magnetic fields at low temperature. The central part was an optimized high-aperture optical system collecting the scattered photons. The separation of the paths of incoming and scattered light in combination with spatial filters enabled the discrimination between Raman light and parasitic background. These efforts facilitated the detection of signals as small as 0.05 photon counts per second and milli-watt laser power for a given spectral resolution of $2\,\mathrm{cm}^{-1}$ under extreme external conditions. The improved high pressure diamond anvil cell could be loaded with helium as the most isotropic pressure transmission medium. In addition, the cell was equipped with a coil system to measure the ac magnetic susceptibility in, for instance, superconducting samples.

In several rare-earth tritellurides $R\mathrm{Te}_3$ (R = La, Ce, Dy, Ho, Er), the gap in the

electronic Raman spectrum, the amplitude modes (AM), and the charge fluctuations above the charge density wave (CDW) transition were directly observed. The AMs were used as a probe to map out the phase diagram of $ErTe_3$ as a function of temperature and pressure. The CDW order can be suppressed gradually until it vanishes down to the lowest temperatures for pressure values in excess of 2.5 GPa. At ambient pressure, the temperature dependence of the AMs close to the maximal transition temperature T_{CDW1} deviates in a systematic yet unexplained fashion from the expected form in all compounds. In addition, the low temperature saturation value of the AM frequency exceeds the value expected from the high-temperature part. The behaviour can be explained by a two-step transition, one at T_{CDW1} and another one close to $2/3\,T_{\mathrm{CDW1}}$. For both transitions, the AM frequency depends linearly on the CDW condensate density at variance with the mean field predictions. Below T_{CDW2}, there is evidence for an AM associated with a second CDW that is oriented orthogonally to the first one and present only in the heavier $R\mathrm{Te}_3$ compounds. The two orthogonal AMs interact giving rise to a beat mode.

Fluctuations considerably suppress the CDW phase transition. The Raman results provide direct evidence for fluctuations with fourfold symmetry that can be described quantitatively by the the exchange of two charge fluctuations with opposite momenta. Hence, the rare-earth tritellurides are one of the few examples for a "stripe liquid" that may have broader implications also in other materials.

Out of the fluctuation regime, CDW order develops. However, the precise mechanism of CDW formation and, in particular, the selection of the ordering vector is under debate. The Raman results on charge fluctuations and the anisotropies of the CDW energy gap show, that lifted band degeneracies play a key role in selecting the ordering vector. Moreover, the Raman vertex efficiently focuses the sensitivity on these hot-spots. Two cooperating effects were identified: (i) The system is very susceptible to charge fluctuations close to lifted degeneracies and gains energy by gapping out these regions of the Fermi surface. (ii) The strong band curvatures in the vicinity of the lifted degeneracies result in a strongly enhanced electron phonon interaction making the system more susceptible to a deformation, fostering CDW formation. For small hybridization and an electron-phonon coupling strength of $\lambda > 0.5$, the combination of these two effects may even exceed the nesting contribution to CDW formation.

In MnSi, the phase transition from paramagnetism to helimagnetic order and its

impact on phonons as well as the electronic response were systematically studied. All optical phonons are detected, showing conventional behaviour above the helimagnetic transition, but pronounced anomalies close to and below T_C. Most remarkably, the phonon energies clearly dip down already above the phase transition. The minimum of the phonon frequency in the fluctuation regime is tracked by the Grüneisen parameter γ_{macro} that connects changes in frequency and volume via macroscopic thermodynamic properties. The temperature dependence at and below T_C has no correspondence in γ_{macro} and thus indicates that the phonons couple differently to the helical spin order and to macroscopic thermodynamic properties such as specific heat. However, there is no microscopic theory yet explaining the spin-phonon coupling in the helical state. In an applied magnetic field of 4 T, i.e., in the field polarized state, the phonon anomalies disappear which further supports a connection between the anomalies and helimagnetism.

With electronic Raman scattering, the frequency and temperature dependence of electron relaxation rates and the corresponding mass enhancement is studied. The magnitude and temperature dependence of the dynamical carrier properties are in overall agreement with those derived from infrared experiments. However, the Raman masses are generally above unity, indicating the existence of interactions at all temperatures and frequencies. Additionally, there is a significant symmetry dependence that corresponds to probing different regions of the Fermi surfaces. The dc Raman relaxation rates between room temperature and 50 K are in reasonable agreement with conventional transport and infrared (IR) spectroscopy in E, T_2 and also in T_1 symmetry which, in principle, is sensitive to chiral excitations. The relaxation rates in the A_1 channel deviate from those obtained by conventional transport and IR spectroscopy at all temperatures. This either results from screening effects or indicates that those parts of the Fermi surface, which are probed by A_1 symmetry, do not determine the temperature dependence of conventional transport. In the range of 2 K above T_C, the Raman relaxation rates show a narrow minimum highlighting the importance of fluctuations for the phase transition. In the helical phase, deviations from transport measurements are found, but cannot be explained theoretically yet. It is remarkable that below T_C also the IR results, analyzed in a standard Drude formalism, deviate from transport but agree with the Raman relaxation rates. As the differences only occur in the ordered state, but not above T_C, scattering of electrons from complex spin structures such as helices may provide an explanation.

Bibliography

[1] M. Vojta, *Quantum phase transitions*, Reports on Progress in Physics **66**, 2069 (2003).

[2] S. A. Kivelson, I. P. Bindloss, E. Fradkin, V. Oganesyan, J. M. Tranquada, A. Kapitulnik, and C. Howald, *How to detect fluctuating stripes in the high-temperature superconductors*, Rev. Mod. Phys. **75**, 1201 (2003).

[3] C. Pfleiderer, *Superconducting phases of f-electron compounds*, Rev. Mod. Phys. **81**, 1551 (2009).

[4] G. R. Stewart, *Superconductivity in iron compounds*, Rev. Mod. Phys. **83**, 1589 (2011).

[5] G. Grüner, in *Density Waves in Solids*, edited by D. Pines (Addison-Wesley, 1994).

[6] H. v. Löhneysen, A. Rosch, M. Vojta, and P. Wölfle, *Fermi-liquid instabilities at magnetic quantum phase transitions*, Rev. Mod. Phys. **79**, 1015 (2007).

[7] A. Ványolos, B. Dóra, and A. Virosztek, *Unconventional charge-density waves driven by electron-phonon coupling*, Phys. Rev. B **73**, 165127 (2006).

[8] W. L. McMillan, *Microscopic model of charge-density waves in 2H-$TaSe_2$*, Phys. Rev. B **16**, 643 (1977).

[9] C. M. Varma and A. L. Simons, *Strong-Coupling Theory of Charge-Density-Wave Transitions*, Phys. Rev. Lett. **51**, 138 (1983).

[10] H. Yao, J. A. Robertson, E.-A. Kim, and S. A. Kivelson, *Theory of stripes in quasi-two-dimensional rare-earth tellurides*, Phys. Rev. B **74**, 245126 (2006).

[11] T. Kiss, T. Yokoya, A. Chainani, S. Shin, T. Hanaguri, M. Nohara, and H. Takagi, *Charge-order-maximized momentum-dependent superconductivity*, Nat. Phys. **3**, 720 (2007).

[12] M. D. Johannes and I. I. Mazin, *Fermi surface nesting and the origin of charge density waves in metals*, Phys. Rev. B **77**, 165135 (2008).

[13] V. J. Emery, S. A. Kivelson, and H. Q. Lin, *Phase separation in the t - J model*, Phys. Rev. Lett. **64**, 475 (1990).

[14] M. Marder, N. Papanicolaou, and G. C. Psaltakis, *Phase separation in a t - J model*, Phys. Rev. B **41**, 6920 (1990).

[15] M. Grilli, R. Raimondi, C. Castellani, C. Di Castro, and G. Kotliar, *Superconductivity, phase separation, and charge-transfer instability in the $U = \infty$ limit of the three-band model of the CuO_2 planes*, Phys. Rev. Lett. **67**, 259 (1991).

[16] A. Perali, C. Castellani, C. Di Castro, and M. Grilli, *d-wave superconductivity near charge instabilities*, Phys. Rev. B **54**, 16216 (1996).

[17] P. A. Lee, T. M. Rice, and P. W. Anderson, *Conductivity from Charge or Spin Density Waves*, Solid State Communications **14**, 703 (1974).

[18] P. A. Lee, T. M. Rice, and P. W. Anderson, *Fluctuation Effects at a Peierls Transition*, Phys. Rev. Lett. **31**, 462 (1973).

[19] H.-M. Eiter, M. Lavagnini, R. Hackl, E. A. Nowadnick, A. F. Kemper, T. P. Devereaux, J.-H. Chu, J. G. Analytis, I. R. Fisher, and L. Degiorgi, *Alternative route to charge density wave formation in multiband systems*, Proc. Nat. Acad. Sci. U.S.A. **110**, 64 (2013).

[20] W. K. Lee, H. Z. Cummins, R. M. Pick, and C. Dreyfus, *Amplitude mode in* K_2SeO_4*: Temperature dependence of the Raman cross section*, Phys. Rev. B **37**, 6442 (1988).

[21] R. V. Yusupov, T. Mertelj, J.-H. Chu, I. R. Fisher, and D. Mihailovic, *Single-Particle and Collective Mode Couplings Associated with 1- and 2-Directional Electronic Ordering in Metallic* RTe_3 *(*$R =$ *Ho, Dy, Tb)*, Phys. Rev. Lett. **101**, 246402 (2008).

[22] T. Moriya, *Spin Fluctuations in Itinerant Electron Magnetism* (Springer, Berlin, Heidelberg, 1985).

[23] G. G. Lonzarich and L. Taillefer, *Effect of spin fluctuations on the magnetic equation of state of ferromagnetic or nearly ferromagnetic metals*, J. Phys. C **18**, 4339 (1985).

[24] L. D. Landau and E. M. Lifshitz, *Course of Theoretical Physics, Electrodynamics of Continuous Media* (Pergamon Press, New York, 1980), Vol. 8, p. Sec. 52.

[25] I. Dzyaloshinsky, *A thermodynamic theory of "weak" ferromagnetism of antiferromagnetics*, J. Phs. Chem. Solids **4**, 241 (1958).

[26] T. Moriya, *New Mechanism of Anisotropic Superexchange Interaction*, Phys. Rev. Lett. **4**, 228 (1960).

[27] T. Moriya, *Anisotropic Superexchange Interaction and Weak Ferromagnetism*, Phys. Rev. **120**, 91 (1960).

[28] S. V. Grigoriev, S. V. Maleyev, A. I. Okorokov, Y. O. Chetverikov, P. Böni, R. Georgii, D. Lamago, H. Eckerlebe, and K. Pranzas, *Magnetic structure of MnSi under an applied field probed by polarized small-angle neutron scattering*, Phys. Rev. B **74**, 214414 (2006).

[29] Y. Ishikawa, T. Komatsubara, and D. Bloch, *Magnetic phase diagram of MnSi*, Physica B+C **86–88**, 401 (1977).

[30] A. Bauer, A. Neubauer, C. Franz, W. Münzer, M. Garst, and C. Pfleiderer, *Quantum phase transitions in single-crystal* $Mn_{1-x}Fe_xSi$ *and* $Mn_{1-x}Co_xSi$*: Crystal growth, magnetization, ac susceptibility, and specific heat*, Phys. Rev. B **82**, 064404 (2010).

[31] C. Pfleiderer, D. Reznik, L. Pintschovius, H. v. Lohneysen, M. Garst, and A. Rosch, *Partial order in the non-Fermi-liquid phase of MnSi*, Nature **427**, 227 (2004).

[32] C. Pfleiderer, G. J. McMullan, S. R. Julian, and G. G. Lonzarich, *Magnetic quantum phase transition in MnSi under hydrostatic pressure*, Phys. Rev. B **55**, 8330 (1997).

[33] C. Pfleiderer, S. R. Julian, and G. G. Lonzarich, *Non-Fermi-liquid nature of the normal state of itinerant-electron ferromagnets*, Nature **414**, 427 (2001).

[34] C. Pfleiderer, P. Böni, T. Keller, U. K. Rößler, and A. Rosch, *Non-Fermi Liquid Metal Without Quantum Criticality*, Science **316**, 1871 (2007).

[35] Y. J. Uemura *et al.*, *Phase separation and suppression of critical dynamics at quantum phase transitions of MnSi and* $(Sr_{1-x}Ca_x)RuO_3$, Narture Physics **3**, 29 (2007).

[36] R. Ritz, M. Halder, M. Wagner, C. Franz, A. Bauer, and C. Pfleiderer, *Formation of a topological non-Fermi liquid in MnSi*, Nature (London) **497**, 231 (2013).

[37] A. Neubauer, C. Pfleiderer, B. Binz, A. Rosch, R. Ritz, P. G. Niklowitz, and P. Böni, *Topological Hall Effect in the A Phase of MnSi*, Phys. Rev. Lett. **102**, 186602 (2009).

[38] T. Schulz, R. Ritz, A. Bauer, M. Halder, M. Wagner, C. Franz, C. Pfleiderer, K. Everschor, M. Garst, and A. Rosch, *Emergent electrodynamics of skyrmions in a chiral magnet*, Nat. Phys. **8**, 301 (2012).

[39] S. Mühlbauer, B. Binz, F. Jonietz, C. Pfleiderer, A. Rosch, A. Neubauer, R. Georgii, and P. Böni, *Skyrmion Lattice in a Chiral Magnet*, Science **323**, 915 (2009).

[40] F. Jonietz, S. Mühlbauer, C. Pfleiderer, A. Neubauer, W. Münzer, A. Bauer, T. Adams, R. Georgii, P. Böni, R. A. Duine, K. Everschor, M. Garst, and A. Rosch, *Spin Transfer Torques in MnSi at Ultralow Current Densities*, Science **330**, 1648 (2010).

[41] J. Iwasaki, M. Mochizuki, and N. Nagaosa, *Current-induced skyrmion dynamics in constricted geometries*, Nature Nanotechnology **8**, 742 (2013).

[42] A. Fert, V. Cros, and J. Sampaio, *Skyrmions on the track*, Nature Nanotechnology **8**, 152 (2013).

[43] M. Mochizuki, X. Z. Yu, S. Seki, N. Kanazawa, W. Koshibae, J. Zang, M. Mostovoy, Y. Tokura, and N. Nagaosa, *Thermally driven ratchet motion of a skyrmion microcrystal and topological magnon Hall effect*, Nature Materials **13**, 241 (2014).

[44] E. Fawcett, J. P. Maita, and J. H. Wernick, *Magnetoelastic and Thermal Properties of MnSi*, lntern. J. Magnetism **1**, 29 (1970).

[45] Y. Ishikawa, Y. Noda, Y. J. Uemura, C. F. Majkrzak, and G. Shirane, *Paramagnetic spin fluctuations in the weak itinerant-electron ferromagnet MnSi*, Phys. Rev. B **31**, 5884 (1985).

[46] M. Date, K. Okuda, and K. Kadowaki, *Electron Spin Resonance in the Itinerant-Electron Helical Magnet MnSi*, J. Phys. Soc. Jpn. **42**, 1555 (1977).

[47] S. M. Stishov, A. E. Petrova, S. Khasanov, G. K. Panova, A. A. Shikov, J. C. Lashley, D. Wu, and T. A. Lograsso, *Magnetic phase transition in the itinerant helimagnet MnSi: Thermodynamic and transport properties*, Phys. Rev. B **76**, 052405 (2007).

[48] M. Janoschek, M. Garst, A. Bauer, P. Krautscheid, R. Georgii, P. Böni, and C. Pfleiderer, *Fluctuation-induced first-order phase transition in Dzyaloshinskii-Moriya helimagnets*, Phys. Rev. B **87**, 134407 (2013).

[49] S. A. Brazovskii, *Phase transition of an isotropic system to a nonuniform state*, Sov. Phys. JETP **41**, 85 (1975).

[50] A. Bauer, M. Garst, and C. Pfleiderer, *Specific Heat of the Skyrmion Lattice Phase and Field-Induced Tricritical Point in MnSi*, Phys. Rev. Lett. **110**, 177207 (2013).

[51] F. P. Mena, D. van der Marel, A. Damascelli, M. Fäth, A. A. Menovsky, and J. A. Mydosh, *Heavy carriers and non-Drude optical conductivity in MnSi*, Phys. Rev. B **67**, 241101 (2003).

[52] D. van der Marel, *Anisotropy of the optical conductivity of high-T_c cuprates*, Phys. Rev. B **60**, R765 (1999).

[53] T. Jeong and W. E. Pickett, *Implications of the B20 crystal structure for the magnetoelectronic structure of MnSi*, Phys. Rev. B **70**, 075114 (2004).

[54] D. Belitz, T. R. Kirkpatrick, and A. Rosch, *Theory of helimagnons in itinerant quantum systems. II. Nonanalytic corrections to Fermi-liquid behavior*, Phys. Rev. B **74**, 024409 (2006).

[55] F. Freimuth, R. Bamler, Y. Mokrousov, and A. Rosch, *Phase-space Berry phases in chiral magnets: Dzyaloshinskii-Moriya interaction and the charge of skyrmions*, Phys. Rev. B **88**, 214409 (2013).

[56] C. Franz, F. Freimuth, A. Bauer, R. Ritz, C. Schnarr, C. Duvinage, T. Adams, S. Blügel, A. Rosch, Y. Mokrousov, and C. Pfleiderer, *Real-Space and Reciprocal-Space Berry Phases in the Hall Effect of $Mn_{1-x}Fe_xSi$*, Phys. Rev. Lett. **112**, 186601 (2014).

[57] T. P. Devereaux and R. Hackl, *Inelastic light scattering from correlated electrons*, Rev. Mod. Phys. **79**, 175 (2007).

[58] S. Caprara, C. Di Castro, M. Grilli, and D. Suppa, *Charge-Fluctuation Contribution to the Raman Response in Superconducting Cuprates*, Phys. Rev. Lett. **95**, 117004 (2005).

[59] S. Caprara, C. Di Castro, B. Muschler, W. Prestel, R. Hackl, M. Lambacher, A. Erb, S. Komiya, Y. Ando, and M. Grilli, *Extracting the dynamical effective interaction and competing order from an analysis of Raman spectra of the high-temperature $La_{2-x}Sr_xCuO_4$ superconductor*, Phys. Rev. B **84**, 054508 (2011).

[60] M. V. Klein and S. B. Dierker, *Theory of Raman scattering in superconductors*, Phys. Rev. B **29**, 4976 (1984).

[61] G. Abstreiter, M. Cardona, and A. Pinczuk, in *Light Scattering in Solids IV*, Vol. 54 of *Topics in Applied Physics*, edited by M. Cardona and G. Güntherodt (Springer Berlin Heidelberg, 1984), pp. 5–150.

[62] G. Turrell, *Infrared and Raman Spectra of Crystals* (Academic Press, London and New York, 1972).

[63] A.-M. Racu, D. Menzel, J. Schoenes, and K. Doll, *Crystallographic disorder and electron-phonon coupling in $Fe_{1-x}Co_xSi$ single crystals: Raman spectroscopy study*, Phys. Rev. B **76**, 115103 (2007).

[64] H.-M. Eiter, P. Jaschke, R. Hackl, A. Bauer, M. Gangl, and C. Pfleiderer, *Raman study of the temperature and magnetic field dependence of electronic and lattice properties in MnSi*, Phys. Rev. B **90**, 024411 (2014).

[65] W. Hayes and R. Loudon, *Scattering of Light by Crystals* (John Wiley and Sons, 1978).

[66] T. P. Devereaux, D. Einzel, B. Stadlober, R. Hackl, D. H. Leach, and J. J. Neumeier, *Electronic Raman scattering in high-T_c superconductors: A probe of $d_{x^2-y^2}$ pairing*, Phys. Rev. Lett. **72**, 396 (1994).

[67] H. B. Callen and T. A. Welton, *Irreversibility and Generalized Noise*, Phys. Rev. **83**, 34 (1951), fluctuation-dissipation theorem.

[68] L. D. Landau and E. M. Lifshitz, *Course of Theoretical Physics, Statistical Physics* (Pergamon Press, New York, 1980), Vol. 5.

[69] B. S. Shastry and B. I. Shraiman, *Theory of Raman scattering in Mott-Hubbard systems*, Phys. Rev. Lett. **65**, 1068 (1990).

[70] S. V. Grigoriev, N. M. Potapova, S.-A. Siegfried, V. A. Dyadkin, E. V. Moskvin, V. Dmitriev, D. Menzel, C. D. Dewhurst, D. Chernyshov, R. A. Sadykov, L. N. Fomicheva, and A. V. Tsvyashchenko, *Chiral Properties of Structure and Magnetism in $Mn_{1-x}Fe_xGe$ Compounds: When the Left and the Right are Fighting, Who Wins?*, Phys. Rev. Lett. **110**, 207201 (2013).

[71] D. Einzel and R. Hackl, *Electronic Raman Scattering in Copper Oxide Superconductors*, Journal of Raman Spectroscopy **27**, 307 (1996).

[72] F. Michaud, F. Vernay, and F. Mila, *Theory of inelastic light scattering in spin-1 systems: Resonant regimes and detection of quadrupolar order*, Phys. Rev. B **84**, 184424 (2011).

[73] P. E. Sulewski, P. A. Fleury, K. B. Lyons, and S.-W. Cheong, *Observation of chiral spin fluctuations in insulating planar cuprates*, Phys. Rev. Lett. **67**, 3864 (1991).

[74] R. Philipp, *Gap und Pseudogap in Kupratsupraleitern nahe der optimalen Dotierung*, Diplomarbeit, Technische Universität München (1998).

[75] W. Prestel, Ph.d. thesis, Technische Universität München, 2012.

[76] H.-M. Eiter, *Untersuchung von Ladungs- und Spinordnung in gering dotierten Kupraten: Eine Raman-Studie*, Diplomarbeit, Technische Universität München (2008).

[77] P. Jaschke, *Untersuchung der Gitter- und Ladungsträgerdynamik von MnSi in der Umgebung der magnetisch geordneten Phase*, Diplomarbeit, Technische Universität München (2012).

[78] A. Köhler, *Gedanken zu einem neuen Beleuchtungsverfahren für mikrophotographische Zwecke*, Zeitschrift für wissenschaftliche Mikroskopie (1893).

[79] A. F. Goncharov and V. V. Struzhkin, *Raman spectroscopy of metals, high-temperature superconductors and related materials under high pressure*, J. Raman Spectrosc. **34**, 532 (2003).

[80] B. Muschler, Ph.d. thesis, Technische Universität München, 2012.

[81] M. Opel, R. Nemetschek, C. Hoffmann, R. Philipp, P. F. Müller, R. Hackl, I. Tüttő, A. Erb, B. Revaz, E. Walker, H. Berger, and L. Forró, *Carrier relaxation, pseudogap, and superconducting gap in high-T_c cuprates: A Raman scattering study*, Phys. Rev. B **61**, 9752 (2000).

[82] R. Hackl, R. Kaiser, and S. Schicktanz, *Gap mode, superconducting gap and phonon mode in V_3Si and Nb_3Sn*, J. Phys. C **16**, 1729 (1983).

[83] R. Hackl, Ph.D. thesis, Technische Universität München, 1987.

[84] J. F. Ready, *Effects of high power laser radiation* (Academic Press, New York, 1971).

[85] W. H. Fietz, R. Quenzel, H. A. Ludwig, K. Grube, S. I. Schlachter, F. W. Hornung, T. Wolf, A. Erb, M. Kläser, and G. Müller-Vogt, *Giant pressure effect in oxygen deficient $YBa_2Cu_3O_x$*, Physica C: Superconductivity **270**, 258 (1996).

[86] S. Sadewasser, J. S. Schilling, A. P. Paulikas, and B. W. Veal, *Pressure dependence of Tc to 17 GPa with and without relaxation effects in superconducting $YBa_2Cu_3O_x$*, Phys. Rev. B **61**, 741 (2000).

[87] L. Tassini, Ph.d. thesis, Technische Universität München, 2008.

[88] R. Roßner, *Untersuchung von korrelierten Elektronensystemen unter hohem Druck*, Diplomarbeit, Technische Universität München (2010).

[89] M. Lavagnini, Ph.D. thesis, ETH Zürich, 2009.

[90] M. I. Eremets, *High Pressure Experimental Methods* (Oxford University Press, 1996).

[91] J. J. H. Hamlin, Ph.D. thesis, Washington University, St. Louis, 2007.

[92] G. Haunschild, *Study of superconductors in a diamond anvil cell*, Bachelor Thesis, Technische Universität München (2012).

[93] A. Driessen, E. van der Poll, and I. F. Silvera, *Equation of state of solid ^{4}He*, Phys. Rev. B **33**, 3269 (1986).

[94] G. J. Piermarini and S. Block, *Ultrahigh pressure diamond-anvil cell and several semiconductor phase transition pressures in relation to the fixed point pressure scale*, Rev. Sci. Instrum. **46**, 973 (1975).

[95] R. A. Forman, G. J. Piermarini, J. D. Bernett, and S. Block, *Pressure Measurement Made by the Utilization of Ruby Sharp-Line Luminescence*, Science **176**, 284 (1972).

[96] J. H. Eggert, F. Moshary, W. J. Evans, K. A. Goettel, and I. F. Silvera, *Ruby at high pressure. III. A pumping scheme for the R lines up to 230 GPa*, Phys. Rev. B **44**, 7202 (1991).

[97] D. M. Adams, R. Appleby, and S. K. Sharma, *Spectroscopy at very high pressures. Part X. Use of ruby R-lines in the estimation of pressure at ambient and at low temperatures*, J. Phys. E: Sci. Instr. **9**, 1140 (1976).

[98] W. A. Bassett, T. Takahashi, H.-K. Mao, and J. S. Weaver, *Pressure-Induced Phase Transformation in NaCl*, Journal of Applied Physics **39**, 319 (1968).

[99] H.-K. Mao and P. M. Bell, *High-Pressure Physics: Sustained Static Generation of 1.36 to 1.72 Megabars*, Science **200**, 1145 (1978).

[100] H.-K. Mao, J. Xu, and P. M. Bell, *Calibration of the ruby pressure gauge to 800 kbar under quasi-hydrostatic conditions*, J. Geophys. Res. **91**, 4673 (1986).

[101] F. Datchi, A. Dewaele, P. Loubeyre, R. Letoullec, Y. L. Godec, and B. Canny, *Optical pressure sensors for high-pressure-high-temperature studies in a diamond anvil cell*, High Pressure Research **27:4**, 447 (2007).

[102] S.-J. You, L.-C. Chen, and C.-Q. Jin, *Hydrostaticity of Pressure Media in Diamond Anvil Cells*, Chinese Physics Letters **26**, 96202 (2009).

[103] K. Asaumi and A. L. Ruoff, *Nature of the state of stress produced by xenon and some alkali iodides when used as pressure media*, Phys. Rev. B **33**, 5633 (1986).

[104] G. J. Piermarini, S. Block, and J. D. Barnett, *Hydrostatic limits in liquids and solids to 100 kbar*, Journal of Applied Physics **44**, 5377 (1973).

[105] J. H. Burnett, H. M. Cheong, and W. Paul, *The inert gases Ar, Xe, and He as cryogenic pressure media*, Review of Scientific Instruments **61**, 3904 (1990).

[106] R. E. Peierls, *Quantum Theory of Solids* (Oxford University Press, New York, 1955).

[107] E. J. Woll and W. Kohn, *Images of the Fermi Surface in Phonon Spectra of Metals*, Phys. Rev. **126**, 1693 (1962).

[108] T. C. Ozawa and S. J. Kang, *Balls & Sticks: easy-to-use structure visualization and animation program*, Journal of Applied Crystallography **37**, 679 (2004).

[109] B. K. Norling and H. Steinfink, *The Crystal Structure of Neodymium Tritelluride*, Inorganic Chemistry **5**, 1488 (1966).

[110] N. Ru, C. L. Condron, G. Y. Margulis, K. Y. Shin, J. Laverock, S. B. Dugdale, M. F. Toney, and I. R. Fisher, *Effect of chemical pressure on the charge density wave transition in rare-earth tritellurides RTe_3*, Phys. Rev. B **77**, 035114 (2008).

[111] N. Ru, Ph.D. thesis, Stanford University, 2008.

[112] K. Y. Shin, V. Brouet, N. Ru, Z. X. Shen, and I. R. Fisher, *Electronic structure and charge-density wave formation in $LaTe_{1.95}$ and $CeTe_{2.00}$*, Phys. Rev. B **72**, 085132 (2005).

[113] N. Ru and I. R. Fisher, *Thermodynamic and transport properties of YTe_3, $LaTe_3$, and $CeTe_3$*, Phys. Rev. B **73**, 033101 (2006).

[114] V. Brouet, W. L. Yang, X. J. Zhou, Z. Hussain, R. G. Moore, R. He, D. H. Lu, Z. X. Shen, J. Laverock, S. B. Dugdale, N. Ru, and I. R. Fisher, *Angle-resolved photoemission study of the evolution of band structure and charge density wave properties in* $R\mathrm{Te}_3$ *(R = Y, La, Ce, Sm, Gd, Tb, and Dy)*, Phys. Rev. B **77**, 235104 (2008).

[115] G.-H. Gweon, J. D. Denlinger, J. A. Clack, J. W. Allen, C. G. Olson, E. DiMasi, M. C. Aronson, B. Foran, and S. Lee, *Direct Observation of Complete Fermi Surface, Imperfect Nesting, and Gap Anisotropy in the High-Temperature Incommensurate Charge-Density-Wave Compound $SmTe_3$*, Phys. Rev. Lett. **81**, 886 (1998).

[116] V. Brouet, W. L. Yang, X. J. Zhou, Z. Hussain, N. Ru, K. Y. Shin, I. R. Fisher, and Z. X. Shen, *Fermi Surface Reconstruction in the CDW State of $CeTe_3$ Observed by Photoemission*, Phys. Rev. Lett. **93**, 126405 (2004).

[117] F. Schmitt, P. S. Kirchmann, U. Bovensiepen, R. G. Moore, L. Rettig, M. Krenz, J.-H. Chu, N. Ru, L. Perfetti, D. H. Lu, M. Wolf, I. R. Fisher, and Z.-X. Shen, *Transient Electronic Structure and Melting of a Charge Density Wave in $TbTe_3$*, Science **321**, 1649 (2008).

[118] E. DiMasi, M. C. Aronson, J. F. Mansfield, B. Foran, and S. Lee, *Chemical pressure and charge-density waves in rare-earth tritellurides*, Phys. Rev. B **52**, 14516 (1995).

[119] R. G. Moore, V. Brouet, R. He, D. H. Lu, N. Ru, J.-H. Chu, I. R. Fisher, and Z.-X. Shen, *Fermi surface evolution across multiple charge density wave transitions in $ErTe_3$*, Phys. Rev. B **81**, 073102 (2010).

[120] R. Gross and A. Marx, *Lecture notes to Applied Superconductivity: Josephson Effect and Superconducting Electronics* (Walther-Meißner-Institut, Bayerische Akademie der Wissenschaften, 2005), chap. F.

[121] J. Jensen and A. R. Mackintosh, in *Rare Earth Magnetism*, edited by J. Birman, S. F. Edwards, C. H. Llewellyn Smith, and M. Rees (Clarendon press, Oxford, 1991).

[122] J. J. Hamlin, D. A. Zocco, T. A. Sayles, M. B. Maple, J.-H. Chu, and I. R. Fisher, *Pressure-Induced Superconducting Phase in the Charge-Density-Wave Compound Terbium Tritelluride*, Phys. Rev. Lett. **102**, 177002 (2009).

[123] M. B. Maple, J. J. Hamlin, D. A. Zocco, M. Janoschek, R. E. Baumbach, B. D. White, I. R. Fisher, and J.-H. Chu, *Superconductivity, spin and charge order, and quantum criticality in correlated electron materials*, EPJ Web of Conferences **23**, 00012 (2012).

[124] K. N. R. Taylor and M. I. Darby, *Physics of Rare Earth Solids* (Chapman and Hall Ltd., London, 1972).

[125] S. Blundell, *Magnetism in Condensed Matter* (Oxford University Press, 2001).

[126] N. Ru, J.-H. Chu, and I. R. Fisher, *Magnetic properties of the charge density wave compounds RTe_3 (R = Y, La, Ce, Pr, Nd, Sm, Gd, Tb, Dy, Ho, Er, and Tm)*, Phys. Rev. B **78**, 012410 (2008).

[127] A. Fang, N. Ru, I. R. Fisher, and A. Kapitulnik, *STM Studies of $TbTe_3$: Evidence for a Fully Incommensurate Charge Density Wave*, Phys. Rev. Lett. **99**, 046401 (2007).

[128] Y. Iyeiri, T. Okumura, C. Michioka, and K. Suzuki, *Magnetic properties of rare-earth metal tritellurides RTe_3 (R = Ce, Pr, Nd, Gd, Dy)*, Phys. Rev. B **67**, 144417 (2003).

[129] A. Sacchetti, C. L. Condron, S. N. Gvasaliya, F. Pfuner, M. Lavagnini, M. Baldini, M. F. Toney, M. Merlini, M. Hanfland, J. Mesot, J.-H. Chu, I. R. Fisher, P. Postorino, and L. Degiorgi, *Pressure-induced quenching of the charge-density-wave state in rare-earth tritellurides observed by x-ray diffraction*, Phys. Rev. B **79**, 201101 (2009).

[130] M. Lavagnini, M. Baldini, A. Sacchetti, D. Di Castro, B. Delley, R. Monnier, J.-H. Chu, N. Ru, I. R. Fisher, P. Postorino, and L. Degiorgi, *Evidence for coupling between charge density waves and phonons in two-dimensional rare-earth tritellurides*, Phys. Rev. B **78**, 201101 (2008).

[131] H. Kuzmany, *Solid-State Spectroscopy - An Introduction* (Springer-Verlag Berlin Heidelberg, 1998).

[132] M. Lavagnini, H.-M. Eiter, L. Tassini, B. Muschler, R. Hackl, R. Monnier, J.-H. Chu, I. R. Fisher, and L. Degiorgi, *Raman scattering evidence for a cascade evolution of the charge-density-wave collective amplitude mode*, Phys. Rev. B **81**, 081101 (2010).

[133] H.-M. Eiter, R. Roßner, M. Lavagnini, R. Hackl, J.-H. Chu, I. R. Fisher, and L. Degiorgi, *Raman study on excitations in charge density wave systems at external pressure*, to be published (2014).

[134] H.-M. Eiter, R. Roßner, M. Lavagnini, R. Hackl, L. Degiorgi, J.-H. Chu, J. G. Analytis, and I. R. Fisher, *High pressure study of charge density wave phase transitions in $ErTe_3$*, Walther Meissner Institute, Annual Report 2011 74 (2011).

[135] M. Lavagnini, F. Pfuner, R. Monnier, L. Degiorgi, H.-M. Eiter, L. Tassini, B. Muschler, R. Hackl, J.-H. Chu, N. Ru, K. Y. Shin, and I. R. Fisher, *Infrared and*

Raman investigation of the charge-density-wave state in rare-earth tri-telluride compounds, Physica B: Condensed Matter **407**, 1864 (2012), proceedings of the International Workshop on Electronic Crystals (ECRYS-2011).

[136] G. Placzek, in *Handbuch der Radiologie*, edited by E. Marx (Akad. Verlagsgesellschaft, Leipzig, 1934), Vol. 6, p. 205.

[137] E. Bauer and M. Rotter, in *Properties and Applications of Complex Intermetallics*, edited by E. Belin-Ferré (World Scientific Publishing Co., 2009), Vol. 2.

[138] O. S. Mortensen and J. A. Koningstein, *Electronic Raman Effect. II. Asymmetry of the Scattering Tensor for Electronic Raman Transitions*, The Journal of Chemical Physics **48**, 3971 (1968).

[139] W. C. Martin, R. Zalubas, and L. Hagan, *Atomic Energy Levels – The Rare-Earth Elements*, Nat. Stand. Ref. Data Ser., Nat. Bur. Stand. (U.S.) **60**, 294 (1978).

[140] H. Kramers, *General Theory of Paramagnetic Rotation in Crystals*, Proc. Acad. Sci. Amsterdam **33**, 959 (1930).

[141] R. Gross and A. Marx, *Festkörperphysik* (Oldenbourg Verlag, München, 2012).

[142] J. T. Hougen and S. Singh, *Electronic Raman Effect in Pr^{3+} Ions in Single Crystals of $PrCl_3$*, Phys. Rev. Lett. **10**, 406 (1963).

[143] S. Jandl, P. Dufour, T. Strach, T. Ruf, M. Cardona, V. Nekvasil, C. Chen, and B. M. Wanklyn, *Raman study of intermultiplet crystal-field excitations in Nd_2CuO_4*, Phys. Rev. B **52**, 15558 (1995).

[144] S. Jandl, M. Iliev, C. Thomsen, T. Ruf, M. Cardona, B. M. Wanklyn, and C. Chen, *Crystal field Raman scattering in Nd_2CuO_4*, Solid State Communications **87**, 609 (1993).

[145] M. Schwoerer and H. C. Wolf, *Organische Molekulare Festkörper* (Wiley-VCH Verlag, Weinheim, 2005).

[146] W. S. Lee, A. P. Sorini, M. Yi, Y. D. Chuang, B. Moritz, W. L. Yang, J.-H. Chu, H. H. Kuo, A. G. C. Gonzalez, I. R. Fisher, Z. Hussain, T. P. Devereaux, and Z. X. Shen, *Resonant enhancement of charge density wave diffraction in the rare-earth tritellurides*, Phys. Rev. B **85**, 155142 (2012).

[147] G. Bilbro and W. L. McMillan, *Theoretical model of superconductivity and the martensitic transformation in A15 compounds*, Phys. Rev. B **14**, 1887 (1976).

[148] T. P. Devereaux, *Theory for the effects of impurities on the Raman spectra of superconductors*, Phys. Rev. B **45**, 12965 (1992).

[149] D. Einzel, priv. comm. (2014) (unpublished).

[150] R. Y. Chen, B. F. Hu, T. Dong, and N. L. Wang, *Revealing multiple charge-density-wave orders in $TbTe_3$ by optical conductivity and ultrafast pump-probe experiments*, Phys. Rev. B **89**, 075114 (2014).

[151] F. Pfuner, P. Lerch, J.-H. Chu, H.-H. Kuo, I. R. Fisher, and L. Degiorgi, *Temperature dependence of the excitation spectrum in the charge-density-wave $ErTe_3$ and $HoTe_3$ systems*, Phys. Rev. B **81**, 195110 (2010).

[152] B. F. Hu, B. Cheng, R. H. Yuan, T. Dong, A. F. Fang, W. T. Guo, Z. G. Chen, P. Zheng, Y. G. Shi, and N. L. Wang, *Optical study of the multiple charge-density-wave transitions in $ErTe_3$*, Phys. Rev. B **84**, 155132 (2011).

[153] V. N. Kostur, *Electron Raman-scattering in metals with strong electron-phonon coupling*, Z. Phys. B **89**, 149 (1992).

[154] S.-H. Lee, J. M. Tranquada, K. Yamada, D. J. Buttrey, Q. Li, and S.-W. Cheong, *Freezing of a Stripe Liquid*, Phys. Rev. Lett. **88**, 126401 (2002).

[155] L. Benfatto, S. Caprara, and C. Di Castro, *Gap and pseudogap evolution within the charge-ordering scenario for superconducting cuprates*, Eur. Phys. J. B **17**, 95 (2000).

[156] R. M. Fernandes, A. V. Chubukov, and J. Schmalian, *What drives nematic order in iron-based superconductors?*, Nat. Phys. **10**, 97 (2014).

[157] A. Sacchetti, L. Degiorgi, T. Giamarchi, N. Ru, and I. R. Fisher, *Chemical pressure and hidden one-dimensional behavior in rare-earth tri-telluride charge-density wave compounds*, Phys. Rev. B **74**, 125115 (2006).

[158] A. Virosztek and A. Ványolos, *Electronic Raman scattering in unconventional density waves*, Phys. Rev. B **72**, 115119 (2005).

[159] D. Einzel and L. Klam, *Response, Relaxation and Transport in Unconventional Superconductors*, J. Low Temp. Phys. **150**, 57 (2008).

[160] P. B. Miller and J. D. Axe, *Internal Strain and Raman-Active Vibrations in Solids*, Phys. Rev. **163**, 924 (1967).

[161] B. Keck and A. Schmid, *Superconductivity and electron-phonon interaction in impure simple metals*, J. Low Temp. Phys. **24**, 611 (1976).

[162] C. M. Varma and W. Weber, *Phonon Dispersion in Transition Metals*, Phys. Rev. Lett. **39**, 1094 (1977).

[163] A. Bauer and C. Pfleiderer, *Magnetic phase diagram of MnSi inferred from magnetization and ac susceptibility*, Phys. Rev. B **85**, 214418 (2012).

[164] B. Lebech, in *Recent Advances in Magnetism of Transition Metal Compounds*, edited by A. Kotani and N. Suzuki (World Scientific, Singapore, 1993), pp. 167–178.

[165] K. Everschor, Ph.D. thesis, Universität zu Köln, 2012.

[166] Y. Ishikawa, G. Shirane, J. A. Tarvin, and M. Kohgi, *Magnetic excitations in the weak itinerant ferromagnet MnSi*, Phys. Rev. B **16**, 4956 (1977).

[167] B. Roessli, P. Böni, W. E. Fischer, and Y. Endoh, *Magnetic field dependence of chiral fluctuations in MnSi*, Physica B: Condensed Matter **345**, 124 (2004), proceedings of the Conference on Polarised Neutron and Synchrotron X-rays for Magnetism.

[168] A. E. Petrova and S. M. Stishov, *Ultrasonic studies of the magnetic phase transition in MnSi*, J. Phys.: Condens. Matter **21**, 196001 (2009).

[169] S. M. Stishov, A. E. Petrova, S. Khasanov, G. K. Panova, A. A. Shikov, J. C. Lashley, D. Wu, and T. A. Lograsso, *Heat capacity and thermal expansion of the itinerant helimagnet MnSi*, J. Phys.: Condens. Matter **20**, 235222 (2008).

[170] Y. Ishikawa, K. Tajima, D. Bloch, and M. Roth, *Helical spin structure in manganese silicide MnSi*, Solid State Communications **19**, 525 (1976).

[171] H. J. Williams, J. H. Wernick, R. C. Sherwood, and G. K. Wertheim, *Magnetic Properties of the Monosilicides of Some 3d Transition Elements*, Journal of Applied Physics **37**, 1256 (1966).

[172] T. H. R. Skyrme, *A Non-Linear Field Theory*, Proceedings of the Royal Society of London. Series A. Mathematical and Physical Sciences **260**, 127 (1961).

[173] B. Borén, *Röntgenuntersuchung der Legierungen von Silicium mit Chrom, Mangan, Kobalt und Nickel*, Ark. Kemi Min. Geol. **11 A**, 1 (1933).

[174] L. Pauling and A. M. Soldate, *The Nature of the Bonds in the Iron Silicide FeSi and Related Crystals*, Acta Crystallographica **1**, 212 (1948).

[175] L. F. Mattheiss and D. R. Hamann, *Band structure and semiconducting properties of FeSi*, Phys. Rev. B **47**, 13114 (1993).

[176] L. Vočadlo, G. D. Price, and I. G. Wood, *Crystal structure, compressibility and possible phase transitions in ϵ-FeSi studied by first-principles pseudopotential calculations*, Acta Crystallographica Section B **55**, 484 (1999).

[177] V. E. Dmitrienko, *Quasicrystals and their approximants: dodecahedral local ordering versus canonical-cell description*, Acta Crystallographica Section A **50**, 515 (1994).

[178] D. Shechtman, I. Blech, D. Gratias, and J. W. Cahn, *Metallic Phase with Long-Range Orientational Order and No Translational Symmetry*, Phys. Rev. Lett. **53**, 1951 (1984).

[179] A. Neubauer, J. Bœuf, A. Bauer, B. Russ, H. v. Löhneysen, and C. Pfleiderer, *Ultra-high vacuum compatible image furnace*, Rev. Sci. Instrum. **82**, 013902 (2011).

[180] J. W. Allen and J. C. Mikkelsen, *Optical properties of CrSb, MnSb, NiSb, and NiAs*, Phys. Rev. B **15**, 2952 (1977).

[181] D. B. Tanner and T. Timusk, in *Physical Properties of High Temperature Superconductors III*, edited by D. M. Ginsberg (World Scientific, Singapore, 1992), p. 363.

[182] C. Pfleiderer, *On the Identification of Fermi-Liquid Behavior in Simple Transition Metal Compounds*, J. Low Temp. Phys. **147**, 231 (2007).

[183] T. Tite, G. J. Shu, F. C. Chou, and Y.-M. Chang, *Structural and thermal properties of MnSi single crystal*, Appl. Phys. Lett. **97**, 031909 (2010).

[184] P. G. Klemens, *Anharmonic Decay of Optical Phonons*, Phys. Rev. **148**, 845 (1966).

[185] S. V. Demishev, V. V. Glushkov, I. I. Lobanova, M. A. Anisimov, V. Y. Ivanov, T. V. Ishchenko, M. S. Karasev, N. A. Samarin, N. E. Sluchanko, V. M. Zimin, and A. V. Semeno, *Magnetic phase diagram of MnSi in the high-field region*, Phys. Rev. B **85**, 045131 (2012).

[186] J. Menéndez and M. Cardona, *Temperature dependence of the first-order Raman scattering by phonons in Si, Ge, and α-Sn: Anharmonic effects*, Phys. Rev. B **29**, 2051 (1984).

[187] C. Postmus, J. R. Ferraro, and S. S. Mitra, *Pressure Dependence of Infrared Eigenfrequencies of KCl and KBr*, Phys. Rev. **174**, 983 (1968).

[188] W. J. Borer, S. S. Mitra, and K. V. Namjoshi, *Line shape and temperature dependence of the first order Raman spectrum of diamond*, Solid State Commun. **9**, 1377 (1971).

[189] R. A. Cowley, *Raman scattering from crystals of the diamond structure*, J. Phys. France **26**, 659 (1965).

[190] G. P. Zinoveva, L. P. Andreeva, and P. V. Geld, *Elastic constants and dynamics of crystal lattice in monosilicides with B20 structure*, Phys. Status Solidi A **23**, 711 (1974).

[191] J. R. Jasperse, A. Kahan, J. N. Plendl, and S. S. Mitra, *Temperature Dependence of Infrared Dispersion in Ionic Crystals LiF and MgO*, Phys. Rev. **146**, 526 (1966).

[192] N. W. Ashcroft and N. D. Mermin, *Solid State Physics* (Saunders College, Philadelphia, 1976).

[193] T. H. K. Barron, J. G. Collins, and G. K. White, *Thermal expansion of solids at low temperatures*, Adv. Phys. **29**, 609 (1980).

[194] G. K. White, R. B. Roberts, and E. Fawcett, *Thermal expansion of Cr and CrV alloys. I. Experiment*, J. Phys. F **16**, 449 (1986).

[195] M. Matsunaga, Y. Ishikawa, and T. Nakajima, *Magneto-Volome Effect in the Weak Itinerant Ferromagnet MnSi*, J. Phys. Soc. Jpn. **51**, 1153 (1982).

[196] D. J. Lockwood and M. G. Cottam, *The spin-phonon interaction in FeF_2 and MnF_2 studied by Raman spectroscopy*, Journal of Applied Physics **64**, 5876 (1988).

[197] X. K. Chen, J. C. Irwin, and J. P. Franck, *Evidence for a strong spin-phonon interaction in cupric oxide*, Phys. Rev. B **52**, R13130 (1995).

[198] J. Laverdière, S. Jandl, A. A. Mukhin, V. Y. Ivanov, V. G. Ivanov, and M. N. Iliev, *Spin-phonon coupling in orthorhombic $RMnO_3$ (R = Pr, Nd, Sm, Eu, Gd, Tb, Dy, Ho, Y): A Raman study*, Phys. Rev. B **73**, 214301 (2006).

[199] E. Fawcett, *Magnetic Grüneisen parameters of critical fluctuations in spin-density wave metals Cr, MnSi and Mn_3Si* , Physica B: Condens. Matter **161**, 83 (1989).

[200] W. Götze and P. Wölfle, *Homogeneous Dynamical Conductivity of Simple Metals*, Phys. Rev. B **6**, 1226 (1972).

[201] B. Muschler, W. Prestel, R. Hackl, T. P. Devereaux, J. G. Analytis, J.-H. Chu, and I. R. Fisher, *Band- and momentum-dependent electron dynamics in superconducting $Ba(Fe_{1-x}Co_x)_2As_2$ as seen via electronic Raman scattering*, Phys. Rev. B **80**, 180510 (2009).

[202] N. Toyota, M. Lang, and J. Müller, *Low-Dimensional Molecular Metals* (Springer, 2007).

[203] F. Venturini, Q.-M. Zhang, R. Hackl, A. Lucarelli, S. Lupi, M. Ortolani, P. Calvani, N. Kikugawa, and T. Fujita, *Raman scattering versus infrared conductivity: Evidence for one-dimensional conduction in $La_{2-x}Sr_xCuO_4$*, Phys. Rev. B **66**, 060502 (2002).

[204] A. Chattopadhyay and M. Jarrell, *Dynamics of disordered heavy-fermion systems*, Phys. Rev. B **56**, R2920 (1997).

[205] F. Venturini, M. Opel, T. P. Devereaux, J. K. Freericks, I. Tüttő, B. Revaz, E. Walker, H. Berger, L. Forró, and R. Hackl, *Observation of an Unconventional Metal-Insulator Transition in Overdoped CuO_2 Compounds*, Phys. Rev. Lett. **89**, 107003 (2002).

[206] I. I. Mazin, T. P. Devereaux, J. G. Analytis, J.-H. Chu, I. R. Fisher, B. Muschler, and R. Hackl, *Pinpointing gap minima in $Ba(Fe_{0.94}Co_{0.06})_2As_2$ via band-structure calculations and electronic Raman scattering*, Phys. Rev. B **82**, 180502 (2010).

[207] P. B. Allen, *Fermi-surface harmonics: A general method for nonspherical problems. Application to Boltzmann and Eliashberg equations*, Phys. Rev. B **13**, 1416 (1976).

[208] A. E. Ioffe and A. R. Regel, in *Progress in Semiconductors*, edited by A. F. Gibson (Heywood & Co. Ltd., London, 1960), Vol. 4, p. 237.

[209] N. F. Mott, *Conduction in non-crystalline systems IX. the minimum metallic conductivity*, Philosophical Magazine **26**, 1015 (1972).

[210] N. E. Hussey, K. Takenaka, and H. Takagi, *Universality of the Mott-Ioffe-Regel limit in metals*, Philos. Mag. **84**, 2847 (2004).

[211] N. E. Hussey, J. C. Alexander, and R. A. Cooper, *Optical response of high-T_c cuprates: Possible role of scattering rate saturation and in-plane anisotropy*, Phys. Rev. B **74**, 214508 (2006).

[212] A. Neubauer, priv. comm. (2012) (unpublished).

[213] A. Zawadowski and M. Cardona, *Theory of Raman scattering on normal metals with impurities*, Phys. Rev. B **42**, 10732 (1990).

List of publications

1. M. Lavagnini, H.-M. Eiter, L. Tassini, B. Muschler, R. Hackl, R. Monnier, J.-H. Chu, I. R. Fisher, and L. Degiorgi, *Raman scattering evidence for a cascade evolution of the charge-density-wave collective amplitude mode*, Phys. Rev. B **81**, 081101 (2010).

2. M. Lavagnini, F. Pfuner, R. Monnier, L. Degiorgi, H.-M. Eiter, L. Tassini, B. Muschler, R. Hackl, J.-H. Chu, N. Ru, K. Y. Shin, and I. R. Fisher, *Infrared and Raman investigation of the charge-density-wave state in rare-earth tri-telluride compounds*, Physica B: Condensed Matter **407**, 1864–1867 (2012).

3. H.-M. Eiter, M. Lavagnini, R. Hackl, E. A. Nowadnick, A. F. Kemper, T. P. Devereaux, J.-H. Chu, J. G. Analytis, I. R. Fisher, and L. Degiorgi, *Alternative route to charge density wave formation in multiband systems*, Proc. Nat. Acad. Sci. U.S.A. **110**, 64–69 (2013).

4. H.-M. Eiter, P. Jaschke, R. Hackl, A. Bauer, M. Gangl, and C. Pfleiderer, *Raman study of the temperature and magnetic field dependence of electronic and lattice properties in MnSi*, Phys. Rev. B **90**, 024411 (2014).

Parts of the text and data presented in Chapters 2, 3 and 4 are taken from the peer-reviewed scientific journals listed above. I contributed to the publications as follows: (1) I set up and performed the experiments, analyzed the data, wrote parts of the text and commented on all versions of the paper. (2) I set up, performed and analyzed a part of the experiments. (3) I set up and performed the experiments and data analysis, contributed to writing and commented on all versions of the text. (4) I set up and performed the experiments and data analysis, wrote the first draft of the publication and commented on all following versions.

Acknowledgement

This work was only possible with the support of numerous people. In particular I am grateful towards:

- *Prof. Dr. Rudolf Gross* for giving me the opportunity to work at the Walther-Meißner-Istitut, his support during the years and helpful advice in any respect.
- *Dr. Rudi Hackl* for his knowledgeable advice, integrity and insightful discussions about life and physics. I cannot thank you enough for the experience I have gained working in your group.
- *Dr. Michela Lavagnini* and *Prof. Dr. Leonardo Degiorgi* for bringing me into the business of studying rare-earth tritellurides which was an enormous benefit for me.
- *Prof. Dr. Christian Pfleiderer, Andreas Bauer,* and *Marlies Gangl,* for providing and characterizing the MnSi single crystals and sharing their broad knowledge about this material.
- *Prof. Dr. Ian Fisher, Dr. James Analytis,* and *Jun-Haw Chu* for providing me with exceptionally clean rare-earth tritelluride samples.
- *Prof. Dr. Tom Devereaux, Dr. Beth Nowadnick, Dr. Lex Kemper,* and *Dr. Brian Moritz* for the theoretical support, particularly the calculation on the tritellurides that greatly enhanced our understanding of these materials. Your hospitality during my visits in Stanford let me have a pleasant and inspiring time.
- *Dr. Leonardo Tassini* for developing and building our prototype diamond anvil cell and for the profound introduction to high pressure techniques as well as Raman scattering.
- *Prof. Dr. B. S. Chandrasekhar* for interesting discussions, proof reading this thesis and (house) concerts of classical music.

- *Dr. Dietrich Einzel* for his pedagogic explanations on Raman theory and for proof reading this thesis.

- my fellow group members *Bernhard Muschler, Florian Kretzschmar, Nitin Chelwani, Andreas Baum, Thomas Böhm,* and *Bea Botka* for the pleasant and constructive atmosphere in the Raman group and for many fruitful discussions.

- *Reinhard Roßner, Peter Jaschke, Markus Künzel, Valentin Kunkel,* and *Georg Haunschild* who contributed during their Diploma and Bachelor works to the success of this dissertation.

- Diploma and Doctoral students of other groups for making the last years a great time. In particular *Elisabeth Hoffmann, Johannes Büttner, Toni Helm, Mathias Weiler, Fred Hocke, Manuel Schwarz, Peter Eder, Friedrich Wulschner, Alma Dorantes, Stefan Geprägs, Jan Goetz, Max Häberlein,* and *Christoph Zollitsch.*

- the technical staff, in particular *Helmut Thies, Robert Müller, Georg Nitschke,* and *Christian Reichlmeier,* for manufacturing most of the parts needed for the cryogenic and high pressure setup. Some of the pieces were impossible to build, I thought.

- the helium liquefaction group, *Harald Schwaiger, Peter Binkert,* and *Jan Naundorf,* for providing me with liquid helium even if I didn't order enough.

- *Emel Dönertas,* and *Ludwig Ossiander* for taking care of any financial and organizational problem even on short notice.

- *Wolfi, Johannes, Marc, Markus, Tobias, Florian, Max* und *Zolli* für die kreative Abendgestaltung an jedem Windstag.

- the person I possibly forgot mentioning here.

- my parents *Antonia* and *Klaus,* and my brothers *Michael* and *Bernhard* for interest in my work, support, advice and understanding.

- *Johann Gabriel* for coming into my life recently. And last but not least my beloved wife *Manuela* for always covering my back and the great time we spend together.